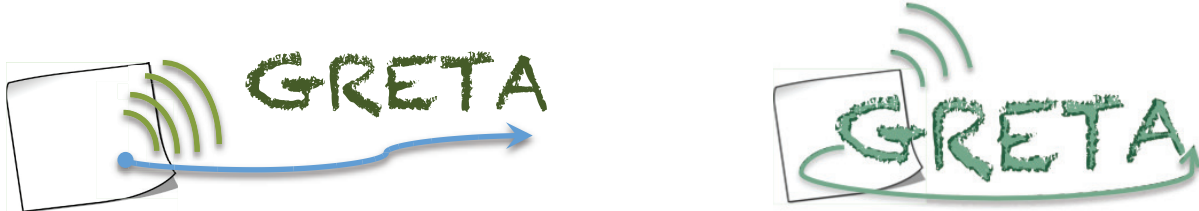


Ministero dell'Istruzione, dell'Università e della Ricerca
PROGRAMMI DI RICERCA SCIENTIFICA DI RILEVANTE INTERESSE NAZIONALE
(PRIN)
Anno 2010-2011 - Progetto GRETA, prot. 2010WHY5PR

ETICHETTE E SENSORI ECO-COMPATIBILI LOCALIZZABILI ED
IDENTIFICABILI CON TECNICHE WIRELESS A BANDA ULTRA LARGA

**GREEN TAGS AND SENSORS WITH UTRAWIDEBAND IDENTIFICATION
AND LOCALIZATION CAPABILITIES (GRETA)**



GRETA
Deliverable Number: D3
Report on the Second Year of Activity

Date of Delivery: March 2015 (T0+24)

Editor(s): Maurizio Bozzi, Pietro Savazzi

Participating institutions: UNIAQ, UNIBO, UNIFE, UNIPG, UNIPV

Contributors: UNIAQ, UNIBO, UNIFE, UNIPG, UNIPV

Workpackage number: (Please fill in)

Nature: R

Dissemination Level: Public

Version: final

Abstract:

The main objective of this deliverable is the final GRETA reader-to-tag architecture and demonstrator definitions. In more details, three different configuration modes, exploiting UWB only and hybrid UHF-UWB tags, are given by detailing all the required system specifications and operating conditions.

The first introductory section describes the second year achievements of GRETA, providing a brief summary of all the topics addressed.

The three different configuration modes are then detailed, by the definition of all the main system parameters and specifications.

The second-year results on UWB localization and tracking algorithms and network management protocols are given as well as the updated link and power budget analysis, taking into accounts the final choice for the three architecture scenarios.

Finally the demonstrator architecture is described with preliminary measurements collected at the initial testbed.

Keyword list: RFID, UWB, green, energy harvesting, localization, CS

CONTENTS

List of acronyms	5
1 Introduction	17
1.1 Notation	17
2 Summary of 2nd Year of Activity	19
3 Design and Implementation of the System Single Parts	21
3.1 Introduction	21
3.2 UWB Interrogation Structure	21
3.3 Configuration Mode 1: UWB Stand-Alone	23
3.4 Configuration Mode 2: Gen2 - UWB	24
3.4.1 Design of the RF components of the architecture	27
3.5 Configuration Mode 3: Gen2 - UWB Enhanced	27
3.6 UWB Parameters Choice	29
3.7 UHF Parameters Choice	29
3.8 UWB Link Budget	30
3.9 Energy harvesting component	30
3.10 UWB backscatter modulator	34
3.10.1 Analysis of the modulation performance	35
3.10.2 Lumped-elements based modulator	36
3.10.3 IC modulator	41
3.11 Green Technologies	43
3.12 Antenna system	53
3.13 Localization and tracking algorithm	61
3.13.1 Range Information Model	62
3.13.2 Tractable Range Information Model	64
3.13.3 Design of the Energy Detector	65
3.13.4 Results	66
3.14 Network Management Protocols	71
3.14.1 UWB-enhanced Identification	71
3.14.2 Performance Results	72
3.14.3 Multi-Reader Systems	73
3.15 Efficient RFID Tag Identification exploiting UWB and Compressive Sensing	78
3.15.1 System Model	79
3.15.2 Tag population estimation and groups identification	80
3.15.3 Proposed UWB-CS Algorithm	81
3.15.4 First step: Estimating the number of active tags and groups	81
3.15.5 Second step: Reducing the scale of Compressive Sensing	81
3.15.6 Third step: Tags Identification through CS Decoding Scheme	82
3.15.7 Number of CS Measurements	82
3.15.8 Simulation Environment	83
3.15.9 Performance Evaluation	83
4 Final Demonstrator Definition	86
4.1 Preliminary GRETA Test-Bed	86
4.1.1 Transmitter and Receiver Chain	88
4.1.2 UWB Tag Realization and Spreading Codes	89
4.2 Preliminary Measurements	91

5 Dissemination Activity	95
5.1 University of Bologna	95
5.2 University of L'Aquila	96
5.3 University of Pavia	97
5.4 University of Ferrara	99
5.5 University of Perugia	100
References	101

LIST OF ACRONYMS

ACK	acknowledge
ADC	analog-to-digital converter
AFL	anchor-free localization
AGNSS	assisted-GNSS
AGPS	assisted GPS
AltBOC	alternate binary offset carrier
AOA	angle-of-arrival
AOD	angle of departure
AP	access point
API	application programming interface
ARNS	aeronautical radio navigation services
A-S	anti-spoofing
AS	azimuth spread
ASIC	application specific integrated circuit
AWGN	additive white Gaussian noise
AWG	arbitrary waveform generator
BCH	Bose-Chaudhuri-Hocquenghem
BEP	bit error probability
BLAS	basic linear algebra subprograms
BOC	binary offset carrier
bps	bits per second
BPSK	binary phase shift keying
BPZF	band-pass zonal filter
BS	base station
BSC	binary symmetric channel
C/A	coarse/acquisition
C/NAV	commercial/navigation
CAD	Computer Aided Design
CAP	contention access period
CAWGN	complex additive white Gaussian noise

CBOC	composite binary offset carrier
CC	central cluster
cdf	cumulative distribution function
CDF	cumulative density function
CDMA	code division multiple access
CF	characteristic function
CFP	contention free period
CH	cluster head
CIR	channel impulse response
CKF	cubature Kalman filter
CL	civil-long
CM	civil-moderate
CMOS	Complementary Metal Oxide Semiconductor
Coop-POCS	cooperative projection onto convex sets (POCS)
Coop-OA	cooperative outer-approximation (OA)
COTS	commercial off-the-shelf
CNLS	constrained non-linear least squares (NLS)
CNSS	Compass navigation satellite system
CPR	channel pulse response
cps	chips per second
CRB	Cramér-Rao bound
CRLB	Cramér-Rao lower bound
CRC	cyclic redundancy check
CRPF	cost reference particle filter
CS	control segment/commercial service/compressed sensing
CSI	channel state information
CSS	chirp spread spectrum
CTS	clear-to-send
CW	continuos wave
DAA	Detect and Avoid
DC	Direct Current

DGPS	differential GPS
DIFS	DCF inter-frame spacing
DM	data mining
DMLL	distributed maximum log-likelihood
DLL	delay-locked loop
DoA	Direction of Arrival
DoD	Department of Defense
DP	direct path
DPE	direct position estimation
DS	delay spread
DSSS	direct sequence spread spectrum
dwMDS	distributed weighted multidimensional scaling
EB	energy-based
EBG	Electromagnetic Band Gap
ECEF	Earth-centered, Earth-fixed
ED	energy detector
EGNOS	European geostationary navigation overlay system
EIRP	effective isotropic radiated power
EKF	extended Kalman filter
EKFBT	extended Kalman filter with bias tracking
e.m.	electro-magnetic
EPE	Ekahau positioning engine
ERP	Effective Radiated Power
ERQ	enhanced robust quad
ESA	European Space Agency
EU	European Union
F/NAV	freely accessible navigation
FCC	federal communications commission
FDMA	frequency division multiple access
FEC	forward error correction
FFD	full function device

FIM	Fisher information matrix
FLL	Frequency-locked loop
FOC	full operational capability
FOM	figure of merit
FPGA	field programmable gate array
FPK	Flächen-Korrektur-Parameter (area correction parameters)
GAGAN	GPS aided GEO augmented navigation
GANSS	Galileo/Additional navigation satellite systems
GDOP	geometric dilution of precision
GEO	geostationary
GIOVE	Galileo In-Orbit Validation Element
GIS	geographical information system
GLONASS	global orbiting navigation satellite system
GML	generalized maximum likelihood
GNSS	global navigation satellite system
GPRS	general packet radio service
GPS	global positioning system
GS	geodetic system
GSM	Global System for Mobile communications
HB	Harmonic Balance
hdwMDS	hybrid dwMDS
HEO	highly-inclined elliptical orbits
HMM	hidden Markov model
HOW	handover word
HPOCS	hybrid POCS
HW	hardware
i.i.d.	independent,identically distributed
I/NAV	integrity/navigation
IC	integrated circuit
ICD	interface control document
ICT	information and communication technologies

ID	IDentification
IE	informative element
IF	intermediated frequency
IGSO	inclined geosynchronous orbit
ILS	instrument landing system
IMU	inertial measurement unit
INS	inertial navigation system
IRNSS	regional navigation satellite system
IR-UWB	impulse radio UWB
ISM	industrial scientific medical
ISRO	Indian space research organization
IST	information society technologies
IVP	inertial virtual platform
JBSF	jump back and search forward
JSD	Jensen-Shannon divergence
KDD	Knowledge Discovery
KF	Kalman filter
KNN	k-nearest-neighbor
LAAS	local area augmentation system
LAN	local area network
LAPACK	linear algebra package
LBS	location-based services
LCS	location services
LDC	low duty-cycle
LDPC	low density parity check
LDR	low data rate
LEO	Localization Error Outage
LLC	logical link control
LLR	log-likelihood ratio
LLS	linear least squares
LOB	line-of-bearing

LOS	line-of-sight
LR	likelihood ratio
LRT	likelihood ratio test
LS	least-squares
LSE	least squares estimator
MAC	medium access control
MAP	maximum a posteriori
MBOC	multiplexed binary offset carrier
MBS	maximum bin search
MB-UWB	multi-band UWB
MCRB	modified Cramér–Rao bound
MDS	multi-dimensional scaling
MEMS	micro-electro-mechanical systems
MESS	maximum energy sum selection
MEO	medium earth orbit
MF	matched filter
MGF	moment generating function
MHT	multiple hypotheses testing
MIMO	multiple-input multiple-output
MISO	multiple-input single-output
ML	maximum likelihood
MLE	maximum likelihood estimator
MMSE	minimum mean squared error
MQKF	multiple quadrature Kalman filtering
MRC	maximal ratio combining
MS	mobile station
MSAS	multi-functional satellite augmentation system
MSB	most significant bit
MSE	mean squared error
MSK	Minimum-shift Keying
MST	minimum spanning tree

MTSAT	multi-functional transport satellite
MUI	multi-user interference
N/A	not available
NAV	navigation
NAVSTAR	navigation system for timing and ranging
NB	narrowband
NBI	narrowband interference
NDIS	network driver interface specification
NG	network green
NLOS	non-line-of-sight
NLS	non-linear least squares
NN	neural network
NPE	Navizon positioning engine
NQRT	new quad robustness test
NRZ	non-return to zero
NSI5	non-standard I5
NSQ5	non-standard Q5
NTP	network time protocol
OA	outer-approximation
OC	open circuit
OCS	operational control segment
OFDM	orthogonal frequency division multiplexing
OMA	open mobile alliance
OOK	on-off keying
O-QPSK	offset quadrature shift keying
OQRT	original quad robustness test
ORQ	original robust quad
OS	open service
OTDOA	observed TDOA
P2P	peer-to-peer
P2PP	P2P-positioning

PAM	pulse amplitude modulation
PAN	personal area network
PDA	personal digital assistant
pdf	probability density function
PDP	power delay profile
PF	particle filter
PHY	physical layer
PLL	phase-locked loop
pmf	probability mass function
PMU	Power Management Unit
PN	pseudo-noise
POC	payload operation center
POCS	projection onto convex sets
PN	pseudo-noise
PPM	pulse position modulation
PPS	precise position service
PR	Pseudo-random
PRN	pseudo-random noise
PRP	pulse repetition period
PRS	public regulated service
PRT	partial robustness test
PSD	power spectral density
PSDP	power spatial delay profile
PSK	phase shift keying
pTOA	pseudo time of arrival
PV	position-velocity
PVT	position, velocity, and time
QKF	quadrature Kalman filter
QZSS	quasi-zenith satellite system
RDSS	radio determination satellite service
RF	radio frequency

RFD	reduced function device
RFID	Radio frequency identification
R-GML	reduced complexity generalized maximum likelihood
RIMS	ranging and integrity monitoring stations
RLE	robust location estimation
RMS	root-mean square
RMSE	root mean square error
RMU	remote measurement unit
RNSS	regional navigation satellite system
RQ	robust quadrilateral
RRC	root raised cosine
RRLP	radius resource location protocol
RSMB	root square of mean biased value
RSS	received signal strength
RT	robust trilateration
RTCM	radio technical commission for maritime services
RTLS	real-time locating systems
RTK	real-time kinematic
RTS	ready-to-send
RTT	round-trip time
r.v.	random variable
RV	random variable
SA	selective availability
SAR	search and rescue
SAW	surface acoustic wave
SBAS	satellite-based augmentation system
SBS	serial backward search
SBSMC	serial backward search for multiple clusters
SC	short circuit
SCKF	square-root cubature Kalman filter
SDR	software defined radio

SDS	symmetric double sided
SET	SUPL enabled terminal
S-GML	soft generalized maximum likelihood
SIR	sequential importance resampling
SLP	SUPL location platform
SIFS	short inter frame spacing
SIMO	single-input multiple-output
SIS	signal-in-space
SISO	single-input single-output
SMD	Surface Mounting Device
SoA	state-of-the-art
SoL	safety-of-life
SMC	sequential Monte Carlo
SNR	signal-to-noise ratio
SNIR	signal-to-noise-plus-interference ratio
SPAWN	sum and product algorithm over a wireless network
SPKF	sigma-point Kalman filter
sps	symbols per second
SPS	standard position service
SQKF	square-root quadrature Kalman filter
SRN	secondary reference nodes
SS	spread spectrum/space segment
ST	simple thresholding
SUPL	secure user-plane location
SV	satellite vehicle
SW	software
TCS	threshold crossing search
TDOA	time difference-of-arrival
TDR	Time-domain reflectometry
TI	trilateration intersection
TFTC	Thin Film Transistor Circuit

TLM	telemetry
TMBOC	time-multiplexed binary offset carrier
TOA	time-of-arrival
TOF	time-of-flight
TOW	time of week
TH	time-hopping
TNR	normalized threshold
TTFF	time-to-first-fix
TW-TOA	two-way-TOA
U.S.	United States
UE	user equipment
UERE	user equivalent range error
UHF	ultra high frequency
UKF	unscented Kalman filter
ULP	user location protocol
UMTS	universal mobile telecommunications system
URE	user range error
US	user segment
UT	user terminal
UTC	coordinated universal time
UTM	universal transverse Mercator
UTRA	UMTS terrestrial radio access
UWB	ultra-wide band
UWB-IR	ultra-wide band impulse radio
VANET	vehicular ad-hoc network
VNA	vector network analyzer
VRS	virtual reference station
WAAS	wide area augmentation system
WADGPS	wide area differential GPS
WARN	wide area reference network
WB	wideband

WE	wireless extensions
WGS84	world geodetic system
WiMAX	worldwide interoperability for microwave access
WLAN	wireless local area network
WLS	weighted least squares
WMAN	wireless metropolitan area network
WPAN	wireless personal area network
WR API	wireless research application programming interface
WSN	wireless sensor network
WT	wireless tools
WWB	Weiss-Weinstein bound
ZZB	Ziv-Zakai lower bound
ZZBT	Ziv-Zakai Bellini-Tartara

1 INTRODUCTION

This deliverable describes the second year's achievements of the GRETA project (GReen TAgS and sensors with ultra-wide-band identification and localization capabilities) firstly devoted to the definition of the complete requirements and specifications of the final tag architecture and demonstrator.

The tag architecture has been defined according to the following three different configuration modes:

- stand-alone UWB tag, which provides both localization and communication by means of UWB signaling, and an additional UHF section is used for just energy harvesting and synchronization;
- Integrated UHF-UWB tag, where a standard off-the-shelf Gen.2 chip is exploited for the communication capability, while the UWB section is used for localization and ranging;
- enhanced UHF-UWB architecture, where the standard Gen.2 communication protocol interacts with the UWB subsystem in order to obtain a performance improvement.

The report is organized as follows.

Section 2 shortly describes the activities carried out during the second year of the GRETA project. The main UWB/UHF parameters and the UWB link budget have been defined accordingly, taking into account the second tag configuration mode (Integrate UHF-UWB) as the main objective for the final tag demonstrator.

Section 3 contains the complete description of the tag architecture choices, by detailing all the UWB/UHF parameter definitions, the energy harvesting subsystem, the UWB backscatter modulator and antennas, highlighting their green technologies and environmental impact. The second-year results on UWB localization and tracking algorithms and network management protocols are given as well as the updated link and power budget analysis, taking into accounts the final choice for the three architecture scenarios.

Section 4 is devoted to the final demonstrator definition, describing the preliminary test-bed and measurements.

Finally, in *Section 5*, the dissemination plan and the updated list of publications of each unit is reported.

1.1 Notation

Hereafter the main mathematical notation rules used throughout the text are listed for the reader convenience. Meanings and formats will be maintained along the text, unless otherwise stated.

x, y, z, \dots	scalar variables, either deterministic or stochastic (depending on the context), either real or complex (depending on the context).
$\mathbf{a}, \mathbf{b}, \mathbf{c}, \dots$	vector variables, column-wise defined, either deterministic or stochastic, either real or complex.
$\mathbf{A}, \mathbf{B}, \mathbf{C}, \dots$	matrix variables, either deterministic or stochastic, either real or complex.
\mathbb{R}^M	Field of the real numbers, M -dimensional.
\mathbb{C}^M	Field of the complex numbers, M -dimensional.
$\mathbf{a} \in \mathbb{R}^M$	M -element real vector.
$\mathbf{b} \in \mathbb{C}^N$	N -element complex vector.
$\mathbf{A} \in \mathbb{R}^{M,N}$	Real matrix, with M rows and N columns.
$\Re\{\cdot\}$	Real part.
$\Im\{\cdot\}$	Imaginary part.
$(\cdot)^T$	Transpose operator.
$(\cdot)^*$	Complex conjugate operator.
$(\cdot)^H$	Hermitian operator (transpose, complex conjugate).
$(\cdot)^\dagger$	Moore-Penrose pseudo-inverse.
$\mathbf{A} \succeq \mathbf{B}$	The matrix $(\mathbf{A} - \mathbf{B})$ is nonnegative definite.
$\mathbf{A} \succ \mathbf{B}$	The matrix $(\mathbf{A} - \mathbf{B})$ is positive definite.
$\mathbb{E}\{\cdot\}$	Expected value (stochastic) operator.
\triangleq	Equal by definition.
$\nabla_{\mathbf{x}}(\mathbf{d}(\mathbf{x}))$	Jacobian matrix (partial derivatives of $\mathbf{d}(\mathbf{x})$ w.r.t. \mathbf{x}).
$g(t)$	Function of a continuous variable. E.g., signal or process as a function of the continuous time.
$g[n]$	Function of a discrete variable. E.g., signal or process in the discrete time domain.
f_c	Carrier or central frequency.
B_W	Bandwidth
f_s	Sampling frequency.
T_c	Chip interval.
T_s	Symbol/Pulse interval.
c	Speed of light.
τ_{mean}	Mean excess delay.
σ_τ	Delay spread (RMS).
$P(\cdot)$	Power or Probability (depending on the context).
$p(\cdot)$	Probability density function.
d	Distance (in meters).
(x, y, z)	Cartesian coordinates of a point.

2 SUMMARY OF 2ND YEAR OF ACTIVITY

The second year of GRETA project has been mainly devoted to the final definition of the system architecture and components, in order to start preparing the final demonstrator test-bed.

A modular tag has been designed, considering the two possibilities of using a stand-alone UWB tag for both localization and communication purposes, and an hybrid UHF-UWB architecture, exploiting a standard Gen.2 RFID tag subsystem, to implement the communications protocol. In this way, the UWB subsystem can be used for accurate localization and ranging algorithms, exploiting the standard off-the-shelf UHF-RFID chip. Furthermore, an enhanced UHF-UWB version has been investigated, where the standard Gen.2 communication protocol is modified to enable a tighter interaction with the UWB part in order to obtain a performance improvement. The possibility to implement the 3rd mode is strictly conditioned on the actual effort available. As described in the following. *Section 3*, the three configuration modes are named:

- UWB-Stand-Alone;
- Gen2-UWB;
- Gen2-UWB Enhanced.

The main objective of the final demonstrator is the Gen2-UWB one.

The UWB interrogator structure has been designed, by considering the differences among the three defined configuration modes, while an important output of this project step has been the final definition of both the UWB-UHF parameters nad link budget analysis.

The energy harvesting component design has had to face the simultaneous operations of UHF energy harvesting and UWB communication, by designing a diplexer which must be able to provide both matching conditions nad filtering for the two operating bands.

The performance of the UWB backscatter modulator has been analyzed by both simulations and experimental measurements, considering pro and cons of different circuit implementations.

The design of the IC backscattering modulator is based on the UMC Low-voltage CMOS 180nm (or UMC L180) technology. The fundamental advantages of the proposed CMOS technology are its low cost, the low gate delay (or logic gate propagation delay) lower than 60ps, and the presence of zero and low voltage threshold devices models. The results obtained depend on the trade-off between the parasitics elements of the integrated circuit (IC) transistor: its channel resistance R, and drain-source capacitance C.

The section on Green Technologies presents the improvement in the manufacturing technique of green, eco-compatible and cost effective SIW microwave passive components. The proposed process for the implementation of SIW circuits on paper consists of two steps: the preliminary preparation of the metalized paper substrate and the manufacturing of the circuit, which requires both milling machining and subsequent metallization of the via holes. Beside the fabrication process, the electromagnetic characterization of the involved materials is presented, as well as design and measurements of several prototypes of SIW microwave devices. The microwave front-end of the proposed tag architecture needs two fundamental blocks: a UWB antenna and a diplexer. The first device is required to collect microwave power in very large frequency band and the diplexer is mandatory to separate the path related to the energy harvesting and the one used by data transmission. Both devices can be implemented on paper substrate, and the two frequency bands adopted are the 868 MHz and the lower part of the UWB channel. This project is designed to guarantee 1.7 GHz of bandwidth for data link, in particular from 3.1 to 4.8 GHz.

The localization and tracking process typically consists of two phases:

- a measurement phase, where readers measure their range to the tag;
- a location inference phase, where tags positions are inferred from prior knowledge and measurements.

The performance of a localization system jointly depends on these two phases. The Deliverable GRETA D2 introduced the location inference phase by describing the Bayesian filtering techniques for localization, tracking, and ordering of tags. In this Deliverable, attention is given to the measurement phase.

Considering the selected UWB-UHF hybrid tag, the reader network management protocols may exploit the UWB tag population estimation, in order to make more energy efficient the ISO/IEC 18000-6C standard. It has been demonstrated that it is possible to get the energy consumption 25% lower with the hybrid tag with respect to the current standard. A similar approach has been applied to an hybrid scenario, where the UHF-RFID standard identification protocol, based on frame slotted Aloha, is replaced by a compressive sampling, or compressed sensing (CS), algorithm. Performance analysis show that the identification time can be efficiently reduced by exploiting the UWB localization information.

For a wide set of applications, characterized by large-scale tags deployments, single reader systems (i.e., one reader-multiple tags) are often unable to cover the entire region of interest, given the limitations of the reader's interrogation range. This motivates the use of multiple readers, geographically distributed and networked in some fashion. Multireader MAC protocols design is challenging given that different kind of collision problems arise. UWB technology can be again conveniently exploited for ranging, localization and tag population estimation and as a support for MAC layer operations.

In order to test the tag UWB backscattering functionalities, a preliminary test-bed has been deployed at the University of Bologna. This test-bed version does not include the UHF Gen.2 compliant reader, but it is able to test the UWB backscattering communication capability. Preliminary measurements were conducted by acquiring the 200ksamples available from the TDS6604 oscilloscope at the University of Bologna laboratories.

3 DESIGN AND IMPLEMENTATION OF THE SYSTEM SINGLE PARTS

3.1 Introduction

The purpose of this section is the identification of the GRETA tag architectures following the application requirements, including the viable technologies that can be adopted. In particular, a general modular tag architecture with 3 different configuration modes has been conceived for the project.

The idea is to design a modular tag, able to operate as follows:

- (i) Stand-alone UWB tag, providing both localization and communication by exploiting the UWB signaling, with an additional UHF section for energy harvesting and synchronization.
- (ii) Integrated UHF-UWB tag, where a standard off-the-shelf Gen.2 chip is exploited. In this case the UHF section provides the communication capability and the UWB section is exploited for localization only.
- (iii) We also consider an enhanced UHF-UWB version where the standard Gen.2 communication protocol is modified to enable a tighter interaction with the UWB part in order to maximize the performance. The possibility to implement the 3rd mode is strictly conditioned on the actual effort available.

The aforementioned 3 configurations modes are named:

1. UWB-Stand-Alone;
2. Gen2-UWB;
3. Gen2-UWB Enhanced;

with the following pros and cons for each specific configuration:

1. Innovative and extremely low-power consuming. Not compatible with the Gen.2 UHF standard.
2. Appealing for the compatibility with the Gen.2 standard. It fulfills all the Greta requirements with a reasonable complexity and implementation effort. It is not optimized for energy efficiency.
3. Appealing for the compatibility with the Gen.2 standard. Optimized for communication and energy efficiency. It requires the design of additional circuits and the implementation of the overall Gen.2 stack (and the additional protocol features).

We report the general tag architecture in Fig. 1; thanks to its flexibility, some of the blocks can be avoided according to the configuration chosen, and the control logic can be reconfigured.

Different configuration modes require also the re-design of some blocks (e.g., the matching circuits).

In the following the three configuration modes will be detailed, starting from the generic structure and timing of the UWB communication packet, which is common to all modes.

3.2 UWB Interrogation Structure

During the UWB interrogation cycle of duration T_{int} , the reader transmits a sequence of UWB pulses modulated by a periodic binary spreading sequence $\{d_n\}$ of period N_c specific to that particular reader (reader's code). Note that the use of the spreading sequence $\{d_n\}$ is not strictly necessary but it makes the architecture more flexible and open to other interrogation protocols. In the basic version of the protocol it can be simply set to 1, i.e., $d_n = 1$. In general, N_{pc} pulses are associated to each code symbol (chip). To accommodate the signals backscattered by tags corresponding to an entire packet of N_r symbols, the UWB interrogation contains $N_t = N_r N_s$ pulses, where $N_s = N_c N_{pc}$ is the number of pulses associated to each symbol. For the configuration modes integrated with UHF Gen.2 (modes 2 and 3) the data communication can be operated in the UHF band, then only $N_r = 1 - 2$ symbols are necessary for detection and ranging purposes. For the configuration mode 1 (stand-alone UWB tag), the number of symbols is function of the amount of data to be transmitted (e.g., 128 bits). Pulses are separated by T_p seconds. Therefore the UWB transmitted signal takes the form

$$s_{\text{reader}}^{\text{UWB}}(t) = \sum_{k=0}^{N_t-1} s(t - kN_c T_c) \quad (1)$$

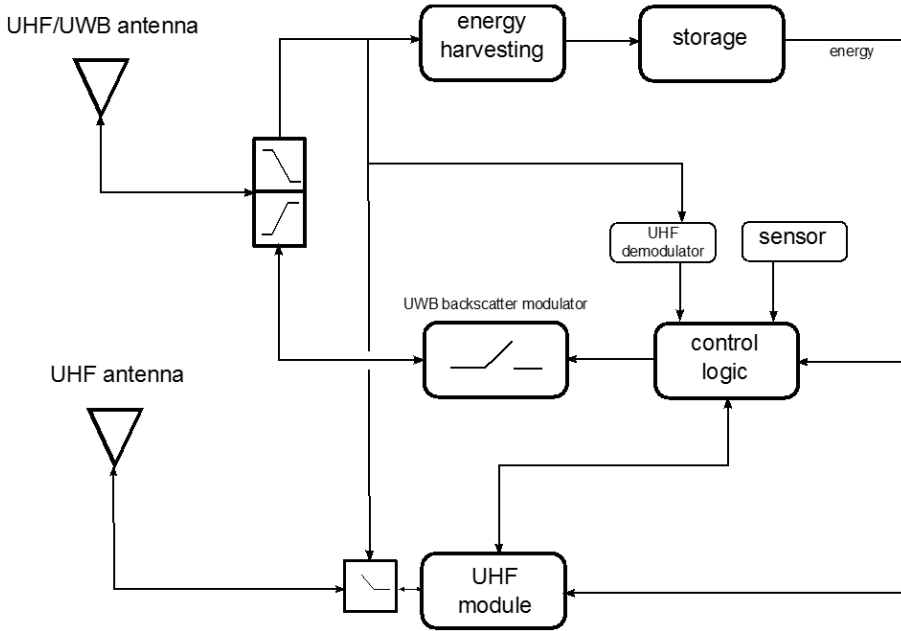


Figure 1: General tag architecture from which each particular configuration mode can be derived.

with the symbol given by

$$s(t) = \sum_{n=0}^{N_c-1} d_n g(t - nT_c) \quad (2)$$

where $T_c = N_{pc} T_p$ is the chip time and $g(t)$ is the composite sequence forming a chip given by

$$g(t) = \sum_{i=0}^{N_{pc}-1} p(t - iT_p) \quad (3)$$

which is composed of N_{pc} elementary UWB pulses $p(t)$. The pulse repetition period T_p is chosen so that all signals backscattered by the environment are received by the reader before the transmission of the successive pulse. The corresponding relations between pulses, chips and symbols are reported in Fig. 2.

Each transmitted pulse is backscattered by the tag's antenna as well as by all the surrounding scatters present in the environment that determine the clutter component.

To make the uplink communication robust to the presence of clutter and interference, a proper backscatter modulation strategy is necessary at tag side. When addressed, depending on the configuration mode, the tag changes continuously its reflection property according to a dedicated spreading code $\{c_n\}$. Specifically, the UWB switch is controlled by a control logic whose purpose is to change the switch status (short or open circuit) at each chip time T_c according to the zero mean (balanced) periodic tag's code $\{c_n\}$, with period N_c , in order to perform clutter removal.

The switch command signal from the micro-controller has the following expression

$$m(t) = \sum_{k=0}^{N_t-1} b_k \sum_{n=0}^{N_c-1} c_n \Pi\left(\frac{1}{T_c}(t - nT_s - iT_p - \Delta)\right) \quad (4)$$

where $\Pi(t)$ is the rectangular function in $[0, 1]$ and Δ is the residual synchronization offset between the chip clock of the tag and that of the reader. One main task of the reader is estimate and compensate this offset. Such an estimation/compensation can be avoided or simplified if proper spreading codes at tag side are exploited.

At the reader side, the received signal is de-spread using the composite code $\{c_n d_n\}$ thus allowing for clutter removal (if $\{c_n\}$ is balanced) and eventual multi-tag interference. The UWB signal round trip time is used to estimate the distance between the tag and the reader (ranging).

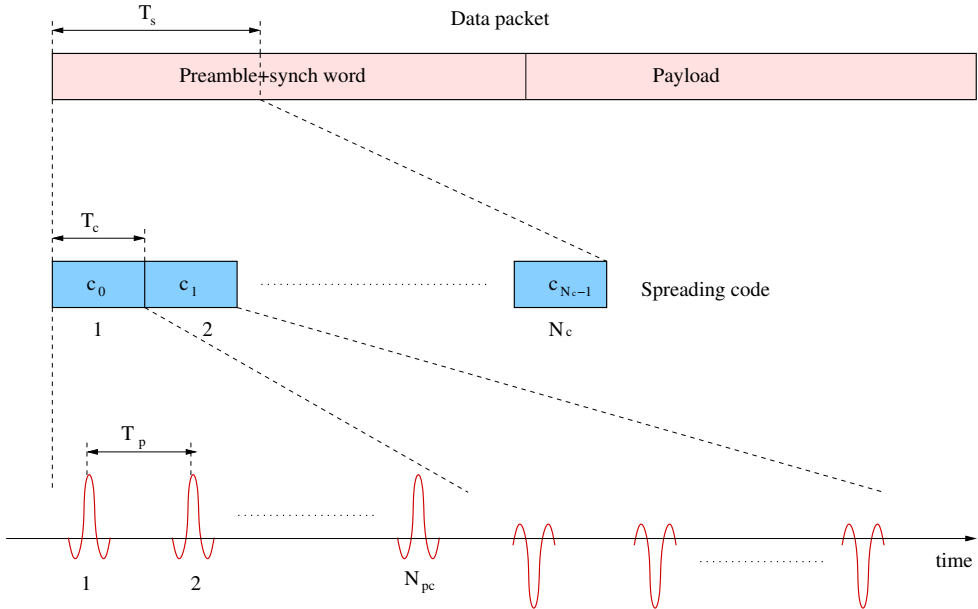


Figure 2: Example of backscattered signal structure, where only the useful component is reported, and $\{d_n\}$ is a sequence of all +1s for simplicity.

3.3 Configuration Mode 1: UWB Stand-Alone

The UWB tag works as a stand-alone entity without the integration of the standard Gen2 protocol. In fact, the standard UHF chip is not present and the architecture reduces as shown in Fig. 3.

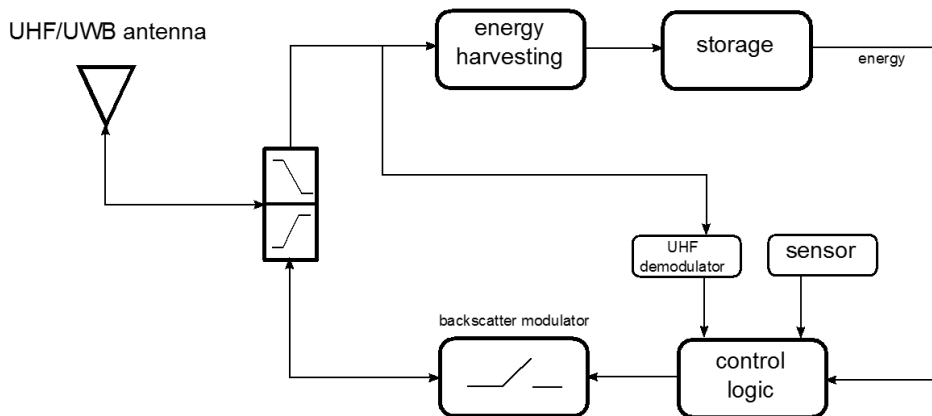


Figure 3: UWB Stand-Alone tag (mode 1).

The UWB communication has to provide to the reader the tag identifier (e.g., the 96 bit of the EPC code), and the sensor data. For this reason the time necessary to transmit the entire packet, according to the parameters values reported in Appendix 1, is long (around 0.2 seconds), and multiple tags have to coexist and communicate with the reader at the same time in order to have a suitable refresh rate. This requires the adoption of proper quasi-orthogonal spreading codes for encoding the communication. Since it is fundamental to provide a good synchronization between reader and all the tags, and to avoid clock drift problems due to the long transmitted packet, a synchronization is ensured by the ASK/OOK modulation of the UHF carrier, working at a frequency which is about 1/10 of the chip rate as trade off between the effect of clock drift and hardware consumption.

The energy is provided by an energy harvesting block working in the UHF band. A proper diplexer

is included to separate the UHF channel, used for harvesting and synchronization, and the UWB channel, used for backscattering communication.

The control logic provides to the backscatter modulator the bits to be transmitted and the proper timing for switching between open and short circuit the RF path. Synchronization is ensured by the UHF link. Specifically, a starting command to reset the spreading code generator and starting the UWB backscatter modulation is realized with the beginning of the ASK/OOK modulation on the continuous wave UHF carrier. If the implementation of the ASK/OOK demodulator is too complex, a simpler circuit detecting the absence of the carrier wave can be adopted. Such a modulation could be also exploited to trigger periodically the local tag clock generator in order to prevent drift during the transmission of the (long) packet.

This solution ensures the minimum energy consumption. In fact the tag design is optimized since no external energy-consuming chips are included.

This architecture can also represent a backup solution in the case the third party chips for standard Gen.2 tag foreseen for mode 2 do not fulfill our requirements of modularity and flexibility.

3.4 Configuration Mode 2: Gen2 - UWB

This mode foresees the UWB tag subsystem as an add-on of a standard Gen.2 UHF passive tag. In this mode there are two possible uses for the tag:

- a) The standard Gen.2 protocol is adopted to identify the tag and to read and write data from/to the tag. The UWB link is used only for high-accuracy ranging (see Fig. 4).

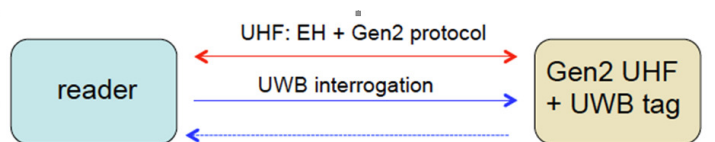


Figure 4: UWB backscatter: only for ranging.

- b) The standard Gen.2 protocol is adopted to identify the tag and the UWB link is used for tag-to-reader data communication and high-accuracy ranging.

Among the possible benefits of such solutions, it is important to underline that channel multiple access is solved by the Gen.2 UHF protocol: since only one tag per time is allowed to communicate with the reader, the multi user interference problem is avoided in the UWB link.

Moreover, since only one tag is active each time, very simple and robust spreading codes can be exploited to drastically simplify synchronization and acquisition at reader side.

In the use case a), the communication is faster as no data are transmitted in the slow UWB communication link, and only 1-2 UWB symbols and one unique spreading code are necessary for ranging (1-2 ms interrogation duration). As a consequence, a simple reader is required to perform tag detection and localization, guaranteeing also high refresh rate (the standard guarantees about 200 reads/s).

However, read/write operations in the Gen.2 tag might be costly in terms of energy consumption, so that for transmission of short sensor measurements, it might be convenient to use the UWB link as in the use case b).

The block schematic of the tag is reported in Fig. 7 below.

At this point, it may be discussed the possibility of including two antennas in the tag. The first one is a hybrid UHF/UWB antenna, which is exploited in the UHF band for energy harvesting only (if necessary, see the discussion later), and in the UWB band for UWB backscattering. The second is a UHF antenna, which is exploited by the Gen.2-compliant tag part for data communication using backscattering. In general, a second UHF antenna to be exploited by the Gen.2 chip is not strictly necessary. However the exploitation of a single hybrid antenna would require a complete re-design of the subsystem and this would lead to an increased solution complexity.

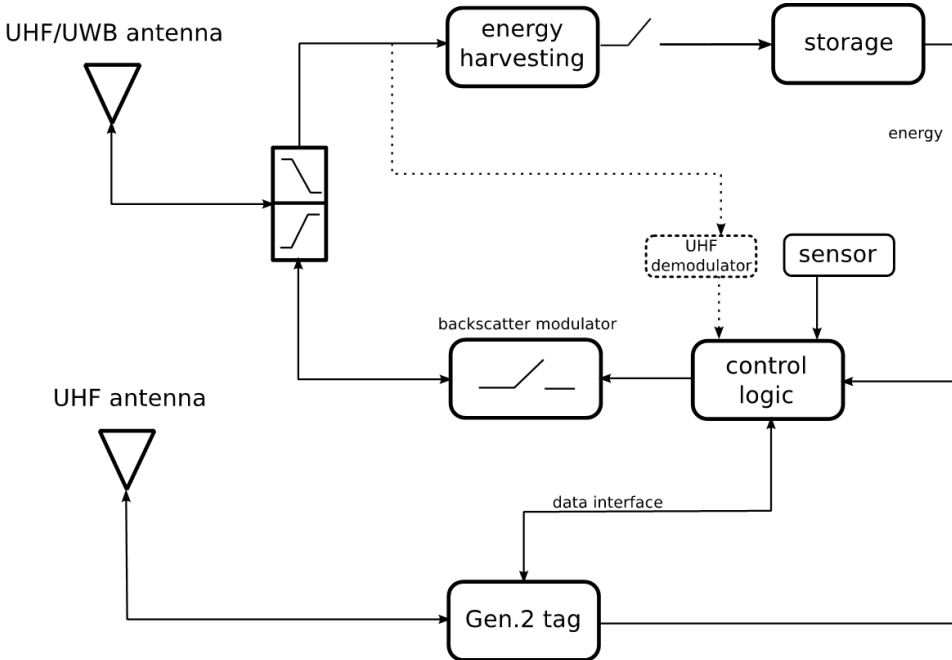


Figure 5: Gen2-UWB tag (mode 2).

The interrogation cycle starts following a standard Gen.2 UHF signaling scheme between the reader and the tag. During this phase, the tag is powered up and all contentions to address only a specific tag are solved.

With the considered architecture, since only one tag per time is active, a unique spreading code $\{c_n\}$ is necessary for ranging, thus drastically simplifying the reader structure. In any case, for better tag modularity and flexibility, the possibility to program different codes and eventually modulate the codes with information bits must be foreseen.

In this case, the synchronization can be conceived in two different manners:

1. Once the UHF tag is addressed, an enable/sync command is sent to the tag control logic via the UHF chip data interface in order to activate the UWB backscatter modulator.
2. Once the UHF tag is addressed, an enable command is sent to the tag via the UHF chip data interface. Then, the UHF carrier exploited for energy harvesting is modulated with ASK/OOK modulation, and this is recognized as starting command for UWB backscattering. In this manner the multiple access is guaranteed since only one tag is addressed by the standard UHF protocol. At the same time a more precise synchronization is ensured by the ASK/OOK modulation.

Once the tag is activated and addressed, the UWB interrogation cycle follows. Upon availability of a different channel for the tag synchronization, the UWB operation can be conducted in parallel or not with the following UHF interrogation. The two resulting interrogation cycles are depicted in the figure below with the corresponding time analysis in the following.

T_{Query} : *Query* → 476.5μs (Delimiter, Preamble, Query Command (22 bits) with 50% “0”, 50% “1”)

$T_{QueryAdjust}$: *QueryAdjust* → 209.375μs (Delimiter, Frame-Sync, QueryAdjust Command (9 bits) with 50% “0”, 50% “1”)

$T_{QueryRep}$: *QueryRep* → 131.25μs (Delimiter, Frame-Sync, QueryRep Command (4 bits), 75% “0”, 25% “1”)

T_{RN16} : *RN16* → 192μs (Preamble, 128μs RN16 Reply @125Kbps, End-of-Signaling)

T_{ACK} : *ACK* → 350μs (Delimiter, Frame-Sync, ACK Command (18 bits) with 50% “0”, 50% “1”)

T_{NAK} : *NAK* → 193.75μs (Delimiter, Frame-Sync, ACK Command (8 bits) with 50% “0”, 50% “1”)

T_{ID} : *EPC_ID* → 1088μs (Preamble, 1024μs PC +EPC + CRC16 @125Kbps, End-of-Signaling)

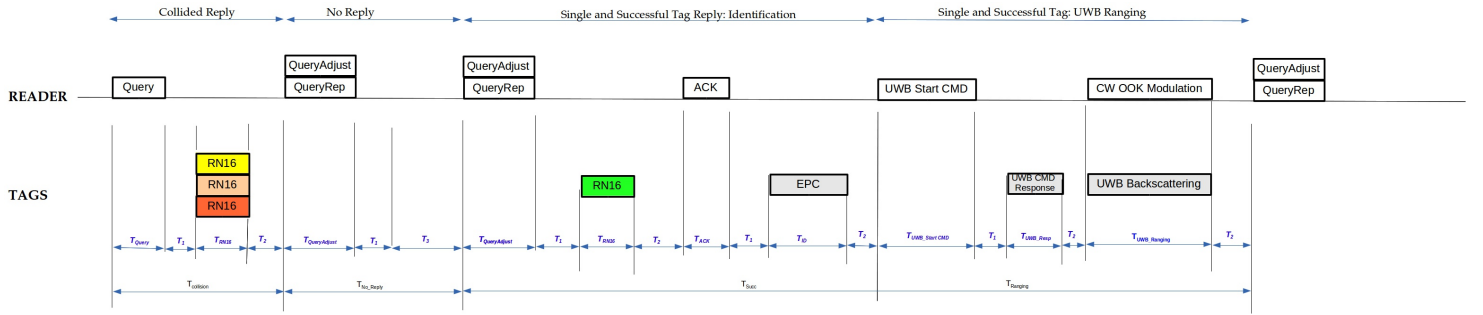


Figure 6: Example of UWB and UHF signal in the Q-algorithm, highlighting the UWB and UHF time analysis.

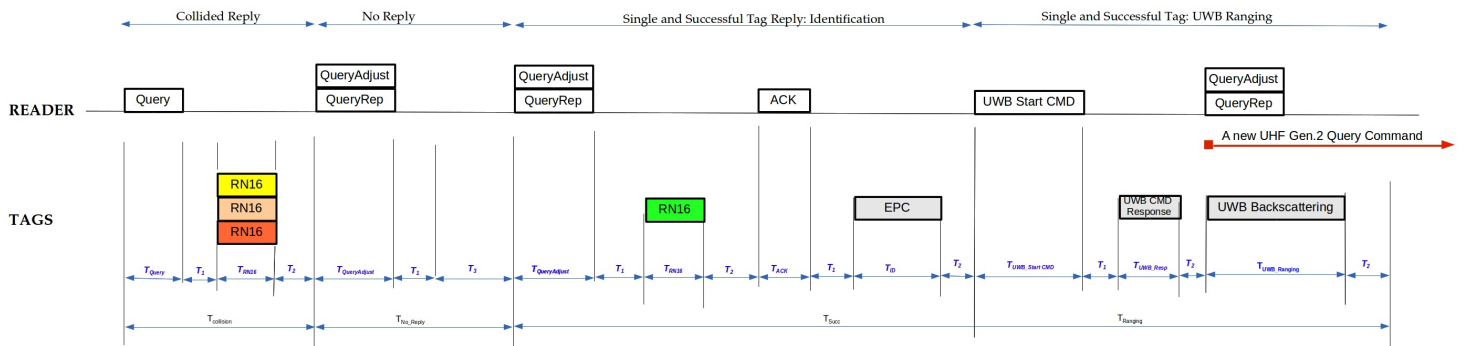


Figure 7: Example of UWB and UHF signal in the Q-algorithm, highlighting the UWB and UHF time analysis with overlap UWB backscattering replay.

$$T_{collision} \rightarrow 812.5\mu s$$

$$T_{idle} \rightarrow 260.625\mu s$$

$$T_{succ} \rightarrow 1804.5\mu s \text{ (with } Query) / 2149.75\mu s \text{ (with } QueryRep)$$

$$T_{UWB_Ranging} \rightarrow 2560\mu s$$

T_{UWB_Start CMD}: → 1031.25μs Delimiter, Preamble, Write Command (66 bits) with 50% “0”, 50% “1” [Write Command like]

T_{UWB_Start CMD_Resp}: → 264μs (Preamble, 128μs RN16 Reply @ 125Kbps, End-of-Signaling) [Write Response like]

$$T_{Ranging} \rightarrow 4015.25\mu s$$

In this solution an external Gen.2 compatible chip is exploited. Such a component represents the highest energy consumption source of the tag. Moreover, the communication range capability of the UHF link (i.e., the tag sensitivity) is strongly related to the availability of an external source of energy to the UHF chip. For this reason the energy harvesting and storage circuit have been included, and must be properly designed. If the UHF chip is able to accumulate enough energy to feed the external circuitry and provide itself the necessary energy to have a reasonable RF sensitivity (which is function of the availability of external energy in commercial UHF chips), the additional energy harvesting circuits could be disconnected.

The UHF carrier adopted for energy harvesting can be the same exploited for the standard Gen.2 communication or an ad-hoc carrier (generated, for example, by the energy showers). In the case the only Gen.2 UHF signal is exploited, it is necessary to properly design the Gen.2 protocol timing before the singulation of the tags in order to ensure the charging of the energy storage (which is fundamental to guarantee the reading of the tags within the reader field of view). This requires being careful with the timing when the tag is externally powered since Gen2. provides specific times for power off and reset of

tag.

Differently, if a second UHF source is used for flooding energy to the tags, a different frequency can be exploited to avoid interference to the standard Gen.2 communication. If such a carrier comes from energy showers, and a synchronization from the UHF band with ASK/OOK modulation is exploited, additional issues have to be considered (tight synchronization between reader and showers). Moreover, if a different frequency is adopted, its behavior on the RF and rectifiers circuits must be characterized when working with the standard Gen.2 UHF signal.

For the test-bed implementation a reasonable solution encompasses the adoption of the commercial UHF tag for tag-to-reader data communication, whose read/write command from/to external units (e.g., sensors) is exploited for synchronizing the UWB backscatter modulator, thus avoiding the UHF demodulator block. Similarly, if such standard UHF chip is able to provide enough energy, the energy harvesting block could be disconnected.

3.4.1 Design of the RF components of the architecture

UHF and UWB signals are completely independent, therefore the load offered by the UWB modulator does not affect the UHF path.

The 3-port filter has to be designed in order to provide both separation of the UHF-UWB signals and matching condition for the energy harvesting section and backscatter modulator. The backscatter modulator shows two possible load conditions, open and short circuit.

The filter should be designed to provide the minimum insertion losses, e.g., 1-2 dB in both the UHF and UWB bands. We would like to realize the energy harvesting and backscatter modulator sections on chip (a single chip or two separate ones).

With regard to the 3-port filter, this can be realized in microstrip technology off-chip (with weakly influence antenna performance); but an on-chip realization would be preferred in this case too.

3.5 Configuration Mode 3: Gen2 - UWB Enhanced

In this case the goal is to maximize the performance of the UHF-UWB tag, by optimizing the standard Gen.2 protocol.

The tag architecture is reported in the figure below.

In this configuration, we exploit ranging/localization capabilities of tags that are ensured by the UWB component to enhance the Gen.2 protocol and make it operate with wireless coverage awareness.

Since the UHF backscatter modulator must be realized on chip, without exploiting a standard Gen.2 compatible chip, a single UHF/UWB antenna of two separated UHF and UWB antennas can be adopted. In any case the UHF antenna has to provide at the same time the possibility of being loaded with the backscatter modulator and the energy harvesting block, as in the standard UHF chips.

Note that a single control logic handles both UWB and UHF channel operations ensuring an optimized behavior from both the communication and the energy efficiency point of view.

The time evolution of the algorithm is illustrated in the figure below and described in the following.

1. Initially, the reader transmits a continuous-wave UHF signal to power up the tags in its maximum transmission range $Range_{Max}$.
 2. As soon as the nodes are powered (i.e., $T_{pw} \approx 1500 \mu s$), the interrogation starts by following the standard Gen.2 protocol.
- Together with the first *Query* command, the reader starts transmitting a sequence of UWB pulses and tags respond by modulating the backscattered UWB signal using the c_n code.
3. The reader interprets the received backscattered signal and estimates $Range_0$ and $Range_1$, namely the interrogation ranges that contains N_0 and $N_0 + N_1$ tags, respectively.
 4. The reader then selects $Q = [\log_2 N_0]$, where $[.]$ denotes the nearest integer function, and sends the following *Query* command with sufficient power to interrogate tags in $Range_0$.

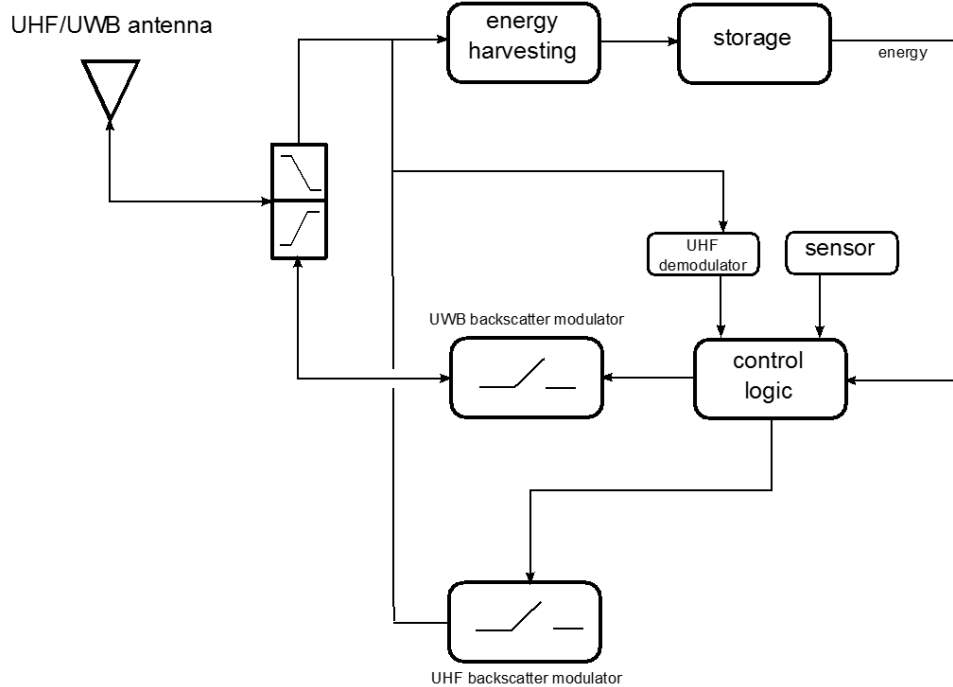


Figure 8: Gen2 - UWB Enhanced (mode 3).

5. Between consecutive *Query* commands, while interrogating tags in *Range0*, the reader continues the UWB ranging procedure by considering *Range1* and *Range2*, which includes further N_2 tags. The UHF transmission power is set to reach also tags that are interrogated in the next *Query*. By doing so, those tags are already powered when receiving the *Query* command.
 6. After N_1 tags have been identified, the reader increases the transmission power of the following *Query* command to reach tags in *Range1* and, similarly, after $N_1 + N_2$ tags have been identified, the transmission power is increased to include *Range2*.
- In this way, the average number of active tags in different stages of the interrogation is kept between $N_0 - N_i$ and N_0 .
- Notice that already identified tags stop responding to query commands as well as backscattering modulated UWB pulses in the same interrogation session.
7. The transmission range is increased every N_i successful interrogations until it reaches *RangeMax* and the session ends when all tags have been identified.

We recall that the proposed mechanism is compliant with the Gen.2 specifications for both the reader and the tag.

The time evolution is reported in the figures below.

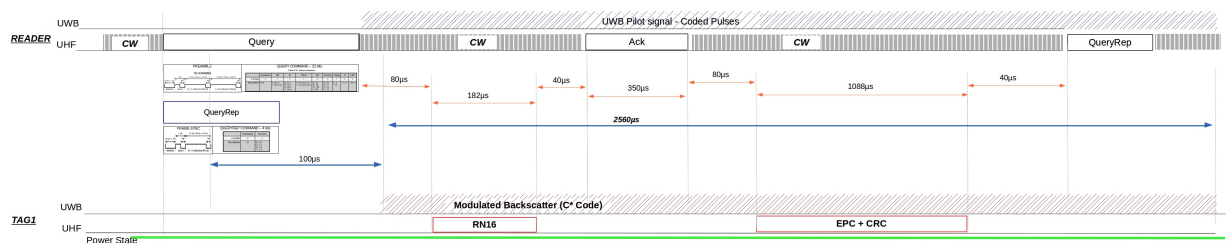


Figure 9: Example of UWB and UHF signal in the adaptive Q-algorithm, highlighting the UWB link tag use.

This solution represents an optimal design and can be considered as the most appealing for a practical

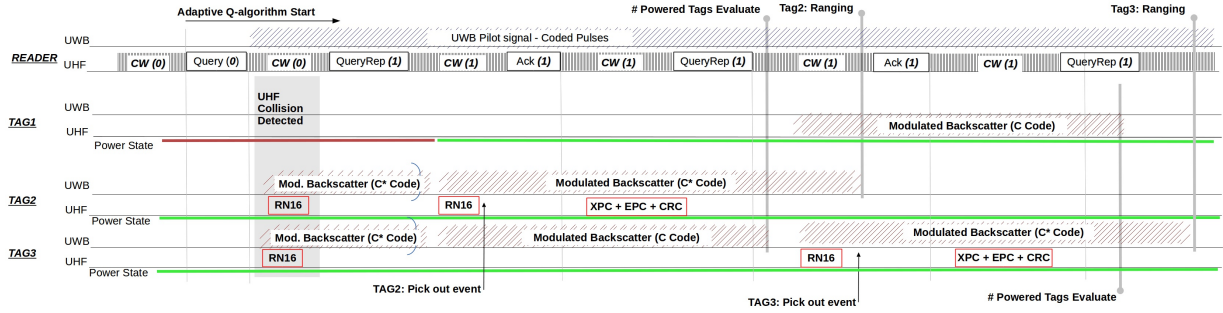


Figure 10: Example of UWB and UHF signal in the adaptive Q-algorithm, highlighting the UWB link tag use, the estimated number of tags (c_n code) and ranging (c_n^* code).

implementation of the Greta architecture. However its implementation requires the design of what usually included in a standard UHF chip (e.g., the UHF backscatter modulator) and of a more complex ad-hoc control logic which has to manage both the standard-compatible UHF protocol stack and the UWB communication protocol.

3.6 UWB Parameters Choice

For the UWB component, the transmitting power P_t has been chosen compliant to the emission limit in the 3.1-4.8GHz band. Increasing N_s improves the tag reading range (higher processing gain) but the total packet time should not exceed the typical Gen.2 reading time in order to not limit the refresh rate. The chip rate has been kept as low as possible to minimize the power consumption of the switch.

In the following table the list of parameters obtained as a compromise between the various aspects underlined before is reported. Note that the UWB-related parameters are the same for all modes except for the packet length (number of bits to be transmitted), here indicated as 2, where in mode 2 has to be increased to accommodate the tag ID and sensor data, i.e., at least 128 bits, for an overall packet transmission time of around 170ms.

Parameter	value	units	description
Tp	100	ns	inter-pulse time
Tc	10	us	chip time
Rc	0,1	MHz	chip rate
Npc	100		pulses per chip
Nc	128		code length
Ns	12800		pulses per symbol (bit)
Ts	1280	us	symbol time
Br	0,78125	Kbit/s	bit-rate
Nr	2		packet length
Tint	2,56	ms	packet transmission time

3.7 UHF Parameters Choice

The UHF transmitted signal for the UWB-UHF Gen.2 tag architecture is regulated by the standard. Protocol parameters and corresponding values for Gen.2 are reported in the following table 1.

Table 1: UHF Gen2 Parameters.

Parameters	Values
TARI	$12.5\mu s$
DATA0	$12.5\mu s$
DATA1	$18.75\mu s$
RTrate	64kbs
RTcal	$31.25\mu s$
TRcal	$64\mu s$
DR	8
LF	125kHz
M	<u>1,2,4,8</u>
TRRate	<u>125, 64.5, 31.25, 15.625 kbps</u>
Tpri	$LF \rightarrow 8\mu s$
TtoR Preamble	$6 \times Tpri \rightarrow 48\mu s$
TtoR End-of-Signaling	$2 \times Tpri \rightarrow 16\mu s$
Delimiter	$12.5\mu s$
RtoT Preamble	$120.25\mu s$
RtoT FrameSync	$56.25\mu s$
T1	$\text{Max}\{RTcal, 10 \times Tpri\} \rightarrow 80\mu s$
T2	$5 \times Tpri \rightarrow 40\mu s$
T3	$5 \times Tpri \rightarrow 40\mu s$
Length of Query	22 bits
Length of QueryAdjust	9 bits
Length of QueryRep	4 bits
Length of RN16	16 bits
Length of ACK	18 bits
Length of NAK	8 bits
Length of EPC/ID	96 bits
Length of EPC packet	128 bits [16+96+16 bits (PC+EPC+CRC16)]
Length of UWB Start CMD (Write Command like)	66 bits
Length of UWB Start CMD Response (Response Command like)	33 bits

3.8 UWB Link Budget

In table 2 the link budget table extrapolated from deliverable D2 is reported.

3.9 Energy harvesting component

The main challenge of this topic has been the design of the circuitry aiming at guaranteeing the simultaneous operations of UHF Energy Harvesting and UWB communication. These contemporaneous dual-band functionalities are allowed by means of a diplexer, providing both matching conditions and filtering for the two operating bands. Of course the design of this component has been carried out taking into account the actual diplexer load, i.e. the dual-band antenna described in paragraph 3.12. In this design step we have considered a standard thin dielectric substrate (Taconic RF60A, $\epsilon_r=6.15$, thickness 0.635 mm) in order to verify the feasibility of the solution and its connection to the antenna. The significant dispersive behavior

Table 2: UWB Link Budget Table.

Symbol	Value & Units
f_c	ultra-wide band (UWB) central frequency
f_w	ultra high frequency (UHF) central frequency
c	Speed of Light
τ_p	Pulse Width
v	Roll-Off factor
B_W	Bandwidth
P_t	Transmitted Power
R	Adaptation impedance
T_p	Inter-Pulse time
G_{reader}	Reader Antenna Maximum Gain
G_{tag}	Tag Antenna Maximum Gain
F	Noise Figure
T_0	Reference Temperature
k_{boltz}	Boltzmann Constant
SNR_{\min}	SNR threshold
N_s	Number of Pulses per Symbol
L_p	Tag Loss
M	Supplementary Loss
d_0	reference distance
E_t	Transmitted Energy
EIRP	Effective Isotropically Radiated Power
T_{sist}	System Temperature
N_0	Noise Power Spectral Density
PG	Processing Gain
PL_{\max}	PL threshold
PL_0	path-loss (PL) at d_0
d_{\max}	Maximum Distance

of the adopted antenna needs a proper matching network in order to work correctly. The communication capabilities in the UWB band are provided by the exploitation of passive backscattering; therefore the UWB port of the diplexer will be connected to a backscatter modulator, which will be responsible for the modulation of the incoming signal by switching its impedance between the two mismatched conditions of open and short circuit terminations. For design purposes, the UWB path of the diplexer has been matched to a 50Ω termination; nevertheless a similar design procedure can be successfully followed for any other loading conditions. As regards the UHF band, the diplexer is responsible for filtering the UHF signal as well as for providing matching condition towards the following rectifier, which converts the RF incoming signal into DC output power. For the rectifying section a voltage-doubler topology, exploiting Schottky diodes SMS7630 from Skyworks, has been adopted. These functionalities are provided by the diplexer by dividing the two paths through a lumped element filter for the UHF band and a distributed element filter for the UWB band, composed by a microstrip line featuring two short-circuited stubs. Another fundamental feature requested to the diplexer is a high decoupling behavior between the two paths,

since UWB backscattering needs to be completely transparent to UHF operations and vice-versa. Since the adopted UWB-UHF antenna has no ground plane, its radiation pattern is bi-directional and the presence of nearby circuitry metallization can highly deteriorate antenna performance. For this reason several diplexer topologies have been investigated focusing on preserving the radiating properties of the antenna while at the same time ensuring a low-profile structure. With these constraints, a 1-cm² microstrip/lumped elements diplexer has been designed on the Taconic RF-60A substrate, which runs parallel to the antenna substrate. The connection between the UWB-UHF antenna and the diplexer has been realized by means of a balanced line departing from the central part of the spiral: in this way a balun-free transition from the balanced-to-unbalanced architectures can be realized (see Fig. 11). Increasing circuit dimensions would lead to a degradation of the ungrounded antenna performance, especially for the higher frequencies of the UWB band: for this reason a miniaturization of the diplexer circuit is mandatory.

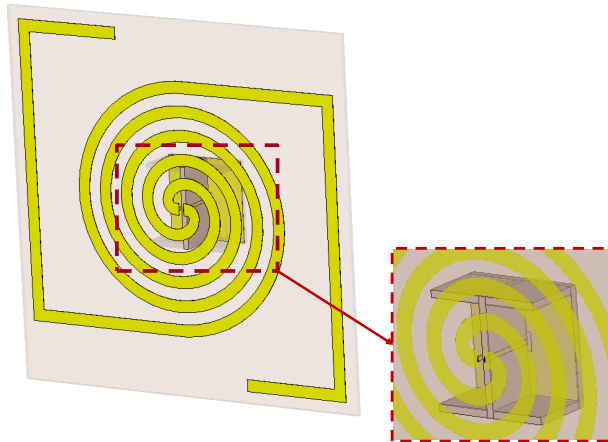


Figure 11: Diplexer-antenna connection.

The diplexer, which is shown in Fig. 12, is mainly composed of three sections: the microstrip UWB matching and filtering circuit, the lumped elements UHF matching and filtering circuit, and the rectifying section. In order to realize the requested topology on 1-cm² area the 32.5 mm-long microstrip line composing the UWB path has been meandered; this line is 0.3 mm-wide while the two short-circuited stubs are 5.5 mm-long and 0.7 and 0.5 mm-wide, respectively. As regards the UHF path and the rectifying section, the UHF filter is merely composed of a series inductance L1 and a parallel capacitance C1. Two Schottky diodes are employed in the rectifier, after which an optimum load of 6.5 kΩ has been used. The aforementioned parts are all commercially-available components, of which the models employed are listed in Table I.

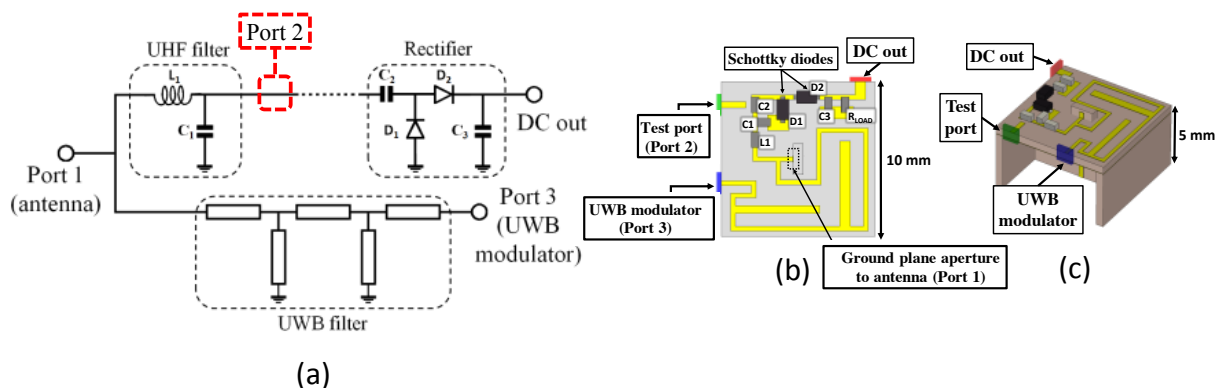


Figure 12: Diplexer (a) schematic; (b) layout top view, (c) perspective view.

Part name	Manufacturer	Product code	Value
C1	Murata	GRM0225C1C1R5CD05D	1.5 pF
L1	Coilcraft	0402HP-15NXGLU	15 nH
C2 - C3	Murata	GJM1555C1H100FB01D	10 pF
D1 - D2	Skyworks	SMS-7630 (package SC-79)	

Table 3: UHF components list.

The proposed diplexer exhibits very good matching performance as well as isolation between the two bands. In order to evaluate the matching and filtering capabilities, a testing port (Port 2) has been added before the rectifying section, thus allowing a three-port scattering parameters extraction. A $(20-j250)$ Ω termination at Port 2 has been taken into account, as an average, low-power level input impedance of the nonlinear rectifier. In Fig. 13 the simulated scattering parameters of the above-described three-port network are provided. It can be noticed that the insertion loss is less than 1 dB in the UWB band while the transmission coefficient is slightly below 2 dB at 868 MHz; at the same time high decoupling between the two bands is guaranteed.

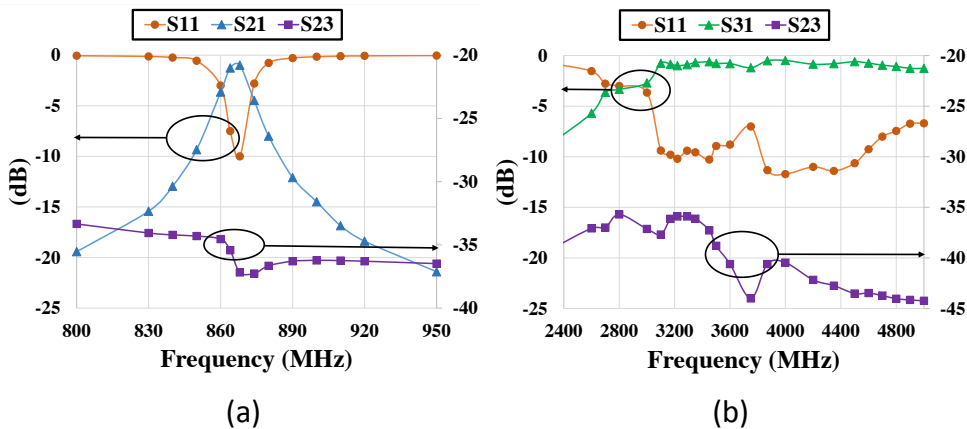


Figure 13: Simulated scattering parameters of the diplexer of Fig. 12: (a) UHF band, (b) UWB band.

Similar performance have been obtained with the corresponding solution on paper substrate. In this case the higher paper losses cause a worse insertion loss, but always about than 2 dB in both bands. In order to successfully provide the demanded functionalities during all the tag operating conditions, the highest decoupling behavior between the UHF and the UWB frequency bands is mandatory. For this reason a further inspection of the diplexer performance under different operating circumstances has been conducted. During the UWB backscattering communication, the UWB modulator switches its impedance from an open circuit to a short circuit condition; these extremely different loads values could affect UHF behavior too, if not properly decoupled. Fig. 14(a) shows UHF filtering and matching performance for all the UWB different operating conditions, for the paper-based diplexer; this result clearly shows how the high decoupling provided between the two operating bands guarantees a correct UHF operation. On the other side, rectifying operation in the UHF band could affect the UWB communication, especially because of the non-linearity introduced by the rectifying section. For this purpose the insertion loss introduced by the UWB microstrip path is evaluated for different levels of the incoming RF signal, as depicted in Fig. 14(b). Once again, high decoupling proves to be guaranteed, allowing completely transparent operations between the two operating bands.

In order to provide simultaneous recovery of RF energy while communicating in the UWB band, a

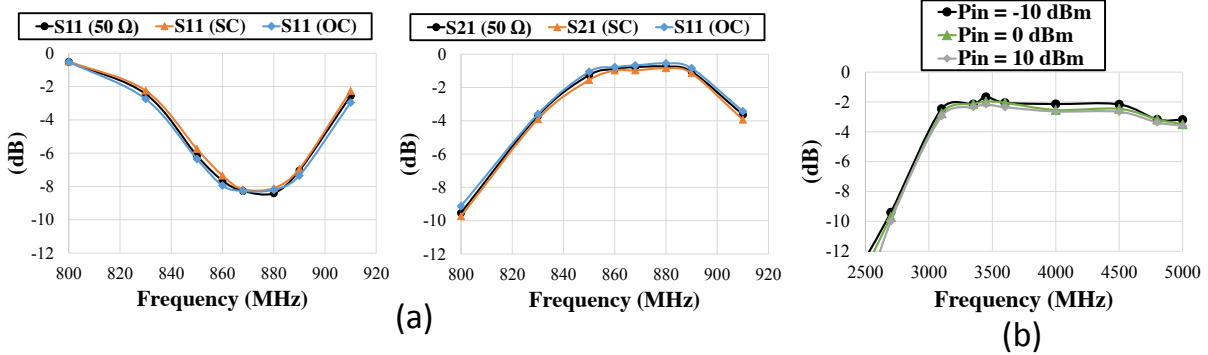


Figure 14: Simulated results of paper-based diplexer: (a) UHF matching and filtering performance distortion during the UWB modulation (SC = Short Circuit, OC = Open Circuit); (b) UWB band insertion loss for different incident RF power levels.

non-linear/electromagnetic co-simulation of the whole circuit has been carried out, including real component models, and taking into account the dispersive behavior of the antenna, with the goal of maximizing the RF-to-DC conversion efficiency. Since RF energy harvesting has to deal with typically low-levels of incoming signals, the optimization has been mainly focused on incoming available RF power ranging from -15 to -5 dBm. The resulted conversion efficiency, in optimum loading conditions, for the Taconic diplexer is shown in Fig. 15 for this range of available RF input power: promising values from 50 to 60 % are clearly observed.

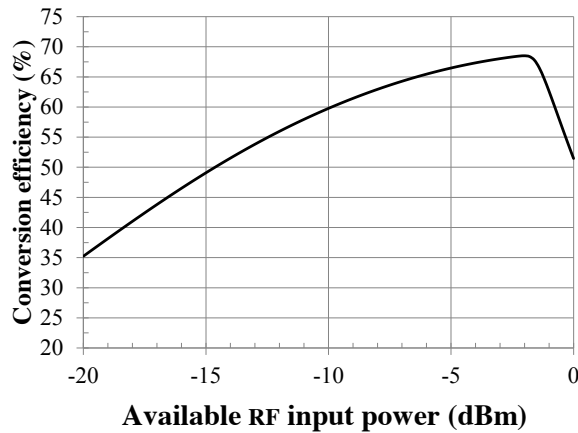


Figure 15: RF-to-DC conversion efficiency for low-levels of incoming RF available power.

3.10 UWB backscatter modulator

Passive tags are generally characterized by a backscattering modulator in order to perform the modulation reducing the circuit complexity and the power consumption. The modulation is performed by varying the load impedance (reflection due to mismatch) of the tag TX-RX antenna (see Fig. 16(a)). The modulation technique adopted in the present project for the UWB tag is the phase shift keying (PSK) (called also binary PSK). The different antenna load conditions required by this kind of modulation can be obtained by means of an open circuit (OC) and a short circuit (SC) at the antenna terminals (see Fig. 16(b)): in the two cases the total reflection is achieved with a phase difference between them equal to 180 degrees.

The technical specifications of the backscatter modulator, in agreement with the UWB communication

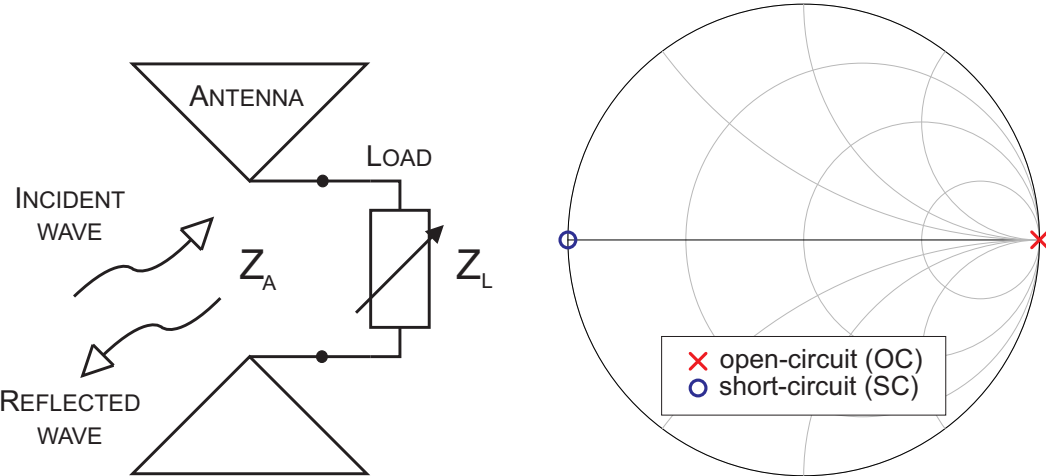


Figure 16: Backscatter modulator operating principle (a). OC and SC on the Smith chart (b).

standards, are resumed in Table 4.

Table 4: UWB backscatter modulator specification.

Parameter	Value	Description
T_{SW}	1-2 ns	switching time
T_S	10 us	average symbol time
f_S	100 kHz	average switching frequency
B_W	3.1-4.8 GHz	operating frequency band
P_C	10 uW (optimal) - 100 uW (maximum)	power consumption

Firstly, a tolerance analysis of the backscatter modulation performance is presented in Sec. 3.10.1 varying the magnitude and the phase of the modulator reflection conditions. After, the backscattering modulator has been designed exploiting lumped components. The preliminary results are resumed in Sec. 3.10.2. Then, the preliminary simulations results of the IC switch are presented in Sec. 3.10.3.

3.10.1 Analysis of the modulation performance

In this section, an analysis about the effects of the reflection coefficients on the reflected signal and, thus, on the modulation performance is carried out. In particular, in an ideal case the magnitude of the reflection coefficients and their phase difference must be equal to 1 and 180 degrees, respectively, in order to maximize the PSK modulation performance. The analysis has been performed exploiting the software MATLAB.

Firstly, a Gaussian signal with the desired spectral signature is generated in the time domain (Fig. 17) and converted in the frequency domain. Then, the signal has been multiplied for the reflection coefficients of the OC and the SC. In the ideal case they are respectively 1 and -1 (which correspond to a phase difference of 180 degrees), but in the present case the OC has been fixed to one and the SC has been varied to evaluate the performance reduction. In particular, the amplitude of the SC has been varied between -3 and 0 dB and its phase between 180-45 and 180+45 degrees. Then, after a conversion in the time domain, the energy of the signal obtained from the difference of the signals reflected from the OC and the SC, computed by exploiting the Eq. 5, and normalized with respect to the maximum value (obtained for OC and SC equal to 1 and -1) has been evaluated (Fig. 18).

The results highlight that the energy is affected by both the reflection amplitude and phase. For example, an energy reduction of about 73% can be noticed for a phase error of ± 45 degrees, fixing the

amplitude to 0 dB, and for a reflection magnitude equal to -3 dB, fixing the phase error to 0 degrees.

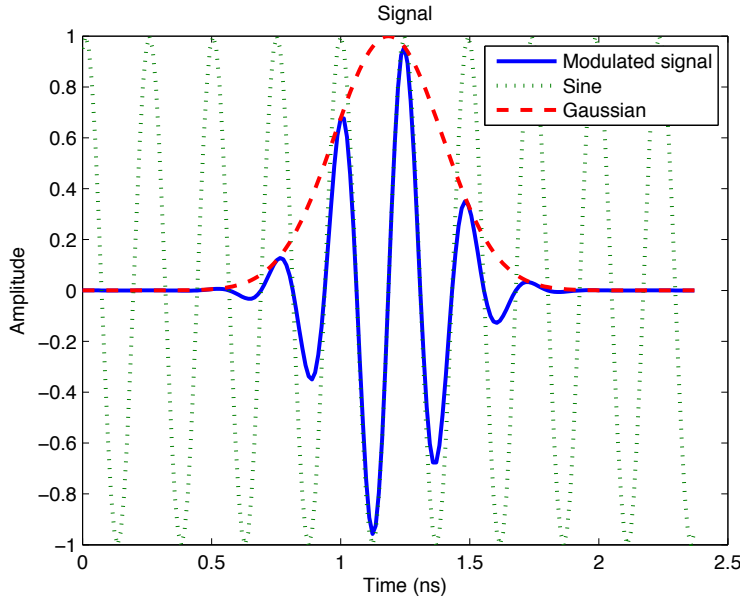


Figure 17: Modulated gaussian signal in the time domain.

$$\int |S_{OC}(t) - S_{SC}(t)|^2 dt \quad (5)$$

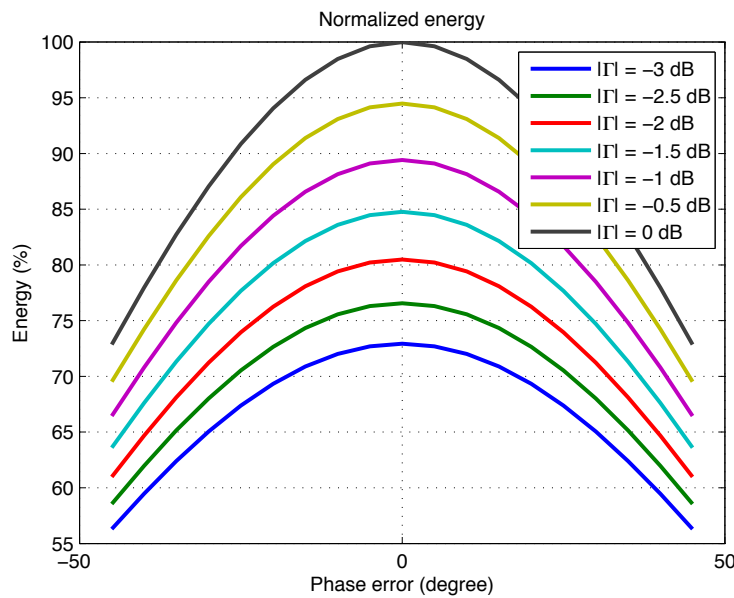


Figure 18: Normalized energy versus the reflection coefficient amplitude and phase error.

3.10.2 Lumped-elements based modulator

In this section the proposed topologies of the backscattering modulator based on lumped components are shown and the results are reported. Several circuit topologies have been designed, fabricated and measured. Each following subsection deals with one switch topology.

All the switches are designed considering the source impedance equal to 50 Ohm. The measurements have been performed by means of a vector network analyzer (VNA) for the two operating conditions, the OC and the SC. Voltages equal to 0V and 1V are respectively used in the OC and SC conditions. The magnitude of the reflection coefficients, ideally equal to 1 (0 dB), and the phase, in particular the phase difference of the two conditions that should be equal to 180 degrees, have been analyzed.

The proposed solutions are based on available on-the-shelf components. Transistors and diodes have been selected in order to have good performance in the desired frequency band. In particular, the adopted FET transistor is the VMMK1225 and the PIN diode is the SMP1322-040, both selected in order to operate in the desired frequency range. Thus, the overall switches performance are strictly related to the devices used. However, it can be noticed that the effects of the parasitics and the inaccuracy of the diode SPICE model reduce the performance of the prototype, in particular for the diode based switches, in comparison with the simulations. Other diodes models are under investigation.

The power consumption of these solutions has been already discussed in the previous deliverables. Resuming, transistor based solutions are characterized by the only dynamic power consumption while diode based ones have also the static power consumption, increasing in this way the overall power consumption of the backscattering modulator.

The lumped elements based solution, suitable for the demonstrator, is the unbalanced FET based switch. This solution, the simplest one in terms of layout and components (no DC feeds and no DC blocks required), provides a 50 Ohm input line and its phase difference varies close to 180 degrees in spite of the reflection coefficient in the SC condition equal to about -3 dB. The maximum gate-source voltage supported by the transistor is 1V: a voltage divider can be adopted in case of higher control voltages.

3.10.2.1 Unbalanced single FET switch

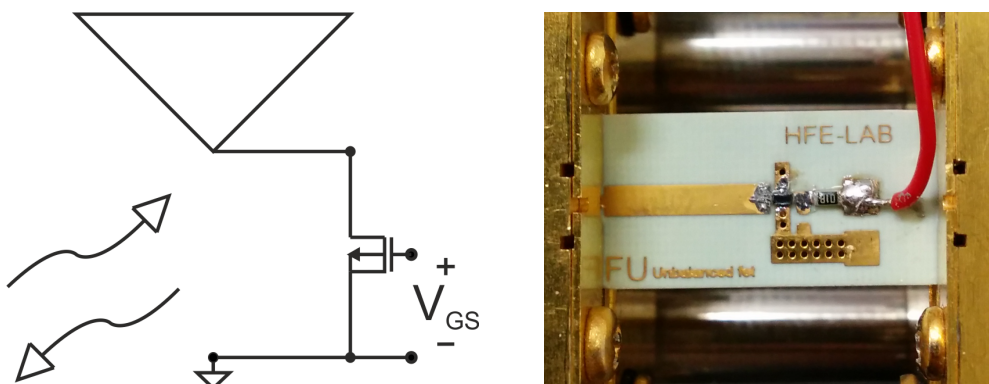


Figure 19: Schematic (a) and prototype (b) of the unbalanced single FET switch.

The schematic and the prototype of the unbalanced FET switch are shown in Fig. 19. The measurements and the simulations are compared in Fig. 20. The measured values are plotted after the de-embedding of the 50 Ohm input line. In particular, the phase difference varies between 191 and 137 degrees, the reflection coefficient in the SC state is about -5 dB and that one in the OC state is about 0 dB.

Resuming, the main characteristic of this switch are:

- 50 Ohm input impedance;
- unbalanced solution;
- 1V control voltage;
- dynamic power consumption only;
- phase difference between 191 and 137 degrees;
- reflection coefficient in the SC state of about -5 dB;
- reflection coefficient in the OC state of about 0 dB.

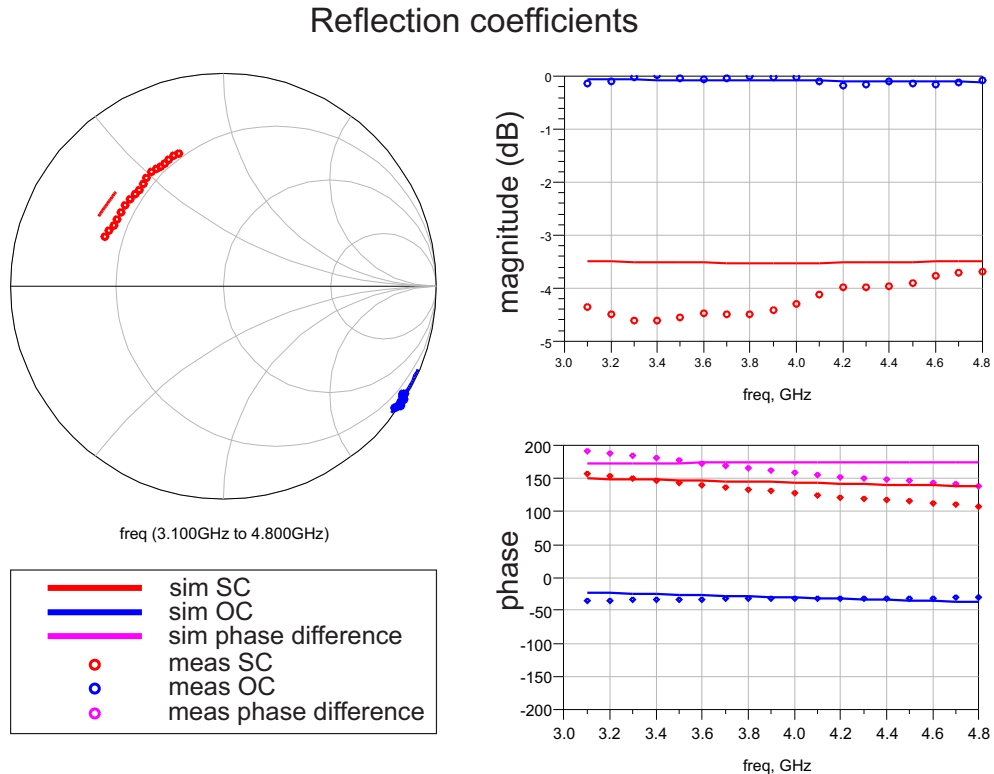


Figure 20: Measurements vs. simulations of unbalanced single FET switch.

3.10.2.2 Balanced single FET switch

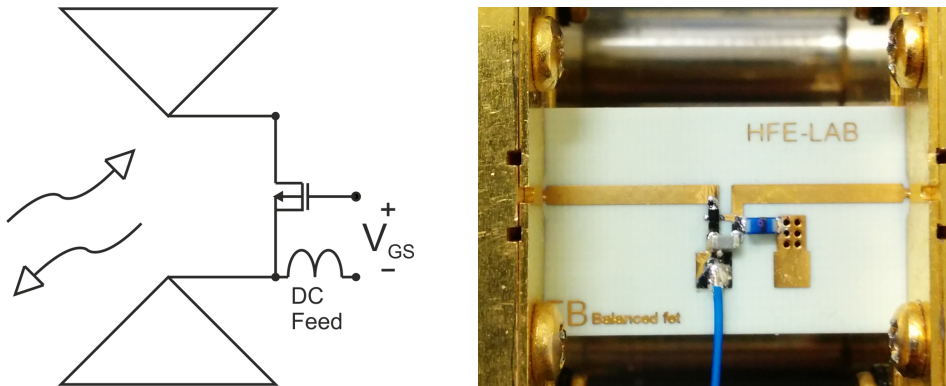


Figure 21: Schematic (a) and prototype (b) of the balanced single FET switch.

The schematic and the prototype of the balanced FET switch are shown in Fig. 21. The measurements and the simulations are compared in Fig. 22. The measured values are plotted after the de-embedding of the 50 Ohm input lines. In particular, the phase difference varies between 181 and 179 degrees, the reflection coefficient in the SC state is about -3 dB and that one in the OC state is about -0.4 dB.

Resuming, the main characteristic of this switch are:

- 50 Ohm input impedance;
- balanced solution;
- 1V control voltage;
- dynamic power consumption only;
- phase difference between 181 and 179 degrees;
- reflection coefficient in the SC state of about -3 dB;

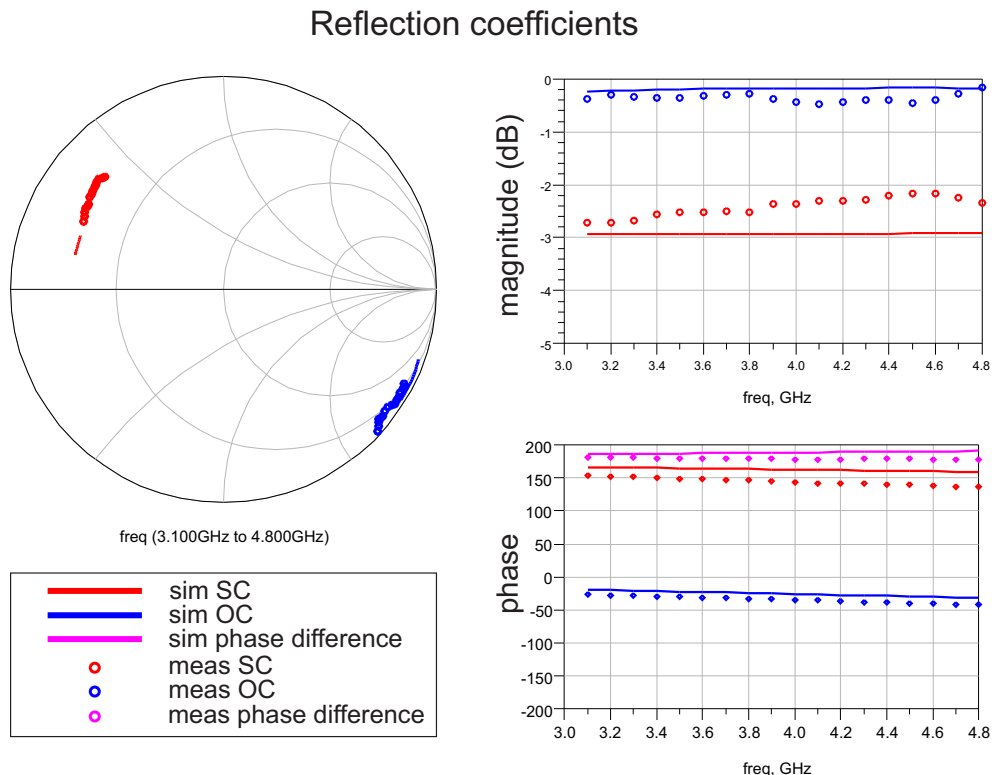


Figure 22: Measurements vs. simulations of the balanced single FET switch.

- reflection coefficient in the OC state of about -0.4 dB.

3.10.2.3 Unbalanced single diode switch

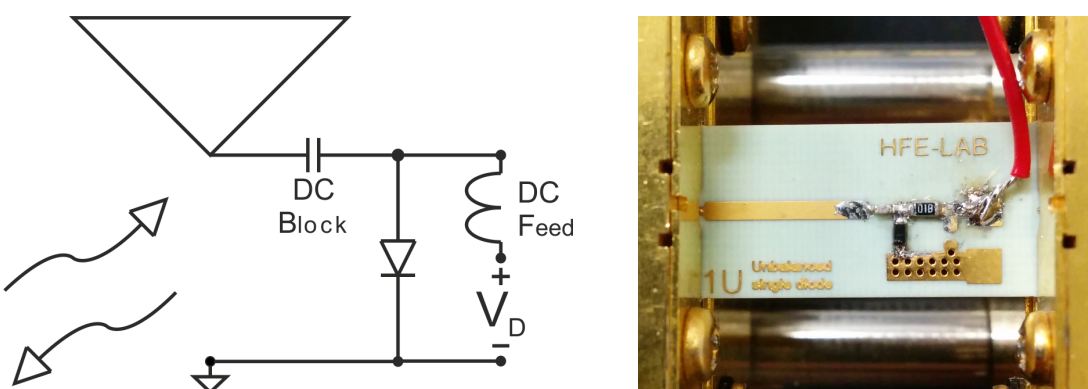


Figure 23: Schematic (a) and prototype (b) of the unbalanced single diode switch.

The schematic and the prototype of the unbalanced diode switch are shown in Fig. 23. The measurements and the simulations are compared in Fig. 24. The measured values are plotted after the de-embedding of the 50 Ohm input line. In particular, the phase difference varies between 242 and 257 degrees, the reflection coefficients in both SC and OC state are about -0.5 dB.

Resuming, the main characteristic of this switch are:

- 50 Ohm input impedance;
- unbalanced solution;
- 1V control voltage;

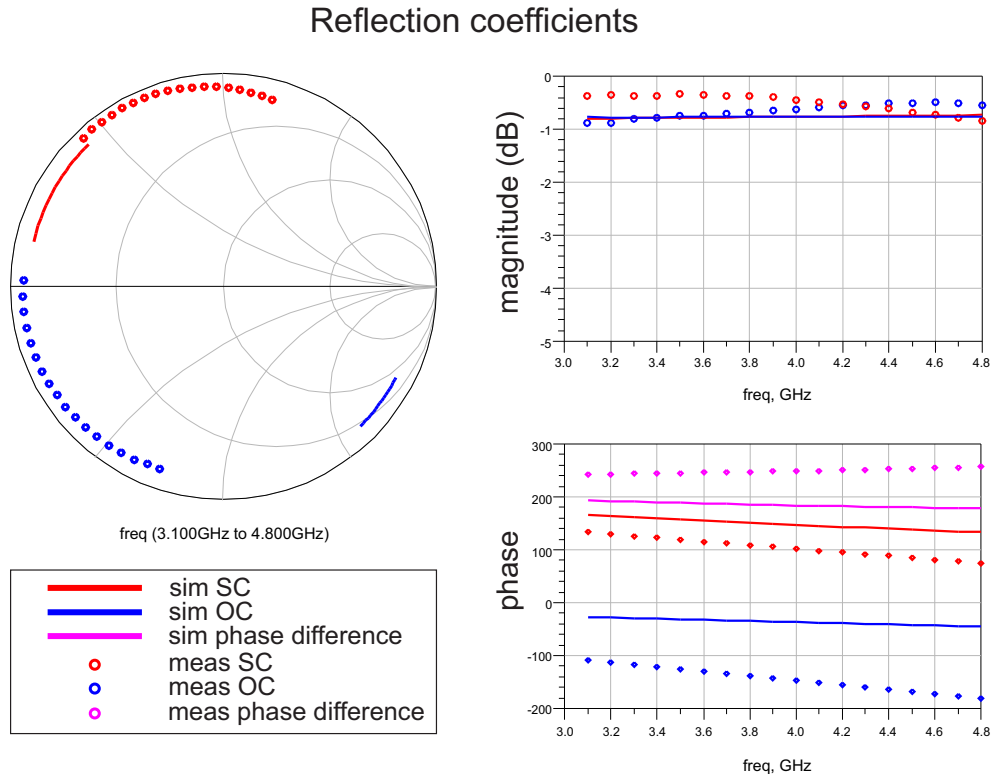


Figure 24: Measurements vs. simulations of the unbalanced single diode switch.

- dynamic and static (SC state) power consumption;
- static power consumption of 0.22 mW;
- phase difference between 242 and 257 degrees;
- reflection coefficient in the SC state of about -0.5 dB;
- reflection coefficient in the OC state of about -0.5 dB.

3.10.2.4 Balanced single diode switch

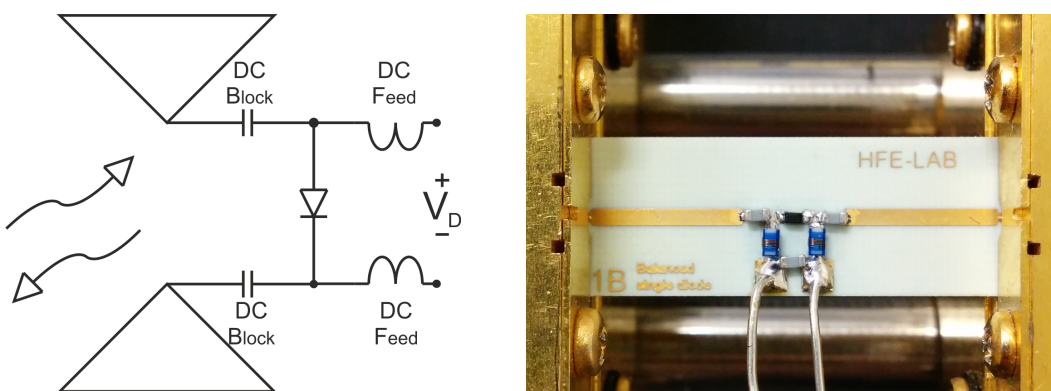


Figure 25: Schematic (a) and prototype (b) of the balanced single diode switch.

The schematic and the prototype of the balanced diode switch are shown in Fig. 25. The measurements and the simulations are compared in Fig. 26. The measured values are plotted after the de-embedding of the 50 Ohm input lines. In particular, the phase difference varies between 268 and 327 degrees, the reflection coefficient in the SC state is about -2.5 dB and that one in the OC state is about -0.5 dB.

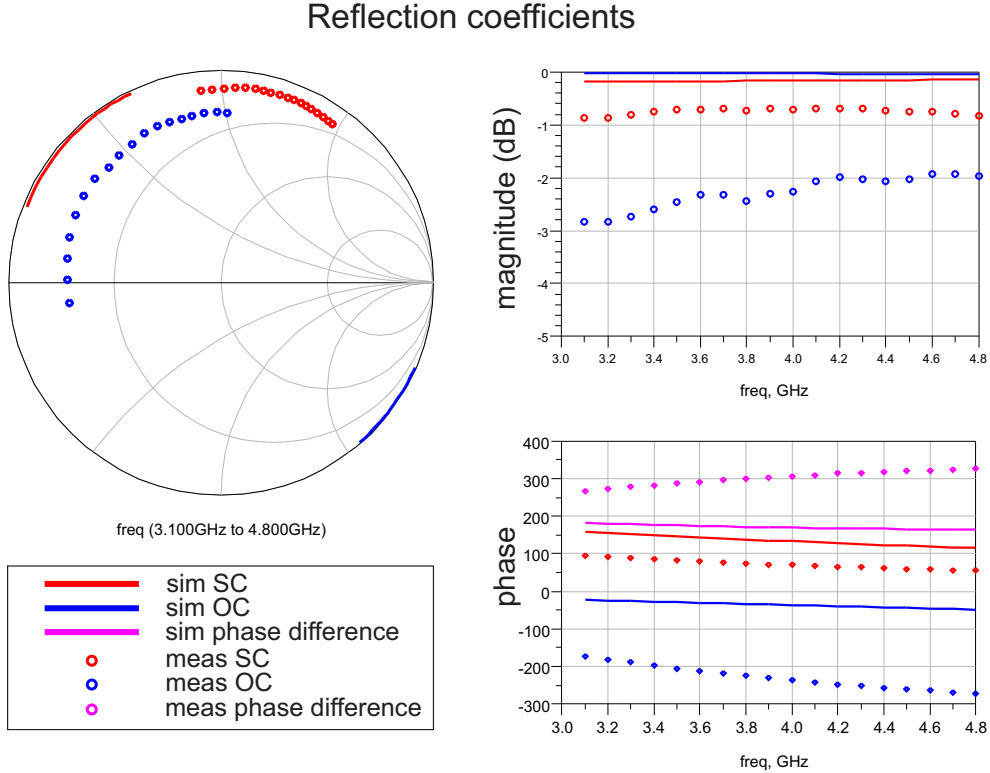


Figure 26: Measurements vs. simulations of the balanced single diode switch.

Resuming, the main characteristic of this switch are:

- 50 Ohm input impedance;
- balanced solution;
- 0.75V control voltage;
- dynamic and static (SC state) power consumption;
- static power consumption of 1.7 mW;
- phase difference between 268 and 327 degrees;
- reflection coefficient in the SC state of about -2.5 dB;
- reflection coefficient in the OC state of about -0.5 dB.

3.10.3 IC modulator

The technology proposed for the design of the IC backscattering modulator is the UMC Low-voltage CMOS 180nm (or UMC L180). The fundamental advantages of the proposed CMOS technology are its low cost, the low gate delay (or logic gate propagation delay) lower than 60ps, and the presence of zero and low voltage threshold devices models.

The IC modulator has been firstly analyzed in the frequency domain in the two operating conditions: the OC and the SC. The schematic of the switch is shown in Fig. 27: an inductor is adopted to compensate the capacitive effect of the transistor. The transistor and the inductor have been optimized in order to obtain the magnitude of the reflection coefficients close to 1 (0 dB), and a phase difference between the two conditions (OC and SC) close to 180 degrees, such as in the lumped elements switches previously analyzed.

The simulation results are plotted in Fig. 28. In particular, the phase difference varies between 179 and 176 degrees, the reflection coefficient in the SC state is about -3 dB and the that one in the OC state is about -1 dB.

The results obtained depend on the trade-off between the parasitics elements of the IC transistor: its

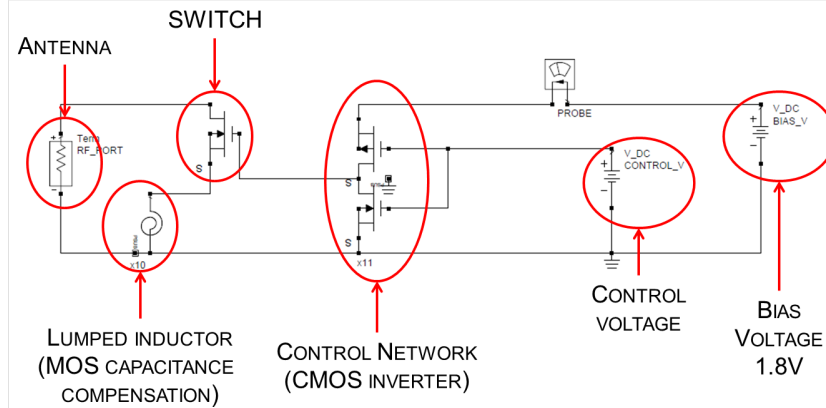


Figure 27: IC modulator schematic.

channel resistance R , and drain-source capacitance C . Both of them depends on its dimension, in particular, by increasing it, R decreases and C increases. The resistance affects the SC state reflection level while the capacitance affects the phase difference between the two states (trade-off between reflection level and phase difference). The phase error has been compensated with an inductor affecting the reflection level because of its quality factor. However, it results to be the best compromise by comparing the cases with and without inductor in terms of modulation performance exploiting the energy plot in Fig. 18.

Reflection coefficients

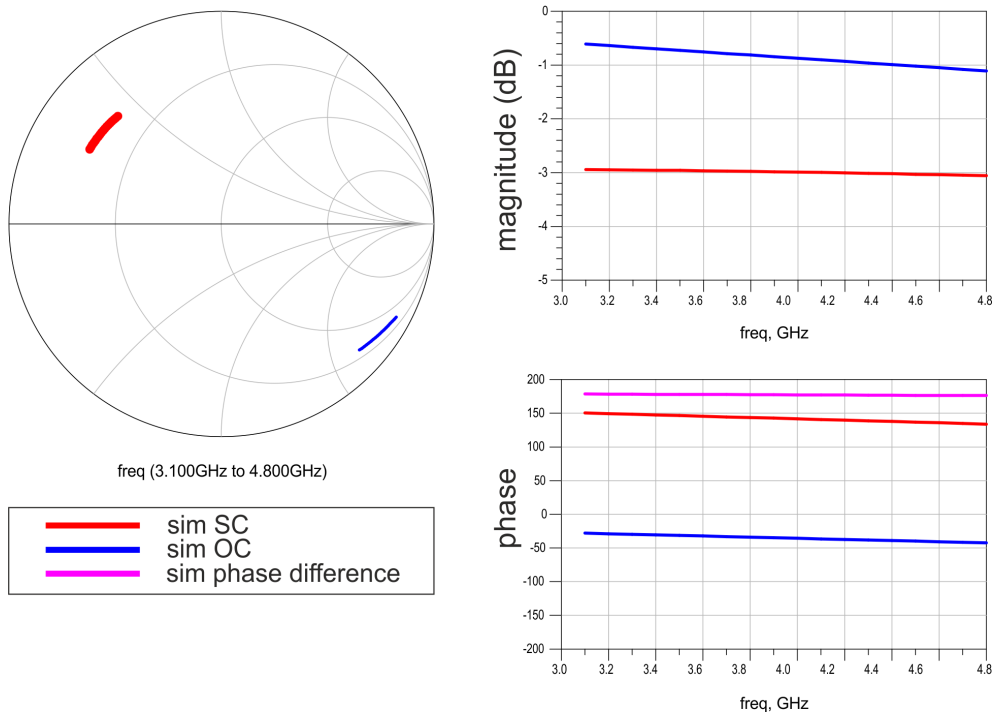


Figure 28: Simulated frequency response of the IC switch.

The backscattering modulator has been analyzed also in the time domain in order to evaluate its time response. The signals in the time domain are plotted in Fig. 29. The red curve is the voltage at the switch transistor gate and the blue one is the control voltage at the input of inverter used to control the UWB switch. The plot highlights that the high-to-low (SC-to-OC) and the low-to-high (OC-to-SC) transition times are lower than 1 ns. The time response depends on the time constant $\tau = RC$, where C is the

transistor gate-source capacitance and R the resistance of the inverter used to control the switch. For this reason a trade-off between the transition time and the transistor dimensions, which affect its gate-source capacitance and channel resistance is required: in order to have a faster response a smaller capacitance is required, increasing the channel resistance and the SC state reflection level.

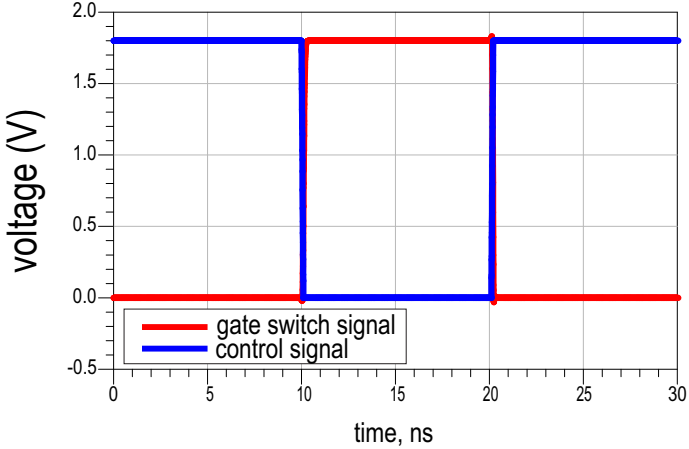


Figure 29: Simulated time response of the IC switch.

The power consumption details of the IC backscattering modulator are resumed in Table 5 defining the dynamic power consumption as $P_D = V_{HIGH}^2 C_{MOS} f_S$.

Table 5: IC backscatter modulator specification.

Parameter	Value	Description
V_{HIGH}	1.8 V	bias voltage
W	100 μm	transistor width optimized in presence of the inductor
W/L	555	transistor dimensions ratio
C_{MOS}	0.11 pF	transistor capacitance
P_D/f_S	0.36 pJ	dynamic energy consumption
P_D	36 nW	dynamic power consumption assuming an average symbols rate $T_S = 10 \text{ us}$ ($f_S = 0.1 \text{ MHz}$)

3.11 Green Technologies

This section presents the improvement in the manufacturing technique of green, eco-compatible and cost effective SIW microwave passive components. The proposed process for the implementation of SIW circuits on paper consists of two steps: the preliminary preparation of the metallized paper substrate and the manufacturing of the circuit, which requires both milling machining and subsequent metallization of the via holes.

Beside the fabrication process, the electromagnetic characterization of the involved materials is presented. Finally, the design and the measurement of several prototypes of SIW microwave devices are reported.

Substrate preparation

The preparation of the substrate requires, as a first step, the selection of a suitable type of paper with the proper thickness. The thickness of the substrate plays a role in the overall loss of SIW components: in

fact, conductor loss in a SIW structure decreases when increasing the substrate thickness, whereas the dielectric loss is independent from the thickness. Consequently, the substrate thickness should be large enough, to guarantee that conductor loss is small compared to dielectric loss. If available, a single paper sheet is adopted; otherwise, a few paper sheets can be stacked and glued, in order to reach the required thickness. Of course, the latter approach leads to a more complex (and less reliable) technological process. In this work, a single paper layer with a thickness of 500 μm has been used.

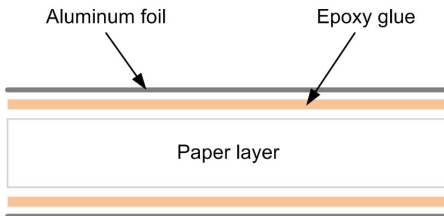


Figure 30: Side view of the metallized paper substrate, consisting of a stack of paper layer and aluminum foils, attached by epoxy glue.

Differently from traditional laminated substrates, which are commercially available with top and bottom metallization, the paper substrate requires metal sheets to be attached on both faces. To this aim, the paper sheet is embedded between two aluminum foils with a thickness of 20 μm (Fig. 30), which are attached by epoxy glue. The stack of paper sheet and aluminum foils is pressed and heated in a thermal oven for four hours at 65 Celsius degree. Since the stack is pressed while the glue is not yet completely solid, the thickness of the glue is only few microns and it results negligible with respect to the paper thickness. The main reason for using epoxy glue is the achieved stiffness of the glue layer, that permits an easy manufacturing process by milling machining, as detailed in the next Section.

Manufacturing of the SIW circuit

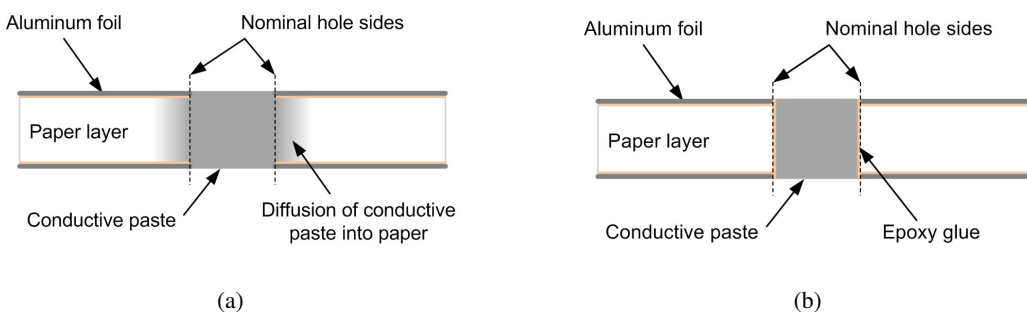


Figure 31: Effect of different techniques for the metallization of the via holes: (a) direct use of the conductive paste, with diffusion of the paste into paper; (b) preliminary coating of the hole walls by epoxy glue, which prevents conductive paste diffusion.

The manufacturing of the SIW circuit on paper is based on the use of a numerical controlled (CNC) milling machine, namely a ProtoMat E33 from LPKF Laser & Electronics AG. This machine is adopted both for the surface patterning and for the hole drilling, as in a standard PCB fabrication process. The milling machine can be equipped with two main types of tools: the spiral drills and the cutters. The first ones are employed to drill the via holes, with diameter spanning from 0.2 mm to 2 mm. The cutters are used both to etch thin gaps between strips and to remove wide areas of metal foil, and the available cutters diameter ranges from 0.15 mm to 3 mm.

Finally, the via holes of the SIW structure need to be metallized. A conductive paste is adopted to fill the drilled holes, to guarantee ohmic contact between top and bottom conductive layer. Several

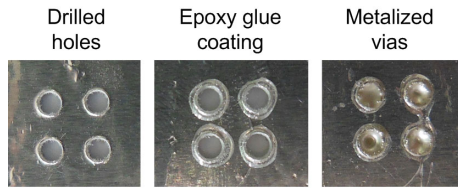


Figure 32: Photographs of the steps of manufacturing of the metalized via holes.

experiments showed that the direct use of conductive paste is critical, as the conductive paste diffuses in the substrate because of the porosity of the paper, thus jeopardizing the metallization process (Fig. 31a). To overcome this problem, a two-steps metallization process was adopted. A preliminary coating thin film of epoxy glue is distributed on the inner wall of via holes, to avoid the aforementioned diffusion effect (Fig. 31b). A fast heating process is required to cure the coating. The second step is the metallization process with the conductive paste. A final heating process in a thermal oven is required to increase the conductivity of the conductive paste. The implementation process of the metal via holes is shown in Fig. 32, with a four-hole pattern test bench.

By using this new fabrication method the costs of material and manufacturing are extremely low. Moreover, the proposed technique is suitable for SIW components and can be applied to other non-standard substrates.

Material characterization

The use of paper-based substrates for the implementation of microwave components requires a preliminary characterization of the electric parameters of the adopted materials. In particular, it is necessary to measure the dielectric permittivity and the loss tangent of paper and the conductivity of the aluminum foils.

This section presents, at first, the experimental determination of the conductivity of the aluminum foils, which is independent from the selected paper material. Subsequently, test circuits are realized on paper substrates, to determine the electric properties of paper.

Measurement of aluminum foil conductivity

The technique adopted to characterize the conductivity σ of the aluminum foils is based on a cylindrical cavity resonator, operating at 2.45 GHz on the fundamental TM_{010} mode. In fact, the quality factor of the cavity mode depends on the wall conductivity. Two cavities have been considered: in the first case, the top and bottom walls of the cylindrical cavity consist of bulky copper, while in the second case they are replaced by the aluminum foils.

The experimental setup consists of the cavity, connected through two ports to a vector network analyzer (VNA). Weak coupling is achieved by properly adjusting input/output feeding loops, in such a way that the loaded quality factor well approximates the unloaded one.

Fig. 33 shows the measured transmission coefficient of the cavity in the two cases. The unloaded quality factor can be derived from the scattering parameters and it results approximately 6000 for both cases. Because the difference between the quality factor in the two cases is negligible, the conductivity of the aluminum foil is comparable to the copper conductivity. For this reason, the conductivity value $\sigma=3.5 \times 10^7$ S/m was adopted in the simulations. In addition, Fig. 33 shows a small frequency shift of 6.6 MHz between the two resonances: this phenomenon is attributed to the small bending of the thin aluminum foils, which was confirmed by numerical simulations.

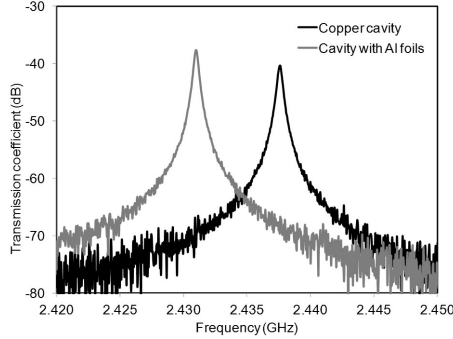


Figure 33: Measured $|S_{21}|$ of the resonant cavity adopted for the characterization of the aluminum foil conductivity: cavity with copper top and bottom (black line) and with aluminum foil (gray line).

Electrical characterization of paper

There is wide availability of different types of paper, which vary in density, thickness, and texture. However, since paper is not developed specifically for microwave applications, accurate information about its electric properties are not readily available. Therefore, it is essential to adopt a systematic process for determining the dielectric permittivity ϵ_r and the loss tangent $\tan\delta$. Several methods are currently used to characterize microwave substrates, including resonators and transmission lines. The method adopted in this work is based on the study of the frequency response of a microstrip ring resonator. This technique permits to determine the dielectric permittivity of the substrate from the analysis of the resonance frequencies of the ring, and the loss tangent from the evaluation of the quality factor of the resonant modes.

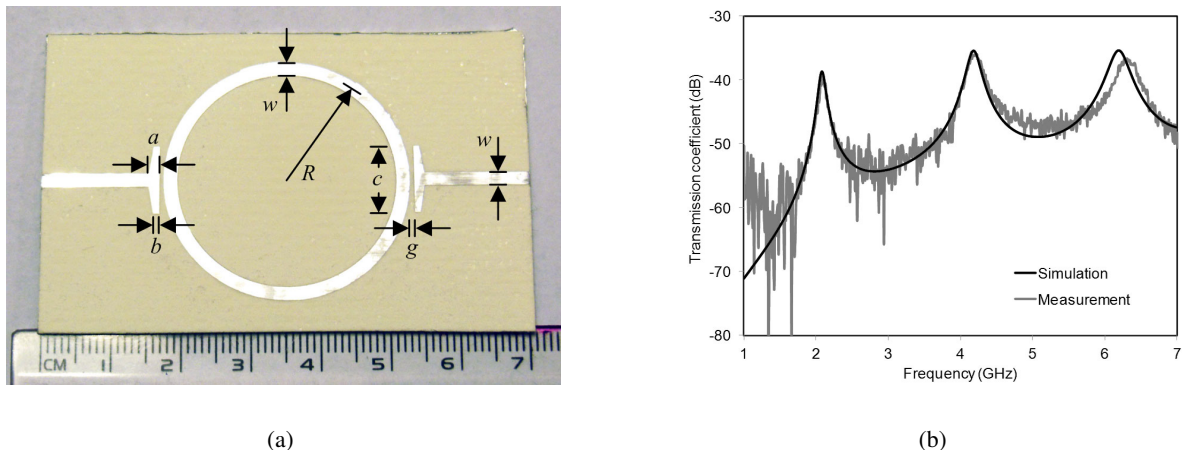


Figure 34: Example of a microstrip ring resonator on paper adopted for the material characterization (dimensions in mm: $w=1.9$, $g=0.65$, $R=16.8$, $a=1.5$, $b=0.8$, $c=9.9$): (a) photograph of the prototype; (b) simulated and measured $|S_{21}|$.

Several different types of papers have been characterized by adopting this technique. In all cases, a proper ring resonator has been designed and tested. The structure of the circuit consists of a microstrip ring, as shown in Fig. 34a, coupled to the input and output 50 Ohm microstrip lines through two gaps. The value of the gap was selected, taking into account the constraints of the manufacturing process. In the design, the terminal sections of the microstrip lines near the ring were increased to increase the capacitance, and consequently to achieve a larger coupling.

The frequency response of the ring resonator presents a set of resonances at the frequencies where the length of the ring corresponds to an integer number of effective wavelengths (Fig. 34b). As the effective

wavelength is related to the dielectric permittivity of the substrate, the value of ϵ_r is derived from the resonance frequencies of the ring resonator. Concerning the loss tangent of the paper substrate, it is mainly related to dielectric loss, as radiation loss is negligible and it was demonstrated in the previous subsection that the aluminum foils exhibit a high conductivity. Therefore, the value of $\tan\delta$ is derived from the measured unloaded quality factor, obtained from the insertion loss and the -3 dB bandwidth.

All ring resonators have been designed in order to have the first resonant frequency at 2 GHz, assuming the tentative value of dielectric permittivity $\epsilon_r=2.85$, taken from the literature.

Table 6: Electrical parameters of different types of paper substrates, derived from the measurement of ring resonators.

<i>Paper type</i>	<i>Number of layers</i>	<i>Thickness μm</i>	<i>Dielectric constant</i>	<i>Loss tangent</i>
Photographic paper	3	690	2.35	0.044
Fabriano Copy 2	6	480	2.13	0.060
Watercolor paper	1	300	2.09	0.045
Corrugated paper	1	1500	1.46	0.036
Raw paper	1	350	2.11	0.037
PM1	1	500	1.90	0.045
Momo 07	1	665	2.02	0.041
Fabriano 5	1	500	2.25	0.045
Burgo	1	500	2.20	0.040

The values of the relative permittivity and of the loss tangent of several different paper substrates, measured with the ring resonator technique, were determined, and the results are reported in Table 6. The values of ϵ_r and $\tan\delta$ were preliminarily determined by using the formulas in, and subsequently refined by using full-wave simulations to fit measurement data. The results show that the dielectric permittivity of the paper is in the range of 1.9-2.35 in the frequency band from 2 to 4 GHz for most types of paper, with the only exception of corrugated paper, which has a lower permittivity of 1.46 due to the large presence of air. The values of loss tangent range from 0.037 to 0.06.

Paper based components

Once the fabrication process achieved an acceptable level of reliability and the electromagnetic characteristics of the involved materials are known, the design, manufacturing and measurements of different passive microwave components can be done. In particular, this Section presents several SIW components based on paper substrate.

These new designs are based on Burgo paper substrate which is a thick raw paper without any final glossy treatment. The dielectric permittivity is $\epsilon_r = 2.2$ and the loss tangent is $\tan\delta = 0.04$. The most important improvement with respect of the previous designs is that the thickness of a single sheet of paper is $500 \mu\text{m}$, that allows to use a single layer as dielectric substrate for the implementation of the SIW structures.

The proposed prototypes comprise an SIW cavity, two SIW interconnections, a two-pole SIW filter based on quarter-mode cavities and a cavity-backed SIW slot antenna. All these components have been designed with the commercial electromagnetic simulator Ansys HFSS, and the measurement setup is based on the vector network analyzer (VNA) Anritsu 37347C and the universal test fixture (UTF) Anritsu 3680.

SIW square cavity

A square SIW cavity on paper is designed to resonate at 4 GHz, which is the middle of the lower part of the standard UWB frequency band. The excited fundamental mode is the TM_{110} . The layout of the square SIW cavity is illustrated in Fig. 35a. The side dimension of the optimized cavity is $a=b=36.5 \text{ mm}$ in order

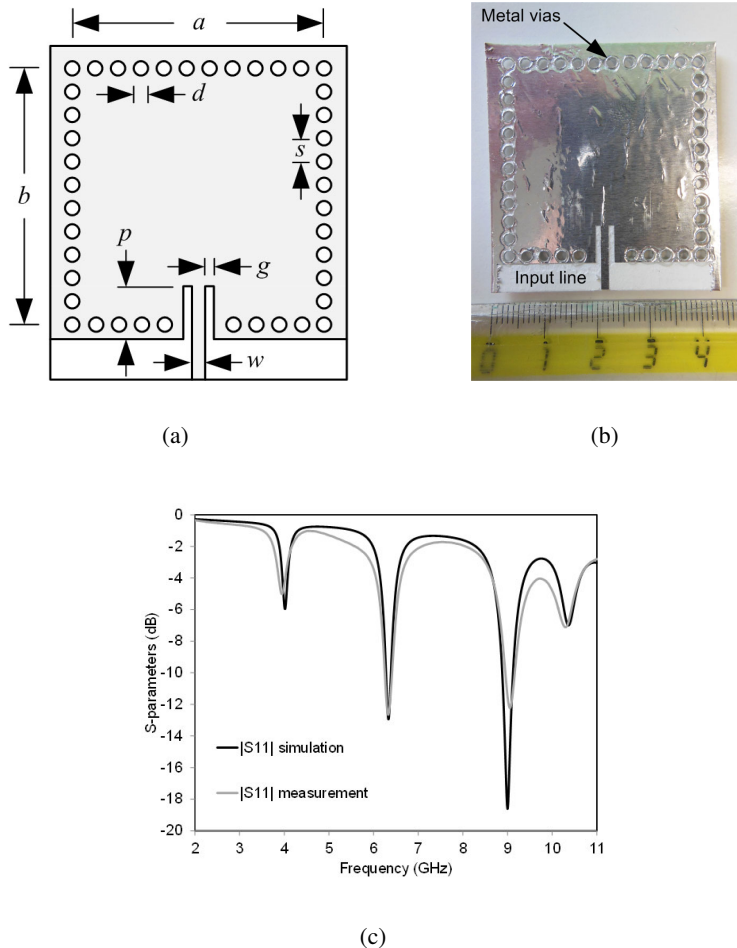


Figure 35: SIW cavity resonator on paper: (a) drawing of the SIW cavity (dimensions in mm: $a=b=36.5$, $d=2$, $s=4$, $w=1.6$, $g=1$, $p=7$); (b) photograph of the prototype; (c) simulated and measured $|S_{11}|$ of the cavity resonator.

to center the desired resonant frequency, the via holes have a diameter of $d=2$ mm, and their spacing is $s=4$ mm (that is the double of the diameter), to practically avoid radiation leakage. The cavity is fed by a 50 Ohm microstrip line, with two symmetric insets to control the coupling. The relevant dimensions of the structure are provided in the caption of Fig. 35a.

Table 7: Simulated and measured resonance frequency and quality factor of the first cavity modes.

Resonant mode	Simulated f_r (GHz)	Measured f_r (GHz)	Simulated Q_U	Measured Q_U
Mode TM_{110}	4.02	3.95	20.9	10.9
Mode TM_{210}	6.33	6.33	19.3	11.8
Mode TM_{310}	9.00	9.05	15.3	11.8

Fig. 35b shows a photograph of the prototype. The comparison of simulated and measured reflection coefficient of the circuit is shown in Fig. 35c. In the considered frequency band from 2 GHz to 11 GHz, the frequency response of the SIW cavity exhibits four poles, corresponding to four resonant modes of the cavity. The good agreement between simulation and measurement demonstrates that the values of ϵ_r and $\tan \delta$, determined at the frequency of 2 GHz in the previous section, do not change significantly over the entire frequency band. More specifically, Tab. 7 shows the simulated and measured resonance frequency f_r and unloaded quality factor Q_U of the first three cavity modes. The maximum discrepancy between

simulated and measured resonance frequencies is in the order of 2%, and a reasonable agreement was found also in the values of the quality factors.

Moreover, the resonant cavity represents the basic element for the implementation of SIW filters, as the quality factor of the cavity is related to the achievable filter selectivity. The Q_U factor of the first mode of the SIW square cavity is approximately 11. To make a comparison, the quality factor of the ring resonator fabricated on the same paper is 17. This result is not surprising, as in the case of the SIW cavity the field is completely confined inside the (quite lossy) dielectric material, whereas in the case of the microstrip ring resonator the field is partially in the dielectric material and partially in air, thus reducing the overall dielectric losses. Beside this issues, SIW cavity resonators, as well as SIW components, are completely shielded and consequently the radiation losses are negligible. This leads to the possibility of stacked more layers of SIW components without changing their frequency behaviors and also to prevent spurious perturbations from the external environment.

SIW and HMSIW interconnections

As presented before, another classical component is the straight interconnection, that is essential for the implementation of microwave circuits. As discussed the main difference between the previous prototypes is related to the substrate adopted. In this case the single sheet of Burgo paper is employed in order to keep as simple as possible the manufacturing of the susbtrate and therefore to achieve a more reliable manufacturing process. Two different topologies of SIW interconnections are proposed: the standard SIW and a half-mode SIW (HMSIW). Both interconnections exhibit tapered transitions to input and output 50 Ohm microstrip lines, in order to measure the scattering parameters of the circuits by using a vector network analyzer. The measurement setup is still the same of the previous case.

The basic SIW interconnection is designed to cover the lower part of the ultra-wideband (UWB) frequency range, from 3.1 GHz to 4.8 GHz. Consequently, the cut-off frequency of the SIW is set to $f_C = 2.5$ GHz, so that the useful band starts at 1.25 $f_C = 3.1$ GHz, according to the usual definition. To this aim, the unit cell of the SIW structure has been designed with the diameter of via holes $d=2$ mm, the longitudinal spacing $s=4$ mm, and the width of the SIW $w=40.7$ mm (Fig. 36a). The overall length of the circuit is set to $L=48$ mm, corresponding to 12 unit cells.

The photograph of the top view of the prototype is shown in Fig. 36b. The frequency response of the SIW structure is shown in Fig. 36c, where the simulated and measured scattering parameters of the paper-based SIW interconnect are reported. An overall agreement between simulation and measurement results is observed. The measured insertion loss of the SIW structure, including input/output microstrip lines and tapered transitions, is 2.83 dB at the frequency of 4 GHz. The dispersion diagram of the SIW structure is obtained by comparing two lines with different length (more specifically, a long structure with 12 unit cells and a short structure with 9 cells). The propagation constant versus frequency is shown in Fig. 36d. The attenuation constant of the SIW interconnection is estimated 0.3 dB/cm at 4 GHz.

The second interconnection based on paper substrate is the half-mode SIW. The structure is obtained by removing half of the top wall of the SIW interconnection, as well as a row of metal vias (Fig. 37a). The operation principle of this structure is based on the presence of a magnetic wall boundary condition along the cutting plane, which satisfies the boundary condition of the fundamental SIW mode. In addition, the radiation leakage through the open side remains negligible because of the low thickness of the substrate and therefore the high aspect ratio. The HMSIW exhibits two basic advantages: the size is reduced of almost 50% with respect to the standard SIW, and the single-mode bandwidth is significantly enhanced. The quasi- TE_{20} mode is not supported because of the magnetic wall condition, and the first upper mode is the quasi- TE_{30} that has the cut-off frequency three times higher with respect of the fundamental mode one.

The HMSIW was designed with the same $f_C = 2.5$ GHz of the SIW described above, thus resulting in the same longitudinal dimensions (as reported in (Fig. 37a).

A prototype of the half-mode SIW was fabricated with the described technology and its picture is reported in Fig. 37b. The simulated and measured scattering parameters are shown in Fig. 37c and

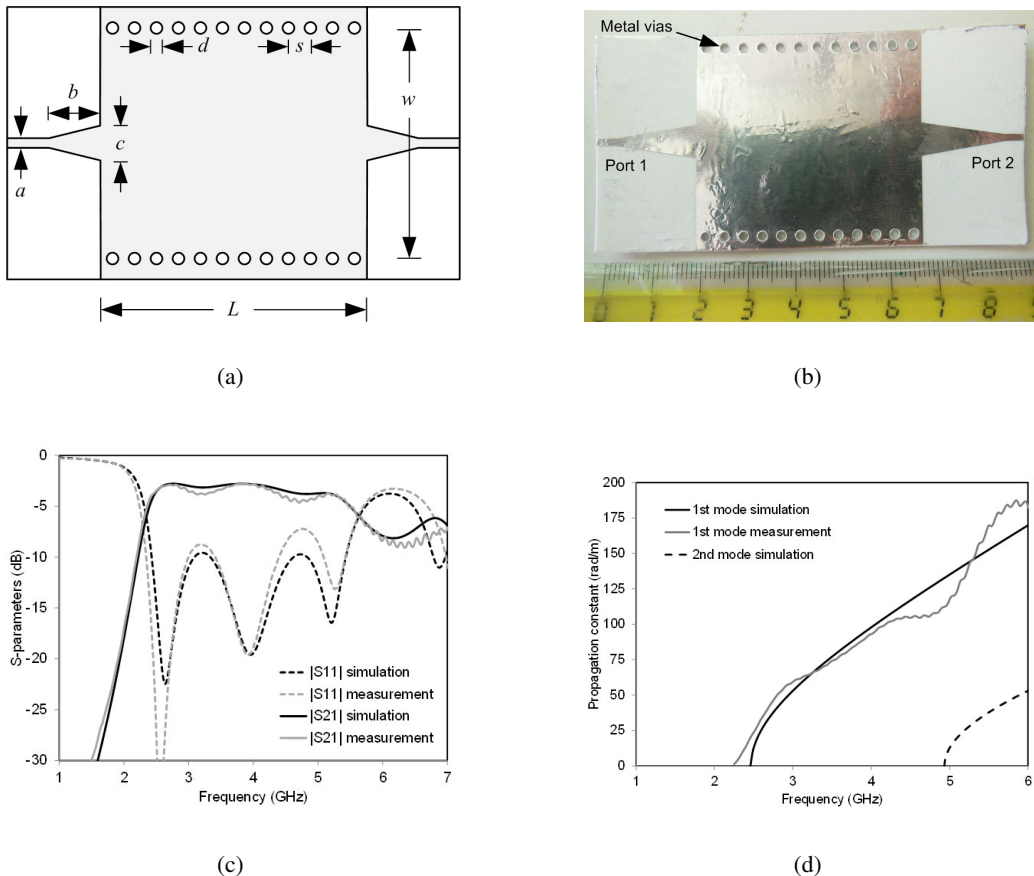


Figure 36: SIW interconnect on paper: (a) drawing of the SIW interconnect (dimensions in mm: $a=1.6$, $b=17$, $c=7.2$, $d=2$, $s=4$, $w=40.7$, $L=48$); (b) photograph of the prototype; (c) simulated and measured scattering parameters of the SIW interconnect; (d) simulated and measured dispersion diagram of the fundamental mode of the SIW interconnect.

exhibit a good agreement over the entire frequency band. Moreover, the propagation constant of the HMSIW is reported in Fig. 37d. The values of the propagation and attenuation constant of the HMSIW are similar to the ones of the standard SIW, being the only difference the much broader single-mode bandwidth. The propagation constant of the second mode starts at approximately 7.5 GHz that is out of scale in Fig. 37d.

Quarter-mode SIW filter

Another significant example presents a two-pole filter based on quarter-mode SIW cavities (Fig. 38a). The selected topology permits to minimize the filter size, as the cavity dimension is reduced of a factor four. The quarter SIW cavity exploits the same concept of the half-mode SIW structure: due to the particular aspect ratio, the two open sides of the quarter cavity practically exhibit magnetic-wall boundary conditions, thus supporting the fundamental $\text{TM}_{0.5,0.5,0}$ cavity mode.

The proposed filter consists of two quarter-mode SIW cavities, connected at one side, where the metal posts are removed. The input/output 50 Ohm microstrip lines are connected to the cavities, in the corner where the electric field assumes the maximum value.

The pass-band filter has been designed with central frequency at 4 GHz. The resulting cavity side is $w = 17.2$ mm, whereas the via diameter and spacing are $d = 2$ mm and $s = 4$ mm. The input/output microstrip lines are slightly tapered to optimize the input matching. The overall length of the device is approximately 50 mm. The dimensions of the circuit are given in detail in the caption of Fig. 38a.

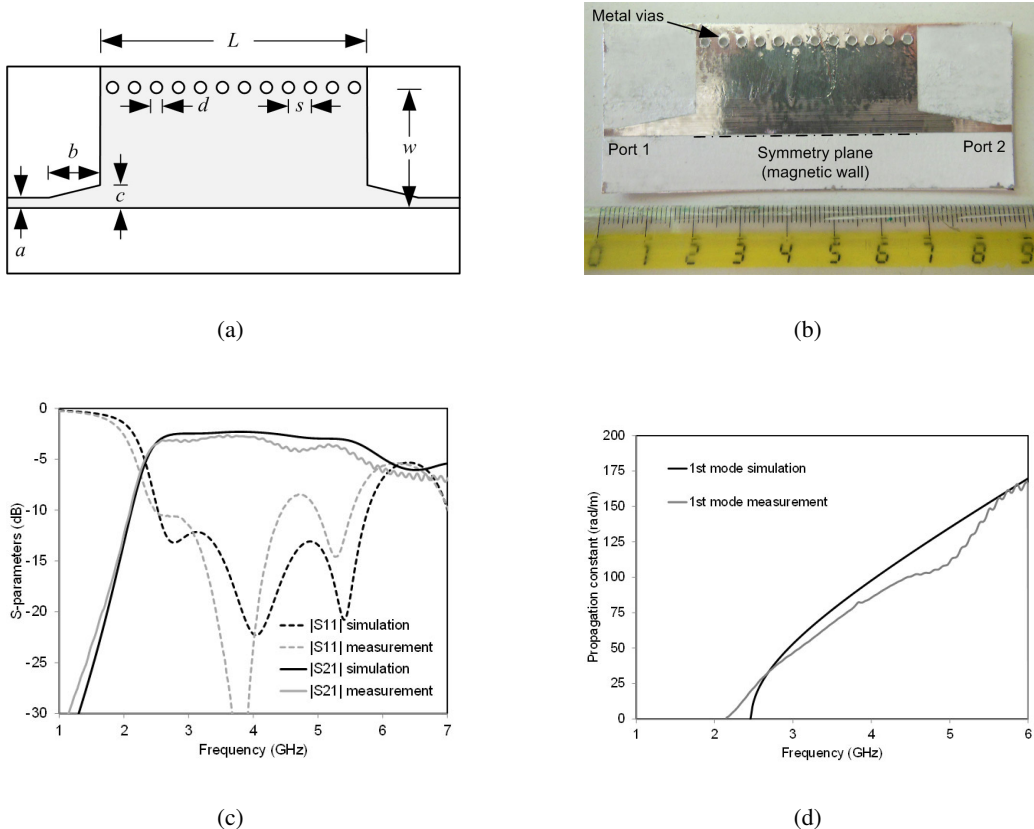


Figure 37: Half-mode SIW interconnect on paper: (a) drawing of the half-mode SIW interconnect (dimensions in mm: $a=1.6$, $b=16.8$, $c=4.8$, $d=2$, $s=4$, $w=20.4$, $L=48$); (b) photograph of the prototype; (c) simulated and measured scattering parameters of the half-mode SIW interconnect; (d) simulated and measured dispersion diagram of the fundamental mode of the half-mode SIW interconnect.

Fig. 38b shows the top view of the prototype. The simulated and measured frequency responses of the filter are reported in Fig. 38c. The measured insertion loss is 2.9 dB at the frequency of 4 GHz.

Half-mode SIW filter

One more example in band-pass filter design based on this technology is a compact half-mode SIW filter. The design is based on the excitation and control of the resonance modes of a half-mode SIW cavity.

By properly selecting the dimension and position of three insets (Fig. 45a), the resonance frequency of the cavity modes can be adjusted, in such a way that two modes determine the pass band at 4.5 GHz and the higher modes are shifted up to approximately 10 GHz (return band), thus guaranteeing a wide out-of-band region. The input matching is optimized by playing with the coupling with the input/output microstrip lines, which does not practically affect the mode resonance frequencies.

The prototype of the filter is shown in Fig. 45a the overall size is quite small, being its length less than 40 mm, including the input/output microstrip lines. The frequency response is reported in Fig. 45b and exhibits a very good agreement between simulation and measurement over the entire frequency band. The measured insertion loss is 5.0 dB at the frequency of 4.5 GHz.

Cavity-backed SIW slot antenna

One more example is a cavity-backed SIW slot antenna, operating at the frequency of 4 GHz and with linear polarization (Fig. 40a). This antenna topology exhibits some important features: because it is

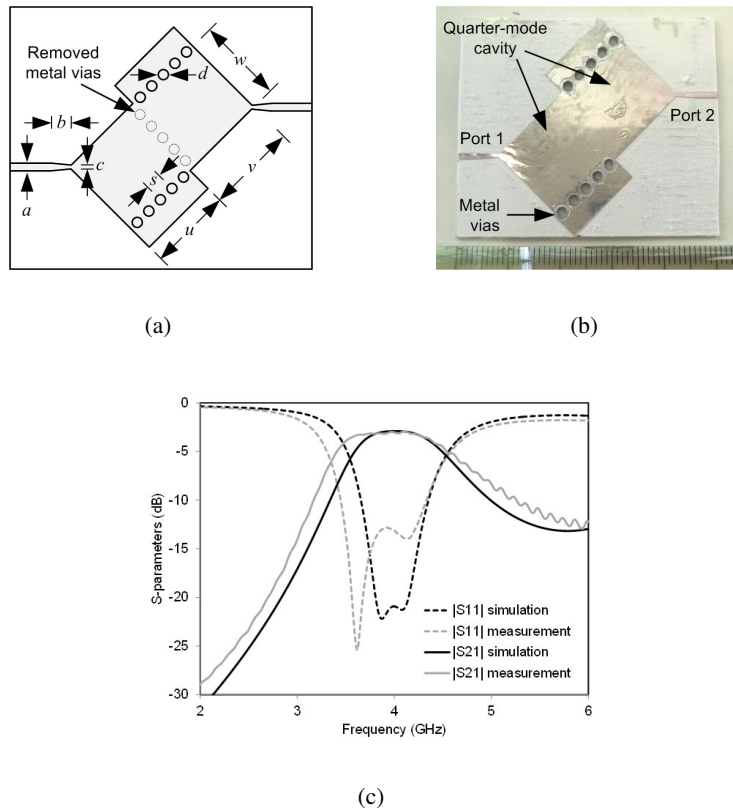


Figure 38: Quarter-mode SIW cavity filter on paper: (a) drawing of the SIW filter (dimensions in mm: $a=1.6$, $b=4.3$, $c=0.65$, $d=2$, $s=3.32$, $u=16.3$, $v=18.1$, $w=17.2$); (b) photograph of the prototype; (c) simulated and measured scattering parameters of the SIW filter.

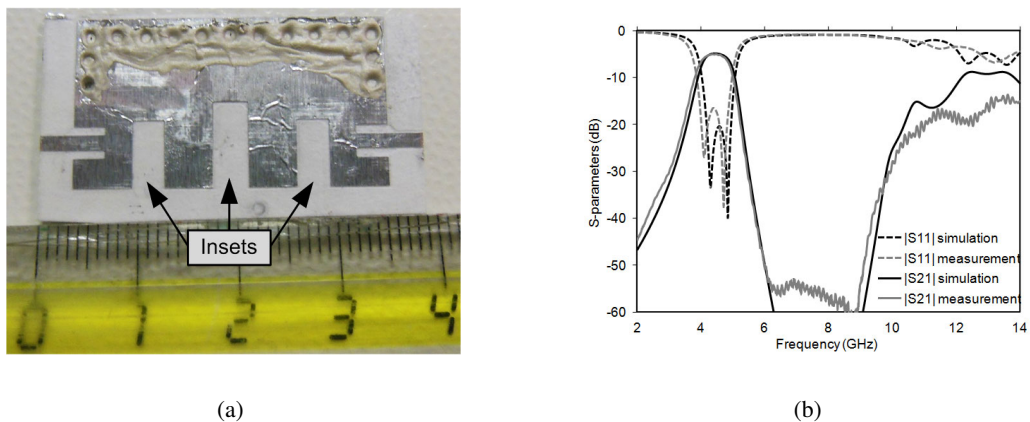


Figure 39: Low pass filter on paper substrate.

completely shielded at the sides it does not suffer from side leakage, it is less sensitive to the environment. For these reasons, this type of antenna finds useful applications in wearable systems.

The antenna consists of a square SIW cavity with a rectangular slot on a side and a feeding line on the opposite side, as depicted in Fig. 40a. The size of the SIW cavity is selected to exhibit the TM_{120} resonant mode at the frequency of 4 GHz. Similarly, the length of the rectangular slot is optimized to radiate at the same frequency. The antenna is fed by a microstrip line with two insets, designed to optimize the input matching. All dimensions of the antenna are provided in the caption of Fig. 40a.

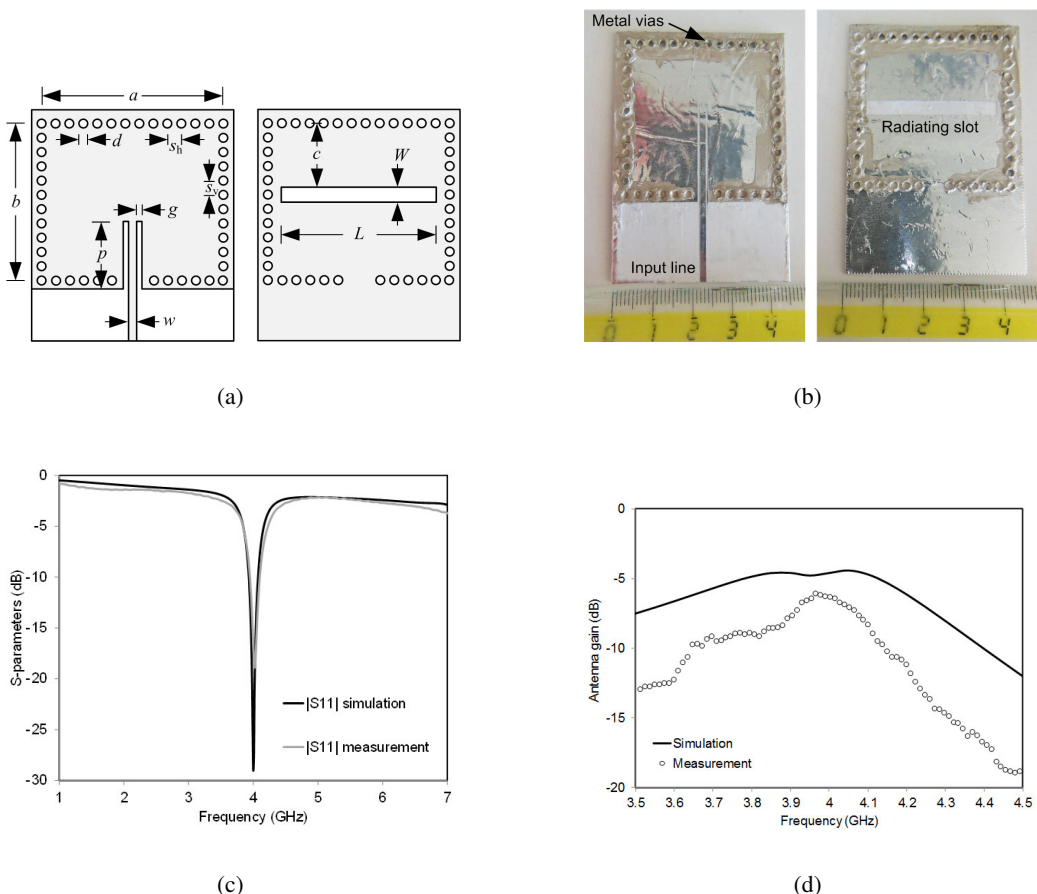


Figure 40: Cavity-backed SIW antenna on paper: (a) drawing of the SIW antenna (dimensions in mm: $a=b=39.3$, $c=17.18$, $d=2$, $sh=3.02$, $sv=3.57$, $w=1.6$, $g=0.5$, $p=25.25$, $L=34$, $W=4$); (b) photographs of the bottom and top side of the prototype; (c) simulated and measured input matching of the SIW antenna; (d) simulated and measured gain vs. frequency of the SIW antenna.

This circuit requires a double-face manufacturing process that implies an uncertainty in the alignment between top and bottom when the substrate is flipped. The photographs of the top and bottom sides of the prototype are shown in Fig. 40b.

The measured and simulated input matching of the antenna are reported in Fig. 40c, and they show a negligible variations in terms of resonant frequency of the antenna, thus fully validating the double-face manufacturing process. Finally, the simulated and measured gain of the antenna are shown in Fig. 40d. The measured gain of the antenna at the frequency of 4 GHz is -6.3 dB, corresponding to a radiation efficiency of 6.4%.

3.12 Antenna system

UNIPV

The microwave front-end of the proposed tag architecture needs two fundamental blocks: a UWB antenna and a diplexer. The first device is required to collect microwave power in very large frequency band and the diplexer is mandatory to separate the path related to the energy harvesting and the one used by data transmission. Both devices can be implemented on paper substrate and manufactured with the technique previously adopted.

The two frequency bands adopted are the 868 MHz and the lower part of the UWB channel. Obviously the first one is a well known standard for RF energy harvesting while the second channel is normally used

for data transmission. Of course, wider is the UWB channel, higher is the data rate. This project is designed to guarantee 1.7 GHz of bandwidth for data link, in particular from 3.1 to 4.8 GHz.

Antenna design and validation

The first device designed and manufactured is the antenna. The requirements of this component are related to the operational bandwidth and the presence of a full ground plane.

The total bandwidth required starts from 868 MHz up to 4.8 GHz, in order to guarantee a good input matching and radiation efficiency both for the energy harvesting and for the UWB data transmission channel. To achieve the desired matching of these two frequency bands it is possible to design a single UWB antenna and adding another longer monopole that resonates at 868 MHz. This design is no longer acceptable when a ground plane is required because every kind of resonant component tends to narrow the operational bandwidth.

These constraints lead to a single arm spiral antenna fed by a single-ended tapered microstrip line. This layout is useful to cover the entire operational bandwidth and guarantees the possibility to add a full ground plane.

A bottom shielded antenna is very useful for wearable uses or where the application demands to place the radiating element on the top of an unpredictable object. In this way, the frequency behavior of the antenna is not disturbed by the environment below it.

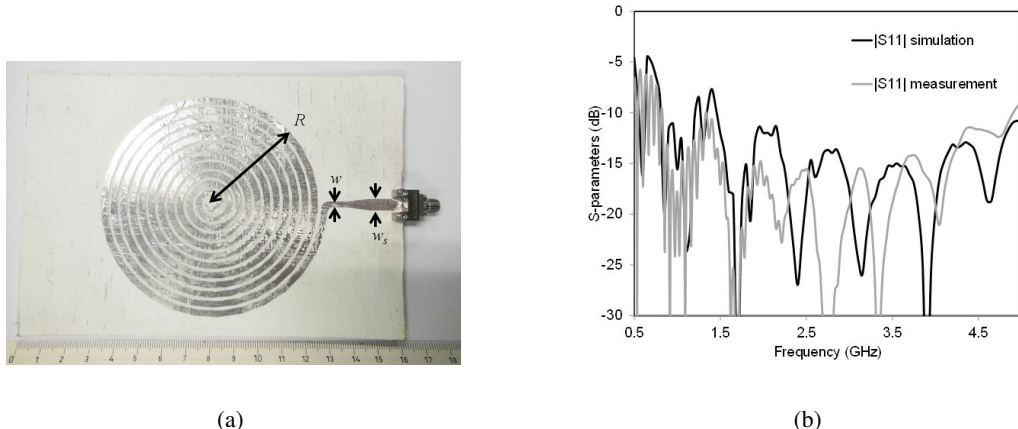


Figure 41: Single arm spiral antenna manufactured on thicker paper substrate. (a) Photograph of the manufactured prototype. Dimensions are in mm: $w_s=5$, $w=2.6$, $R=46$; (b) Simulated and measured $|S_{11}|$ of the single arm spiral antenna.

The microstrip line, that composes the spiral antenna, needs to cover twelve entire rounds in order to achieve the desired input matching also for lower frequency band (868 MHz). The width of the microstrip line and the distance between each round are strictly related to the operational bandwidth.

Because the presence of a fully grounded plane below the antenna element tends to reduce the operational bandwidth and the overall efficiency, it is required to separate as much as possible top and bottom layer. Increasing the thickness of the substrate helps to overcome these problems. Four sheets of Burgo paper are stacked together to achieve the desired thickness, that is 2 mm, and they are glued with the epoxy glue (the same adopted in the manufacturing technique). Finally, the antenna is manufactured on the top of this new substrate and the prototype is shown in Fig. 41a as well as the dimensions. The footprint of the spiral antenna is roughly a square of 97x97 mm.

A 50 Ohm microstrip is adopted to guarantee a good matching between the antenna and the measurement setup. A short taper is then used to match the width of the 50 Ohm microstrip with the arm of the spiral antenna. The measurement setup is slightly different with respect of previous paper-based

components: in this case it is used an end-launch connector instead of the test fixture. By this method the antenna is free from surrounding elements in its near field.

Measurements and simulations are presented in Fig. 41b. It is clear the good agreement between them throughout the frequency band.

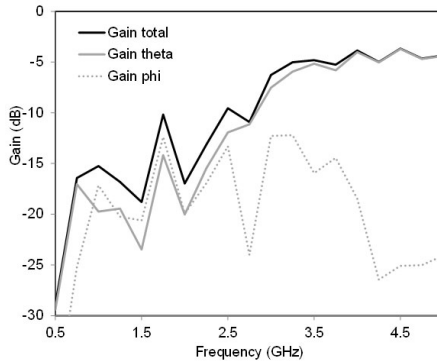


Figure 42: Simulated gain versus frequency of the paper based spiral antenna. The plot shows the superposition of the gain for both and total polarizations.

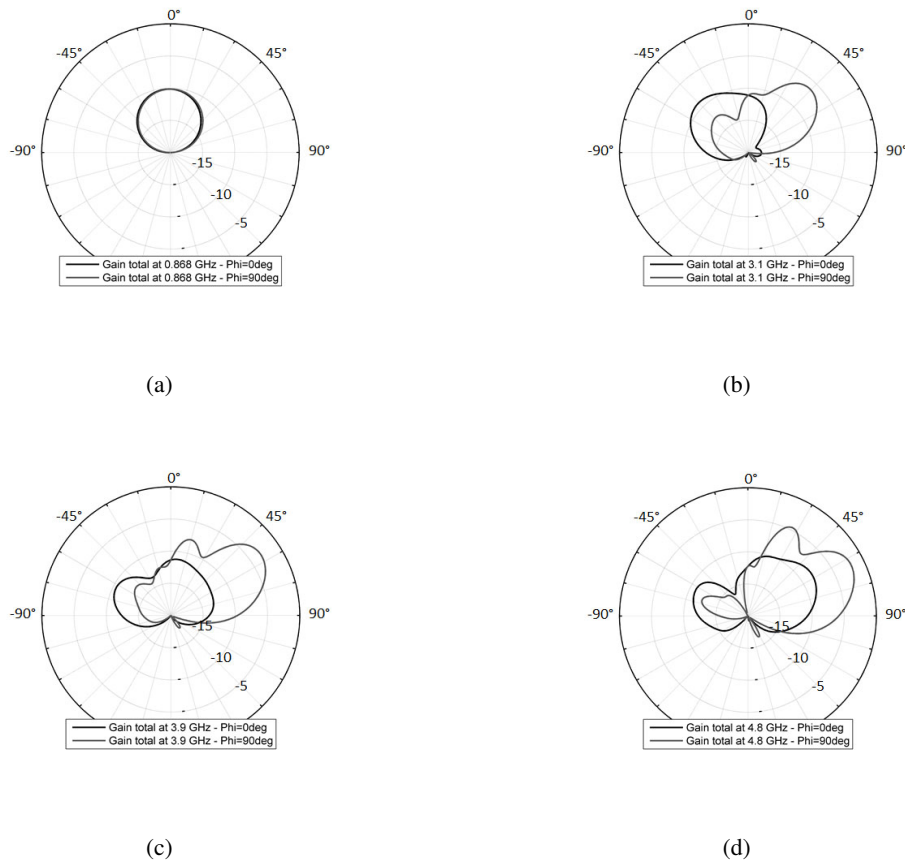


Figure 43: Radiation patterns of the single arm spiral antenna at four main frequencies (a) 0.868 GHz, (b) 3.1 GHz, (c) 3.9 GHz and (d) 4.8 GHz.

The radiation behavior of the spiral antenna has been optimized in order to achieve good performance in both channels (0.868 GHz and 3.1-4.8 GHz). The radiation efficiency across these bands is always bounded between than 7% and 13% despite the high dielectric losses and the presence of a full ground

plane. Fig. 42 shows the gain throughout the frequency span for both polarization in theta and phi directions. It is clear that the antenna behavior for lower frequency (0.868 GHz) is very similar to a monopole and it is linearly polarized. Moreover, in the UWB channel the main polarization is again along theta direction while the cross polarization is always below -10 dB. Another interesting observation is that the radiation efficiency increases for higher frequencies. This phenomenon is probably due to the distance (measured in wavelength) from the antenna to the ground plane that increase when the wavelength diminishes.

In addition, the radiation patterns at different frequencies are shown in Fig. 42. The first chosen frequency is 0.868 GHz that is important for energy harvesting. Fig. 43a shows the radiation pattern at 0.868 GHz and confirms the monopole behavior of the antenna, therefore the maximum gain is achieved at theta=0. The other important frequencies are 3.1 GHz (Fig. 43b), 3.9 GHz (Fig. 43c) and 4.8 GHz (Fig. 43d). These values are chosen to estimate the radiation pattern across the entire UWB channel.

Diplexer

The aim of a diplexer is to combine or separate two channels operating at different frequency bands. It is widely adopted to separate the TX and the RX path channels of a communication link where the two frequency bands occupy two different part of the spectrum. As mentioned, an autonomous tag capable of sensing and monitoring needs a path for the RF energy harvesting, possibly arises from RF showers, and a separate path dedicated to data management.

The diplexer is a three-port device mainly composed by a power divider and two microwave filters: each of them is related to one of the frequency band of interest. The proposed design is composed by a low pass filter and a UWB filter. The aim of the first one is to filter the spectrum below the data transmission frequency band and therefore to collect as much energy as possible, in particular to guarantee the lowest insertion loss as possible at 868 GHz. A low pass filter fits these characteristics together with a simple and very flexible design.

The chosen architecture for the low pass filter consists in a two radial stubs and a narrow microstrip line between them 17.9mm long, the design is shown in Fig. 44a. The radial stubs act as big capacitors that filter the microwave power when the frequency increases. In the meanwhile, the narrow microstrip line is adopted to guarantee a good matching in the pass-band. As predictable, larger are the radial stubs, higher is the value of the related capacitance and therefore the cut-off frequency of the filter is shifted to lower frequencies. The design of this filter is aided firstly by a fast circuit simulator because the entire filter is designed in microstrip technology. Beside this, a final optimization in a full-wave simulator is carried out and the final design is shown in Fig. 44b. The dimensions are stated in the caption of the same figure.

This design is then manufactured and measure. The superposition of the simulated and measured S parameters are reported in Fig. 44c.

On the other hand, the design of a filter that covers the lower part of the UWB channel is not so straightforward. In addition, because selectivity is mandatory to avoid spurious signals the design of this component could be very complex.

The idea to realize this device is to divide the overall filter into two different paths: each of them is composed by a filter that is specific for one sub-band of the full one. In this way, the design of a narrower band filters results more feasible and opens the possibility to compose wide-band filter specifically for UWB applications.

In order to keep the device as symmetric as possible, each filter should be designed in order to guarantee the same relative bandwidth, defined as the ratio between the central frequency of the bandpass and the -3dB bandwidth. The block scheme that describes this architecture is shown in Fig. 45a while the theoretical frequency behavior of this device is depicted in Fig. 45b.

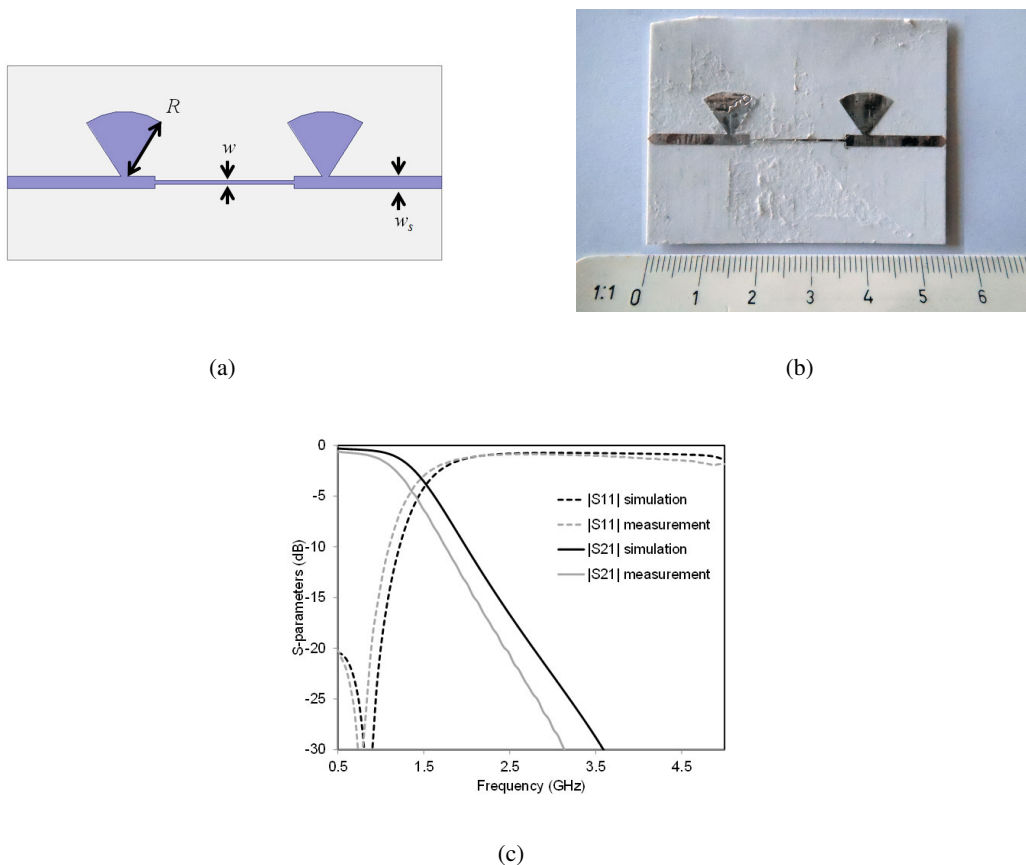


Figure 44: Low pass filter on paper substrate. (a) Drawing of the design. Dimensions are in mm: $w_s=1.6$, $w=0.4$, $R=8.17$; (b) Photograph of the manufactured prototype; (c) Simulated and measured S-parameters of the low-pass filter on paper.

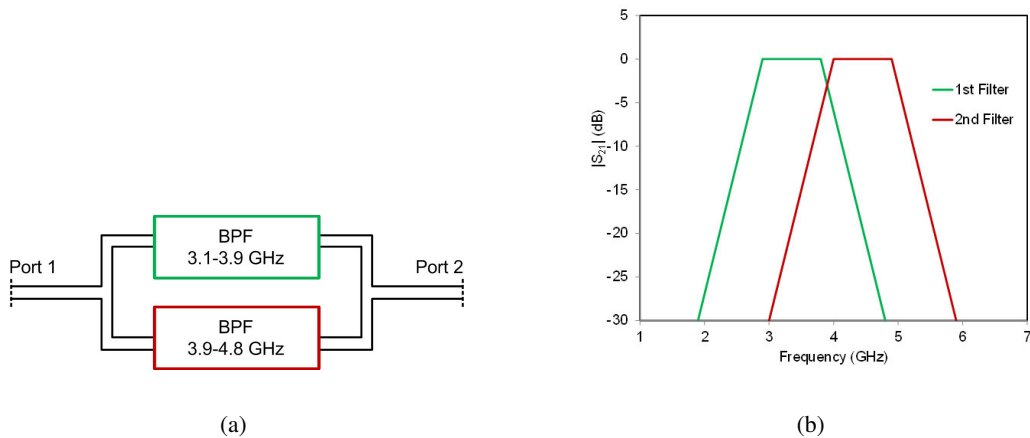


Figure 45: (a) Scheme of the UWB filter of the diplexer. (b) Frequency behavior of the UWB filter.

UNIBO

As tag radiating element, the UNIBO unit has designed the novel UWB-UHF antenna reported in Fig. 46; this particular antenna integrates in the same structure two radiating elements working in two frequency bands: the UWB 3.1 to 4.8 GHz band, which is covered by means of an Archimedean spiral antenna, and

the UHF 868 MHz band, guaranteed by means of a meandered dipole obtained from the extension of the spiral outer arms. The two elements share the same port, for compactness purposes.

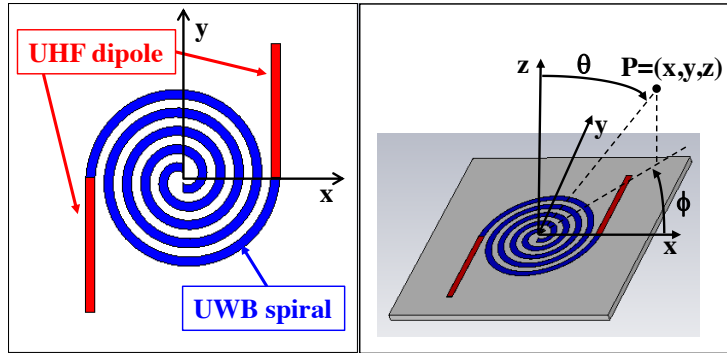


Figure 46: UWB-UHF antenna architecture.

In Fig. 47 the final layout of the prototype is shown, both on paper substrate and on Taconic RF60A used for the diplexer, too. The dipole length is chosen in order to have a resonance behavior at the 868 MHz frequency. This is possible while also preserving little dimensions, as the whole spiral length contribute to the dipole antenna; in particular a 1.5λ behavior has been chosen. Since the current responsible of the radiation in the UHF band has to go through the entire, long path of the metallization, the high paper losses cause an efficiency of 63%, while the realized gain equals the 0 dBi value. An increase of the efficiency to about 80% is reached with the higher quality Taconic substrate. The auto-complementarity and auto-similarity principles of the spiral antenna guarantee an almost constant behavior over the whole 3.1 to 4.8 GHz band, with an efficiency of 90% and a realized gain of 3-4 dBi with both substrates.

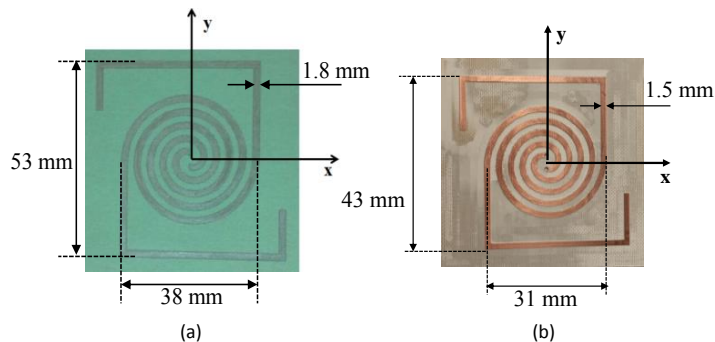


Figure 47: Prototypes layout: (a) on paper substrate; (b) on Taconic RF60A substrate.

In Fig. 48 the antenna impedance simulated and measured results for the paper antenna are reported: From inspection of the figures the exact resonance at 868 MHz, and the almost constant behavior in the UWB band can be easily evinced; the third zero crossing of the reactance in the lower band clearly confirms that the total length of the dipole provides a 1.5λ behavior. It can be observed that in the UHF band the integrated antenna shows an impedance real part of about 12Ω which is acceptable for being matched to an RFID rectifier. Similar results pertain to the Taconic antenna.

In Fig. 49 the predicted and measured normalized radiation patterns in the yz - and xz -plane of the UWB-UHF antenna in both frequency bands are reported. As can be evinced, at 868 MHz the antenna behaves almost identically to a standard straight standalone dipole. The dipole far-field results perfectly linearly-polarized in the y -direction (main axis of the dipole) for a wide elevation (θ) range. In the UWB band, the plots correspond to the co-polarized components, where, due to the ungrounded antenna structure, the $z > 0$ half space shows the right-handed circularly polarized (RHCP) component, while the $z < 0$ one contains the left-handed circularly polarized (LHCP) component.

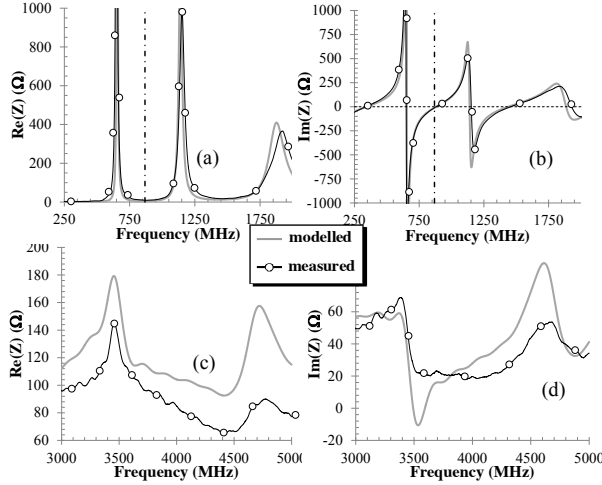


Figure 48: Measured and modelled antenna input impedance: (a) real part, (b) imaginary part in the UHF band; (c) real part, (d) imaginary part in the UWB band.

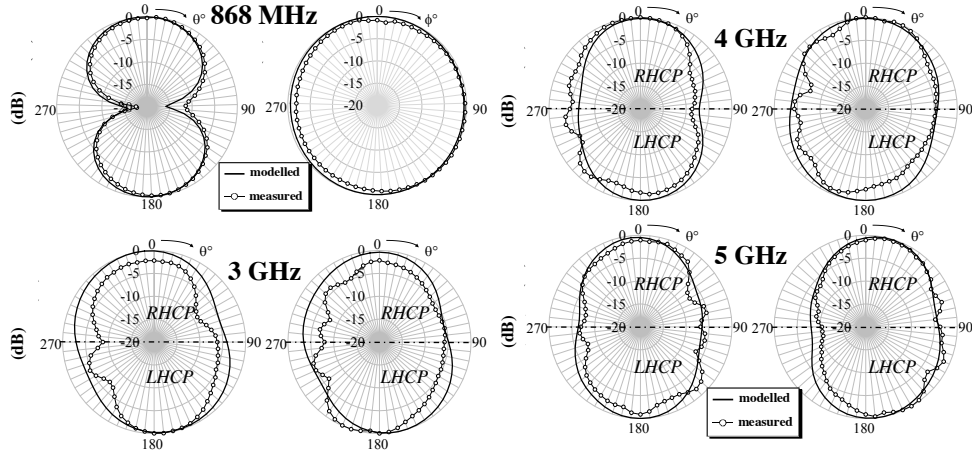


Figure 49: Measured and modelled normalized radiation patterns in the UHF and UWB bands, in the yz-plane (left pattern), and in the xz-plane (right pattern).

A test of the UWB communication antenna capabilities has then been carried out, in order to verify the effect of the back-mounted diplexer on the ungrounded antenna. For this purpose a rigorous circuital approach has been adopted: as UWB pulse waveform a fourth derivative of a Gaussian pulse with duration of 300 ps and period $T_p = 6$ ns is chosen. This way the UWB spectrum can be described by a fundamental frequency $f_{UWB} = 1/T_p = 166.67$ MHz, with NH = 64 harmonics for the coverage of the UWB spectrum. Let us consider the antenna in receiving mode. By resorting to EM theory [1] a rigorous evaluation of the pulse distortion at the antenna port can be carried out. In the following we imagine an incident UWB plane wave with a linearly polarized electric field

$$\mathbf{E}_i = E_i (\cos \psi \hat{\theta} + \sin \psi \hat{\phi}), \quad (6)$$

In these conditions the equivalent Norton current generators are obtained by combining the UWB incident field with the electric field the antenna would radiate at a distance r and direction (θ, ϕ) , in transmitting mode. The corresponding situation is depicted in Fig. 50: 64 current generators are placed in parallel to the full-wave description of the antenna admittance in the whole bandwidth (by means of the admittance $Y_A(\omega)$) in order to compute the actual received UWB voltage at the UWB RX port: this

port is simply given by the balanced antenna terminals in the case without diplexer, while in the second case it corresponds to the port 3 of Fig. 12.

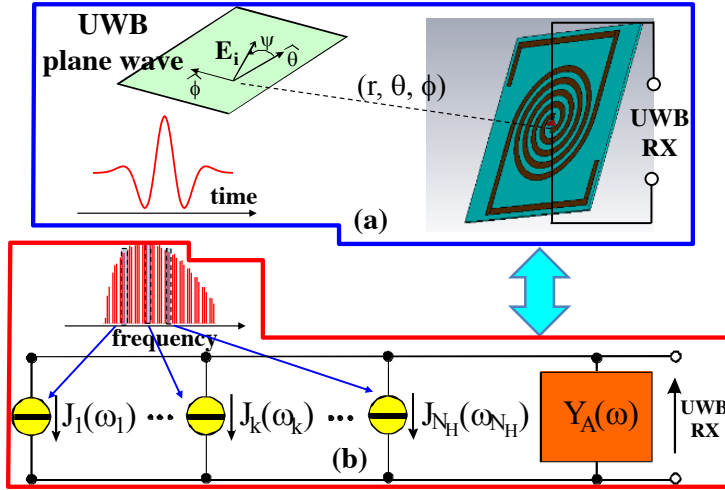


Figure 50: (a) Antenna in receiving mode; (b) Corresponding equivalent-circuit representation.

The distortion effects of the antenna (with and without the diplexer) during the reception of a couple of pulses (of opposite polarity) are compared for different incoming directions ($(\theta, \phi) = (0^\circ, 0^\circ); (30^\circ, 0^\circ)$), different field polarizations ($\psi = 0^\circ, 90^\circ$), and at a fixed distance $r = 1$ m. Fig. 51 reports the received waveforms corresponding to a transmitted pulse of negative polarity in two link conditions. Similar results pertain to the positive pulse case. Note the opposite polarity of the received voltages for the two antenna topologies: this phenomenon is commonly solved in practical UWB communication by means of a first reference pulse of known polarity for each transmitted bit. Despite the augmented ringing of the signal in presence of the circuitry behind the antenna, the behavior of the system is acceptable in this case, too. The backside area occupied by the diplexer does not weaken the UWB system activity, as also confirmed by the energy level at the UWB RX port, defined as the difference between the two received pulses areas over the pulse duration: very similar energy levels are obtained in the cases of Fig. 51.

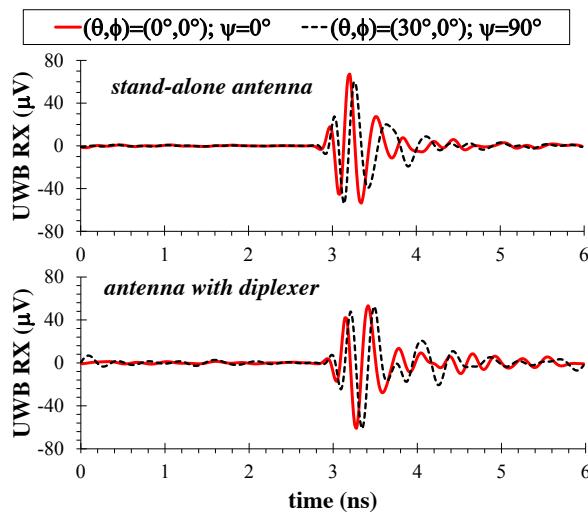


Figure 51: Received pulse waveforms in different link conditions.

3.13 Localization and tracking algorithm

The localization and tracking process typically consists of two phases: (i) a **measurement phase**, where readers measure their range to the tag; and (ii) a **location inference phase**, where tags positions are inferred from prior knowledge and measurements. The performance of a localization system jointly depends on these two phases. The Deliverable GRETA D2 introduced the location inference phase by describing the Bayesian filtering techniques for localization, tracking, and ordering of tags. In this Deliverable, attention is given to the measurement phase.

The measurement phase has a crucial impact on the tag localization accuracy. In the application scenarios of GRETA the requirement on localization accuracy is stringent and the link budget for the backscattered signal is poor. Ranging techniques based on time-of-arrival (TOA) are adopted to exploit the properties of UWB signals. In particular, range information is extracted in terms of range estimate at each reader from the received signals. In this Section, we present a tractable model for the range information as a function of wireless environment, signal features, and detection techniques [2]. Based on the proposed model, practical hard-decision algorithms are developed. Classical ranging techniques based on energy detection provide hard-decision range estimates in accordance with the TOA of received signals. Here, a mathematical model is derived to describe the range information accounting for the wireless environment and signal features to facilitate the design and analysis of optimal energy detectors (EDs). The benefits to location awareness provided by the proposed range information model are quantified in wireless environments.

Consider a ranging system composed of a transmitter at position \mathbf{p}_t that emits N_p copies of a signal $s(t)$ with repetition period T_p , and a receiver at position \mathbf{p}_r . The aim of the ranging system is to detect the signal $s(t)$ and to estimate its TOA τ with respect to a reference time t_0 from the received signal based on N_p observations each with duration T_{obs} . For ranging techniques based on energy detection, an energy sample (namely energy bin) is collected every dwell time T_d . The detection of the signal $s(t)$ and the estimation of its TOA τ are based on the vector of energy bins \mathbf{b} , with $|\mathbf{b}| = N_b$. Classical approaches follow the Bayesian hypothesis testing, involving the comparison of the energy bins with a threshold. Such a threshold is often chosen to achieve a constant false-alarm rate, resulting in a certain misdetection rate.

Typically, ranging is based on hard-decision algorithms which provide the TOA estimate from the observed energy bins. Each element b_i of the vector \mathbf{b} is an instantiation of the random variable (RV)

$$B_i = \sum_{s=0}^{N_{\text{sb}}-1} X_{N_p}^{(i,s)} \quad (7)$$

where

$$X_n^{(i,s)} = \frac{1}{n} \sum_{p=0}^{n-1} (U_{i,p,s} + N_{i,p,s})^2 \quad (8)$$

is the sample average, in p , of the energy bins. In particular, components $U_{i,p,s}$ and $N_{i,p,s}$ are independent random samples of the received signal and of the thermal noise, respectively at the sampling instant $t_{i,p,s} = i T_d + p T_p + s T_s$, with $i = 0, 1, \dots, N_b - 1$ and $p = 0, 1, \dots, N_p - 1$, with sampling period T_s . Note that B_i depends on transmitted signal, thermal noise, true TOA τ , wireless channel, and ED parameters. Let $\boldsymbol{\theta} = [\tau \boldsymbol{\theta}_h \boldsymbol{\theta}_d]$ where $\boldsymbol{\theta}_h$ and $\boldsymbol{\theta}_d$ are the vectors of parameters representing the wireless channel and the ED, respectively. The normalized bin $B_i N_p / \sigma^2$ conditioned on $\boldsymbol{\theta}$ is distributed as a noncentral chi-squared RV with $N_p N_{\text{sb}}$ degrees of freedom, i.e.,

$$B_i \frac{N_p}{\sigma^2} \stackrel{|\boldsymbol{\theta}}{\sim} \chi_{N_p N_{\text{sb}}}^2(\lambda_i) \quad (9)$$

where λ_i is the noncentrality parameter, which depends on $\boldsymbol{\theta}$, given by

$$\lambda_i = \sum_{p=0}^{N_p-1} \sum_{s=0}^{N_{\text{sb}}-1} \frac{U_{i,p,s}^2}{\sigma^2} \quad (10)$$

$$f_{\mathbf{l}}(i|\boldsymbol{\theta}) = \left[1 - F_{\mathbf{B}_i}(\xi_i|\boldsymbol{\theta})\right] \prod_{j \in \mathcal{J}_i(i)} F_{\mathbf{B}_j}(\xi_j|\boldsymbol{\theta}) \left[1 - \prod_{n \in \mathcal{B}} F_{\mathbf{B}_n}(\xi_n|\boldsymbol{\theta})\right]^{-1} \quad (11)$$

$$\begin{aligned} f_{\mathbf{l}}(i|\boldsymbol{\theta}) &= \left[\int_0^{+\infty} \prod_{j \in \mathcal{B} \setminus \{i\}} F_{\mathbf{B}_j}(b|\boldsymbol{\theta}) f_{\mathbf{B}_i}(b|\boldsymbol{\theta}) db - \int_0^{\xi_i} \prod_{j \in \mathcal{B} \setminus \{i\}} F_{\mathbf{B}_j}(\xi_j(b)|\boldsymbol{\theta}) f_{\mathbf{B}_i}(b|\boldsymbol{\theta}) db \right] \\ &\quad \times \left[1 - \prod_{n \in \mathcal{B}} F_{\mathbf{B}_n}(\xi_n|\boldsymbol{\theta})\right]^{-1} \end{aligned} \quad (12)$$

$$\begin{aligned} f_{\mathbf{l}}(i|\boldsymbol{\theta}) &= \left[\int_0^{+\infty} \prod_{j \in \mathcal{J}_{N_w}(i)} F_{\mathbf{B}_j}(\xi_j(b)|\boldsymbol{\theta}) \prod_{j \in \mathcal{J}_{N_w}^c(i) \setminus \{i\}} F_{\mathbf{B}_j}(b|\boldsymbol{\theta}) f_{\mathbf{B}_i}(b|\boldsymbol{\theta}) db \right. \\ &\quad \left. - \int_0^{\xi_i} \prod_{j \in \mathcal{B} \setminus \{i\}} F_{\mathbf{B}_j}(\xi_j(b)|\boldsymbol{\theta}) f_{\mathbf{B}_i}(b|\boldsymbol{\theta}) db \right. \\ &\quad \left. + \sum_{m \in \mathcal{J}_{N_w}(i+N_w+1)} \int_{\xi_j \in \mathcal{J}_{i-m+N_w}(i)}^{+\infty} \prod_{j \in \mathcal{J}_{i-m+N_w}(i)} F_{\mathbf{B}_j}(\xi_j(b)|\boldsymbol{\theta}) [F_{\mathbf{B}_i}(b|\boldsymbol{\theta}) - F_{\mathbf{B}_i}(\xi_i|\boldsymbol{\theta})] \right. \\ &\quad \left. \times \prod_{j \in \mathcal{J}_{i-m+N_w}^c(i) \setminus \{i,m\}} F_{\mathbf{B}_j}(b|\boldsymbol{\theta}) f_{\mathbf{B}_m}(b|\boldsymbol{\theta}) db \right] \left[1 - \prod_{n \in \mathcal{B}} F_{\mathbf{B}_n}(\xi_n|\boldsymbol{\theta})\right]^{-1} \end{aligned} \quad (13)$$

$$\begin{aligned} f_{\mathbf{l}}(i|\boldsymbol{\theta}) &= \left[\int_0^{+\infty} \check{F}_{\mathbf{B}_{i-1}}(\xi_{i-1}(b)|\boldsymbol{\theta}) \prod_{j \in \mathcal{B} \setminus \{i-1,i\}} F_{\mathbf{B}_j}(b|\boldsymbol{\theta}) f_{\mathbf{B}_i}(b|\boldsymbol{\theta}) db \right. \\ &\quad \left. - \int_0^{\xi_i} \prod_{j \in \mathcal{B} \setminus \{i\}} F_{\mathbf{B}_j}(\xi_j(b)|\boldsymbol{\theta}) f_{\mathbf{B}_i}(b|\boldsymbol{\theta}) db \right. \\ &\quad \left. + \sum_{m \in \mathcal{J}_{N_b-i-1}(N_b)} \int_{\xi_{m,i}}^{+\infty} \check{F}_{\mathbf{B}_{i-1}}(\xi_{i-1}(b)|\boldsymbol{\theta}) \prod_{j \in \mathcal{J}_{m-i}(m)} [F_{\mathbf{B}_j}(b|\boldsymbol{\theta}) - F_{\mathbf{B}_j}(\xi_j|\boldsymbol{\theta})] \right. \\ &\quad \left. \times \prod_{j \in \mathcal{J}_{m-i}^c(m) \setminus \{i-1,m\}} F_{\mathbf{B}_j}(b|\boldsymbol{\theta}) f_{\mathbf{B}_m}(b|\boldsymbol{\theta}) db \right] \left[1 - \prod_{n \in \mathcal{B}} F_{\mathbf{B}_n}(\xi_n|\boldsymbol{\theta})\right]^{-1} \end{aligned} \quad (14)$$

with $u_{i,p,s}$ denoting the instantiation of $\mathbf{U}_{i,p,s}$ and σ^2 denoting the variance of the zero-mean thermal noise. The cumulative density function (CDF) $F_{\mathbf{B}_i}(b|\boldsymbol{\theta})$ and probability density function (pdf) $f_{\mathbf{B}_i}(b|\boldsymbol{\theta})$ of \mathbf{B}_i conditioned on $\boldsymbol{\theta}$ are given in [2]. In practice, the noise variance can be estimated by observing the energy bins in an absence of the transmitted signal. Also, λ_i depends on the wireless channel instantiation. Therefore, to derive the distribution of the range estimation error, the averaging over all possible wireless channel instantiations is required.

3.13.1 Range Information Model

In this section, we propose a model for the range information in terms of range estimate and range error.

3.13.1.1 Range Estimate

A widely used approach for ranging is based on hard-decision algorithms that aim to determine the index \hat{i} of the first bin containing a portion of the transmitted signal energy. Therefore, the index \hat{i} can be thought as the instantiation of a discrete RV \mathbf{l} taking value in the set $\mathcal{B} = \{0, 1, \dots, N_b - 1\}$. The TOA estimate $\hat{\tau}$ is the instantiation of the RV \mathbf{T} , with pdf $f_{\mathbf{T}}(t|\boldsymbol{\theta})$, which depends on \mathbf{l} since $\hat{\tau}$ is chosen from the interval $[\hat{i}T_d, (\hat{i}+1)T_d]$. Consider a bijective function $\hat{\tau} = g(\hat{i})$ (e.g., the TOA estimate is chosen to be the center of the interval as $g(\hat{i}) = \hat{i}T_d + T_d/2$). Therefore, the pdf $f_{\mathbf{T}}(t|\boldsymbol{\theta})$ of the TOA estimate is determined from $f_{\mathbf{l}}(i|\boldsymbol{\theta})$ and depends on $\boldsymbol{\theta}$ since \mathbf{l} is a function of both the wireless channel and the ED.

Various hard-decision algorithms based on ED have been proposed in the literature. Here, the most popular ones are analyzed: threshold crossing search (TCS), maximum bin search (MBS), jump back and search forward (JBSF), and serial backward search (SBS) algorithms. These algorithms involve the comparison of each bin value with a corresponding threshold. Let the threshold crossing event be $\mathcal{C}_{\text{th}} = \{\exists i \in \mathcal{B} : B_i > \xi_i\}$ where ξ_i is the threshold for the bin B_i with $i \in \mathcal{B}$. The probability mass function (pmf) of the selected bin index \mathbf{l} conditioned on \mathcal{C}_{th} and $\boldsymbol{\theta}$ can be written as [2]

$$f_{\mathbf{l}}(i|\boldsymbol{\theta}) = \mathbb{P}\{\mathcal{S}_i \cap \mathcal{C}_{\text{th}}|\boldsymbol{\theta}\} / \mathbb{P}\{\mathcal{C}_{\text{th}}|\boldsymbol{\theta}\} \quad (15)$$

where the event $\mathcal{S}_i \cap \mathcal{C}_{\text{th}}|\boldsymbol{\theta} = \{i \text{ is selected}, \mathcal{C}_{\text{th}}|\boldsymbol{\theta}\}$ and

$$\mathbb{P}\{\mathcal{C}_{\text{th}}|\boldsymbol{\theta}\} = 1 - \prod_{n \in \mathcal{B}} F_{B_n}(\xi_n|\boldsymbol{\theta}). \quad (16)$$

For brevity, $f_{\mathbf{l}}(i|\boldsymbol{\theta})$ will be used to denote $f_{\mathbf{l}}(i|\mathcal{C}_{\text{th}}, \boldsymbol{\theta})$. In general, a different threshold ξ_i can be used for each bin index i when it is important to account for the variation among the energy samples.

The TCS algorithm first searches for each bin value b_i that crosses a threshold ξ_i for all $i \in \mathcal{B}$. The algorithm then selects, if \mathcal{C}_{th} occurs, the bin index \hat{i} as the smallest bin index i for which $b_i > \xi_i$. This leads to (11). The choice of the thresholds ξ_i 's affects the accuracy of the TOA estimation, as well as the detection rate and the false-alarm rate.

The MBS algorithm first searches for the maximum value among all the bins with index $i \in \mathcal{B}$. The algorithm then selects, if \mathcal{C}_{th} occurs, if at least a bin with index in \mathcal{B} crosses its threshold, the bin index \hat{i} as the i for which $b_j \leq b_i$ for all $j \neq i$. This leads to (12), with $\check{\xi}_j(b) = \min\{\xi_j, b\}$.

The JBSF algorithm first identifies the index m corresponding to the maximum bin value, jumps back to the bin with smallest index in $\mathcal{I}_{N_w}(m)$, and searches forward for each bin value b_i that crosses a threshold ξ_i for all $i \in \mathcal{I}_{N_w}(m)$, where $\mathcal{I}_W(m) = \mathcal{B} \cap \{m - W + 1, m - W + 2, \dots, m\}$ and with window length N_w . For example, the window length N_w can be chosen according to the channel delay spread and the transmitted signal. The algorithm then selects, if \mathcal{C}_{th} occurs, the bin index \hat{i} as the smallest i for which $b_i > \xi_i$ with $i \neq m$ or as m if none of them crosses the threshold. This leads to (13). Note that JBSF with $N_w = 0$ corresponds to MBS and (13) degenerates to (12). The SBS algorithm first identifies the index m corresponding to the maximum bin value, and searches backward for each bin value b_i that crosses a threshold ξ_i for all $i \in \mathcal{I}_m(m)$. The algorithm then selects, if \mathcal{C}_{th} occurs, the bin index \hat{i} as the the smallest i for which $b_j > \xi_j$ for all $j \in \mathcal{I}_{m-i}(m)$ or as m if none of them crosses the threshold. This leads to (14), with

$$\check{F}_{B_k}(\cdot|\boldsymbol{\theta}) = \begin{cases} F_{B_k}(\cdot|\boldsymbol{\theta}) & \text{for } k \in \mathcal{B} \\ 1 & \text{for } k \notin \mathcal{B} \end{cases}$$

and $\check{\xi}_{m,i} = \max\{\xi_j \forall j \in \mathcal{I}_{m-i}(m)\}$. Recall that $f_{\mathbf{l}}(i|\boldsymbol{\theta})$ for the hard-decision algorithms derived above is conditioned on the threshold crossing event \mathcal{C}_{th} and $\boldsymbol{\theta}$. Expressions for the joint pmf of \mathbf{l} and \mathcal{C}_{th} conditioned on $\boldsymbol{\theta}$ can be obtained by $\check{f}_{\mathbf{l}}(i|\boldsymbol{\theta}) = f_{\mathbf{l}}(i|\boldsymbol{\theta}) [1 - \prod_{n \in \mathcal{B}} F_{B_n}(\xi_n|\boldsymbol{\theta})]$. The distribution $f_{\mathbf{l}}(i|\boldsymbol{\theta})$ of the selected bin index for numerous other hard-decision algorithms can be derived following a similar approach.

3.13.1.2 Range Error

The distribution of the TOA estimation error depends on the particular hard-decision algorithm. In particular, the TOA estimation error $e(\tau) = \hat{\tau} - \tau$ is an instantiation of the RV $E = \mathsf{T} - \tau$, and thus

$$f_E(e|\boldsymbol{\theta}) = f_{\mathsf{T}}(e + \tau|\boldsymbol{\theta}). \quad (17)$$

For a given τ , the RV E belongs to a finite set $\mathcal{E}_\tau = \{\mathsf{T} - \tau \text{ s.t. } \mathsf{T} \in g(\mathcal{B})\}$ where $g(\mathcal{B})$ represents a finite set of TOA estimate. In an absence of a prior information on the true TOA, τ can be modeled as a

uniform RV over the interval $[0, T_a]$, where T_a is the maximum possible TOA that depends on the wireless environment (in general, $0 < T_a \leq T_{\text{obs}}$), which results in $\mathcal{E}_\tau = [-T_a, T_{\text{obs}}]$. When the wireless environment is not known, T_a can be chosen as $T_a = T_{\text{obs}}$. Therefore,

$$f_E(e|\boldsymbol{\theta}_d) = \frac{1}{T_a} \int_0^{T_a} f_E(e|\boldsymbol{\theta}_d, \tau) d\tau \quad (18)$$

where

$$f_E(e|\boldsymbol{\theta}_d, \tau) = \begin{cases} \left| \frac{dg^{-1}(e+\tau)}{de} \right| f_I(g^{-1}(e+\tau)|\boldsymbol{\theta}_d, \tau) & \text{for } e \in \mathcal{E}_\tau \\ 0 & \text{otherwise} \end{cases} \quad (19)$$

with $f_I(i|\boldsymbol{\theta}_d, \tau) = \mathbb{E}_{\boldsymbol{\theta}_h}\{f_I(i|\boldsymbol{\theta})\}$. For specific hard-decision algorithms, (19) can be evaluated by substituting the pdf and CDF of B_i into the specific conditional pmf $f_I(i|\boldsymbol{\theta})$ derived in Section 3.13.1.1 and taking the expectation over the vector of noncentrality parameters $\boldsymbol{\lambda} = [\lambda_0, \lambda_1, \dots, \lambda_{N_b-1}]$. This requires both the evaluation of cumbersome expressions and the expectation over all the channel parameters, calling for a tractable range information model.

3.13.2 Tractable Range Information Model

The design of ranging techniques demands tractable expressions for the range information model, which can be obtained by simplifying $f_{B_j}(b|\boldsymbol{\theta})$ and $F_{B_j}(b|\boldsymbol{\theta})$. First, recall that the chi-squared RV converges in distribution to a Gaussian RV as the number of degrees of freedom, here given by $N_p N_{\text{sb}}$, increases. Therefore $B_i N_p / \sigma^2$ in (9) converges in distribution as

$$B_i \frac{N_p}{\sigma^2} \xrightarrow{d} \tilde{B}_i \frac{N_p}{\sigma^2} \stackrel{|\boldsymbol{\theta}}{\sim} \mathcal{N}(N_p N_{\text{sb}} + \lambda_i, 2(N_p N_{\text{sb}} + 2\lambda_i)). \quad (20)$$

The above approximation depends on $N_p N_{\text{sb}}$ and is accurate for $N_p \gg 1$ or $T_d \gg T_s$. Note that the above distributions depend on the instantiation of the wireless channel through $\boldsymbol{\theta}_h$ in $\boldsymbol{\theta}$. However, the knowledge of the exact channel instantiation is typically not available.

The range information model is further simplified by considering distributions that depend on channel statistics rather than channel instantiations, i.e., on $\bar{\boldsymbol{\theta}} = [\tau \bar{\boldsymbol{\theta}}_h \boldsymbol{\theta}_d]$ instead of $\boldsymbol{\theta}$, where $\bar{\boldsymbol{\theta}}_h$ represents the vector of channel statistics. Recall that the sample average $X_n^{(i,s)}$ in (8) depends on $[\tau \boldsymbol{\theta}_h \boldsymbol{\theta}_d]$ through $U_{i,p,s}$ and on $\boldsymbol{\theta}_d$ through $N_{i,p,s}$. Therefore we approximate $X_n^{(i,s)}$ as in [2] by replacing $U_{i,p,s}$ with a deterministic quantity $U_{i,s}$ that depends on $\bar{\boldsymbol{\theta}}$. Thus, the dependence on wireless channel instantiations can be removed by substituting each noncentrality parameter λ_i , which depends on $\boldsymbol{\theta}$, with its expected value $\bar{\lambda}_i$, which depends on $\bar{\boldsymbol{\theta}}$, in all of the above distributions.

The impulse response of a wideband wireless channel at time t is commonly described by $h(t; \boldsymbol{\zeta}) = \sum_{l=1}^{L(t)} \alpha_l(t) \delta(\zeta - \tau_l(t))$ where $L(t)$ is the number of multipath components, and $\alpha_l(t)$ and $\tau_l(t)$ are the amplitude gain and the arrival time of the l th path, respectively. The $L(t)$, $\alpha_l(t)$, and $\tau_l(t)$ are considered time-invariant over an observation time. For a resolvable multipath channel, i.e., the path interarrival time intrinsic to the wireless environment is larger than the temporal duration of the transmitted signal, $\mathbb{E}\{U_{i,p,s}^2\}$ can be written as $\mathbb{E}\{U_{i,p,s}^2\} \simeq \mathbb{E}\left\{\sum_{l=1}^L \alpha_l^2 s^2(t_{i,p,s} - \tau_l)\right\}$. Therefore, the calculation of $\bar{\lambda}_i$ requires the averaging with respect to the channel nuisance parameters α_l 's and τ_l 's in $\boldsymbol{\theta}_h$. The complexity of such calculation depends on the joint distribution of L , α_l 's, and τ_l 's. However, the resolution of the ED is limited by the dwell time T_d . Hence, the statistics of the energy bins can be determined by considering a tapped-delay-line model. In particular, $h(t; \boldsymbol{\zeta})$ can be replaced by $\check{h}(t; \boldsymbol{\zeta}) = \sum_{l=1}^{\check{L}} \check{\alpha}_l \delta(\zeta - \check{\tau}_l)$, where \check{L} is a deterministic number of path, $\check{\tau}_l = \tau + l\Delta$ with Δ deterministic, and $\check{L}\Delta$ is the approximate dispersion of the channel. For example, Δ can be chosen as the average interarrival time of the paths $\check{\tau}_l$. This results in

$$\mathbb{E}\{U_{i,p,s}^2\} \simeq \sum_{l=1}^{\check{L}} \mathbb{E}\{\check{\alpha}_l^2\} s^2(t_{i,p,s} - \check{\tau}_l). \quad (21)$$

By using this approach, the expected value of the noncentrality parameter for the i th bin becomes

$$\bar{\lambda}_i = \sum_{p=0}^{N_p-1} \sum_{s=0}^{N_{sb}-1} \sum_{l=1}^{\check{L}} \frac{\mathbb{E}\{\check{\alpha}_l^2\}}{\sigma^2} s^2(t_{i,p,s} - \check{\tau}_l). \quad (22)$$

Using (22) instead of λ_i in all distributions reported above, one can obtain the tractable range information model that depends only on $\bar{\boldsymbol{\theta}}$ instead of $\boldsymbol{\theta}$. For instance, B_i can be approximated by \bar{B}_i with conditional CDF given by

$$F_{\bar{B}_i}(b|\bar{\boldsymbol{\theta}}) = \Phi\left(\frac{bN_p/\sigma^2 - N_pN_{sb} - \bar{\lambda}_i}{\sqrt{2(N_pN_{sb} + 2\bar{\lambda}_i)}}\right) \quad (23)$$

where λ_i is replaced by $\bar{\lambda}_i$ and approximating a chi-squared RV with a Gaussian RV and $\Phi(\cdot)$ is the normal Gaussian CDF.

Using the results in this section, tractable expressions of the distribution of the TOA estimation error can be derived for hard-decision algorithms, as introduced in [2]. In particular, substituting the pdf and CDF of B_i into the conditional pmf $f_1(i|\boldsymbol{\theta})$ in Section 3.13.1.1 for specific hard-decision algorithms, and replacing each λ_i with $\bar{\lambda}_i$, (19) is simplified into a tractable form. The parameters $\bar{\lambda}_i$'s depend on $\bar{\boldsymbol{\theta}}_h$ through \check{L} , the statistics of $\check{\alpha}_l$, and Δ . The $\bar{\lambda}_i$'s depend on $\boldsymbol{\theta}_d$ through N_{sb} and $t_{i,p,s}$, which further depends on T_d , T_p , and T_s .

3.13.3 Design of the Energy Detector

This section aims to present the design of energy detection algorithms based on the proposed range information model. Such a model enables us to determine ED parameters (e.g., the choice of the thresholds, window length, and dwell time) according to different optimization criteria and constraints.

The design of ED commonly involves the probability of detection and that of false-alarm [3]. The detection event occurs when, in a presence of the transmitted signal, the presence of the signal is correctly detected. The probability of such an event is given by

$$P_d(\boldsymbol{\theta}_d) = \sum_{i \in \mathcal{B}} \check{f}_1(i|\boldsymbol{\theta}_d, \boldsymbol{\lambda} \neq \mathbf{0}), \quad (24)$$

where $\mathbf{0}$ is the all-zero vector. The false-alarm event occurs when, in an absence of the transmitted signal, the presence of the signal is incorrectly detected due to noise. The probability of such an event is given by

$$P_{fa}(\boldsymbol{\theta}_d) = \sum_{i \in \mathcal{B}} \check{f}_1(i|\boldsymbol{\theta}_d, \boldsymbol{\lambda} = \mathbf{0}). \quad (25)$$

For a given minimum tolerable level of detection probability P_d^* or maximum tolerable level of false-alarm probability P_{fa}^* , constraints on parameters value $\boldsymbol{\theta}_d$ can be obtained. For example, $P_{fa}(\boldsymbol{\theta}_d)$ is non-increasing with the threshold ξ and therefore a minimum value ξ_{fa} can be determined for a given P_{fa}^* .

An important metric for ED design is the mean squared error (MSE) of the TOA estimate. When conditioned on the detection of the transmitted signal, the MSE of the TOA estimate is given by

$$\rho_t(\boldsymbol{\theta}_d) = \int_{-\infty}^{+\infty} e^2 f_E(e|\boldsymbol{\theta}_d) de. \quad (26)$$

Recalling that the TOA estimation error belongs to a finite set \mathcal{E}_τ , the MSE of the TOA estimate for hard-decision algorithms can be written as

$$\rho_t(\boldsymbol{\theta}_d) = \frac{1}{T_{obs}} \sum_{i=0}^{N_b-1} \int_0^{T_{obs}} (g(i) - \tau)^2 f_1(i|\boldsymbol{\theta}_d, \tau) d\tau. \quad (27)$$

The design of an ED minimizing the MSE of the TOA estimate with a guaranteed minimum level of detection probability can be obtained by solving a constrained optimization problem as

$$\hat{\boldsymbol{\theta}}_d = \underset{\{\boldsymbol{\theta}_d : P_d(\boldsymbol{\theta}_d) \geq P_d^*\}}{\operatorname{argmin}} \rho_t(\boldsymbol{\theta}_d). \quad (28)$$

Instead of guaranteeing a minimum detection probability, the design of an ED can minimize the MSE of the TOA estimate with a guaranteed maximum level of false-alarm probability as

$$\hat{\boldsymbol{\theta}}_d = \underset{\{\boldsymbol{\theta}_d : P_{fa}(\boldsymbol{\theta}_d) \leq P_{fa}^*\}}{\operatorname{argmin}} \rho_t(\boldsymbol{\theta}_d). \quad (29)$$

The design of an ED can also be formulated to maximize the detection probability $P_d(\boldsymbol{\theta}_d)$ for a given maximum tolerable MSE ρ_t^* of the TOA estimate, resulting in

$$\hat{\boldsymbol{\theta}}_d = \underset{\{\boldsymbol{\theta}_d : \rho_t(\boldsymbol{\theta}_d) \leq \rho_t^*\}}{\operatorname{argmax}} P_d(\boldsymbol{\theta}_d). \quad (30)$$

Alternatively, the ED design can be based on a hybrid objective function where the optimization problem is formulated to minimize a metric involving the MSE of the TOA estimate and a penalty. The mathematical formulation of such an optimization problem results in

$$\hat{\boldsymbol{\theta}}_d = \underset{\boldsymbol{\theta}_d}{\operatorname{argmin}} v_t(\boldsymbol{\theta}_d) \quad (31)$$

where

$$v_t(\boldsymbol{\theta}_d) = \rho_t(\boldsymbol{\theta}_d) P_d(\boldsymbol{\theta}_d) + v(\boldsymbol{\theta}_d) [1 - P_d(\boldsymbol{\theta}_d)] \quad (32)$$

is the unconditional MSE of the TOA estimate and $v(\boldsymbol{\theta}_d)$ is a penalty in an absence of detection (the penalty $v(\boldsymbol{\theta}_d)$ can be chosen as a function of the detection probability).

The above optimization problems are typical examples for the design of a ranging system. However, the proposed range information model is general and can be used to formulate other optimization problems that arise from energy detection applications.

3.13.4 Results

This section describes the case study scenario and presents performance results based on the developed theory and sample-level simulations. To validate the range information model, the performance results for ranging and localization are obtained by considering a one-way channel (i.e., for the direct reader-tag link), and will be extended to the two-way case (i.e., backscattering reader-tag-reader link) when the experimental results will be available.

Performance of the proposed range information model is evaluated in terms of the ranging accuracy and localization accuracy. The ranging accuracy is determined in terms of CDF of the TOA estimation error $F_E(e|\boldsymbol{\theta}_d)$ and in terms of root mean square error (RMSE) of the TOA estimate $\rho_t(\boldsymbol{\theta}_d) = \sqrt{\rho_t(\boldsymbol{\theta}_d)}$. The CDF $F_E(e|\boldsymbol{\theta}_d)$ and the RMSE $\rho_t(\boldsymbol{\theta}_d)$ are obtained starting from (18) and (26), respectively. The localization accuracy is determined in terms of the Localization Error Outage (LEO). The LEO is defined as the probability that the localization error $\epsilon(\mathbf{p}) = \|\hat{\mathbf{p}} - \mathbf{p}\|$ (\mathbf{p} is the tag true position and $\hat{\mathbf{p}}$ is the estimated one) is above a maximum tolerable value ϵ^* .

3.13.4.1 Wireless Scenario and Energy Detector Setting

Consider a network of readers in known positions aiming to localize tags in unknown positions within an indoor environment. Specifically, the network is composed of four anchors located at the corners of a square with side length equal to 10m. Each reader emits a sequence of UWB root-raised cosine

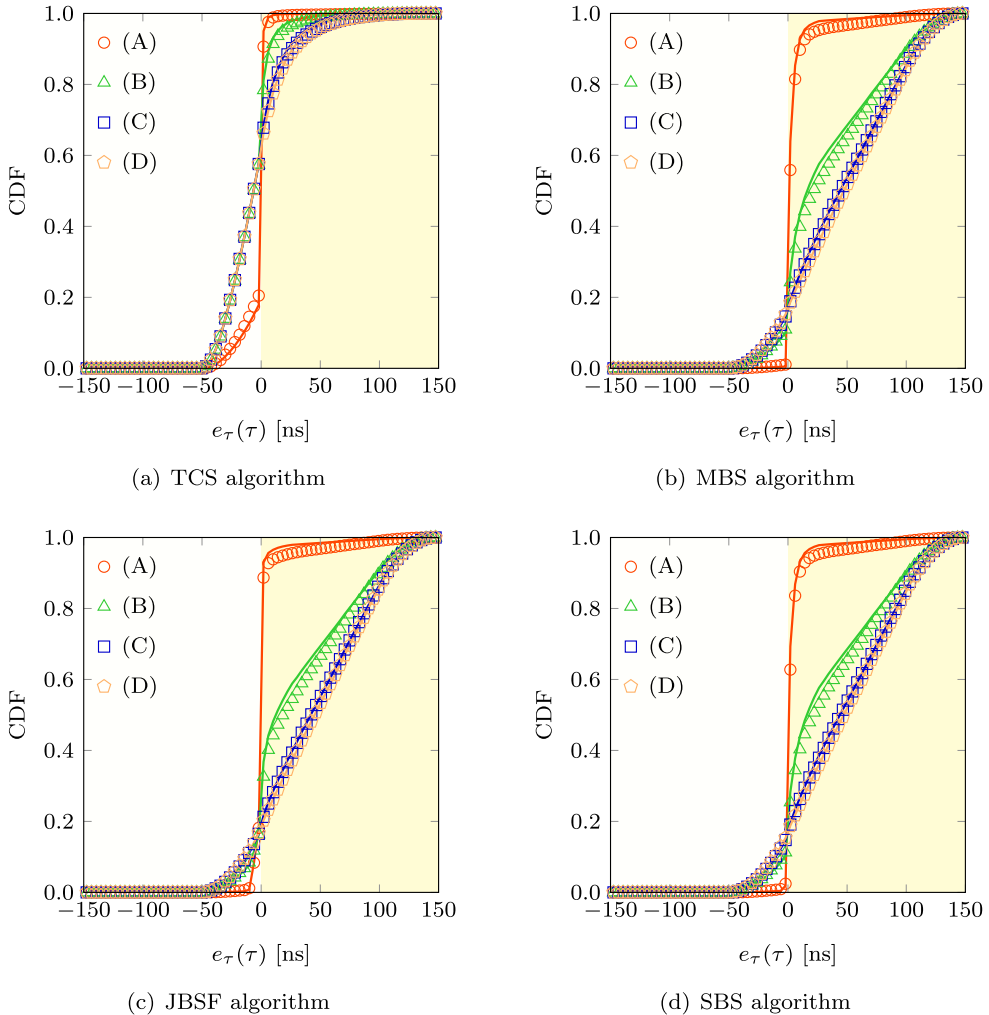


Figure 52: Example CDF of the TOA estimation error for the TCS, MBS, JBSF with $N_w = 5$, and SBS algorithms with different values of N_p and γ : (A) $N_p = 128$, $\gamma = -10\text{dB}$; (B) $N_p = 16$, $\gamma = -10\text{dB}$; (C) $N_p = 128$, $\gamma = -20\text{dB}$; and (D) $N_p = 16$, $\gamma = -20\text{dB}$. Theoretical results are shown in solid lines and simulation results are shown in symbols.

pulses with bandwidth W and pulse repetition period $T_{\text{pr}} = 150\text{ns}$. The transmitted power spectral density is compliant with the emission masks according to the following regulations: (a) Japan (Asia Pacific Telecommunity); (b) Europe (European Telecommunications Standards Institute) and Korea (Asia Pacific Telecommunity); (c) USA (Federal Communication Commission); and (d) China (Asia Pacific Telecommunity). The wireless medium follows the IEEE 802.15.4a channel model for UWB indoor residential line-of-sight (LOS) environments [4] with $T_a = 50\text{ns}$.

The received signal is processed based on energy detection with observation time $T_{\text{obs}} = T_{\text{pr}}$ and $\xi_i = \xi \forall i \in \mathcal{B}$ is considered for illustration. The received signal-to-noise ratio (SNR) per pulse is $\gamma = E_p/N_0$ where E_p is the energy of the received signal pulse and N_0 is the one-sided power spectral density (PSD) of the noise component. The noise has mean zero and variance $\sigma^2 = N_0W$. The bandwidth W depends on the emission masks. Unless otherwise stated, results are provided for a number of bins $N_b = 75$, a dwell time $T_d = 2\text{ns}$, and an emission mask as defined by the Federal Communication Commission with bandwidth $W = 7.5\text{GHz}$. The threshold is chosen according to (28) as the ξ that minimizes the MSE of the TOA estimate with a guaranteed minimum level of detection probability $P_d^* = 95\%$.

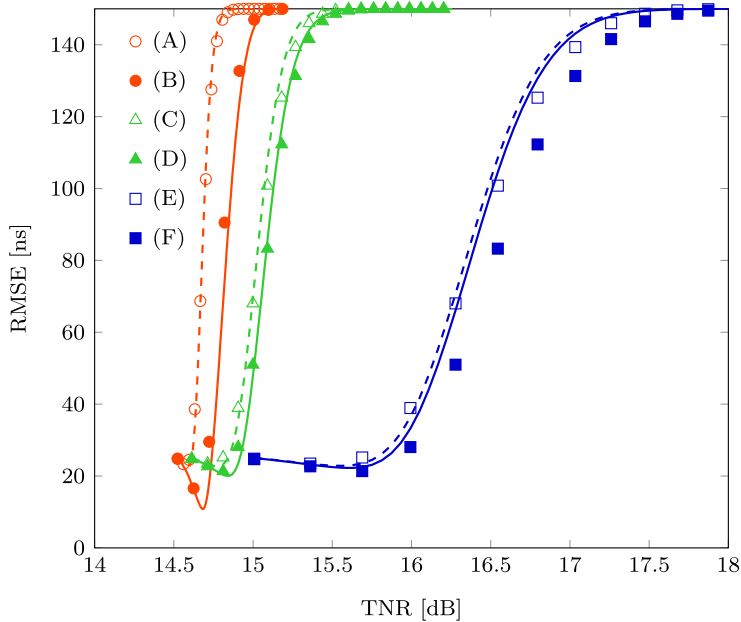


Figure 53: RMSE of the TOA estimate as a function of TNR per pulse for different values of N_p and γ : (A) $N_p = 128$, $\gamma = -20\text{dB}$; (B) $N_p = 128$, $\gamma = -10\text{dB}$; and (C) $N_p = 16$, $\gamma = -20\text{dB}$; (D) $N_p = 16$, $\gamma = -10\text{dB}$; (E) $N_p = 1$, $\gamma = -20\text{dB}$; and (F) $N_p = 1$, $\gamma = -10\text{dB}$. Theoretical results are shown in solid lines and simulation results are shown in symbols.

3.13.4.2 Performance Results

Figure 52 shows the CDF of the TOA estimation error for hard-decision algorithms with different values of N_p and γ . Two different regions can be discerned for the TOA estimation error: the negative errors (light gray region) due to early detection caused by the noise, and the positive errors (light blue region) due to late detection caused by the wireless channel. It can be observed that the results obtained from the proposed range information model are in agreement with those obtained through sample-level simulations in both regions. It is apparent that the distribution of the TOA estimation error is non Gaussian. Furthermore, the behaviors of the hard-decision algorithms are different in the early detection region, in which the errors are due to false alarms. This behavior is due to the fact that the threshold is chosen to minimize the MSE of the TOA estimate with a guaranteed minimum level of detection probability. Note that, while practical systems typically operate with high N_p values, a conservative scenario with small N_p values up to 128 is considered here to strain the proposed range information model. The absolute error of the TOA estimate for $N_p = 128$ and $\gamma = -10\text{dB}$ per pulse is evaluated to be below 3.33 ns (corresponding to about 1 m) in 72%, 56%, 73%, and 61% of the instances for TCS, MBS, JBSF with $N_w = 5$, and SBS algorithms, respectively. The absolute error of the TOA estimate is evaluated to be below 5 ns (corresponding to about 1.5 m) in 79%, 79%, 81%, and 80% of the instances for TCS, MBS, JBSF with $N_w = 5$, and SBS algorithms, respectively.

Figure 53 shows the unconditional RMSE of the TOA estimate for the TCS algorithm as a function of the normalized threshold (TNR) per pulse $\xi/(N_p \sigma^2)$ for different values of N_p and γ . The unconditional RMSE is defined as $\sqrt{\nu_t(\boldsymbol{\theta}_d)}$ where $\nu_t(\boldsymbol{\theta}_d)$ is given in (32) with $\nu(\boldsymbol{\theta}_d) = T_{\text{obs}}^2$, which is the maximum possible MSE. It can be seen that the results obtained from the proposed range information model are in agreement with those obtained by sample-level simulations. The accuracy of the proposed model enables a system designer to determine the optimal TNR value that minimizes the RMSE, which is important for ED design. It can also be observed that the minimum RMSE decreases with N_p for a given γ . On the other hand, the RMSE varies more rapidly with TNR as N_p increases, revealing that the determination of the optimal threshold is critical for large N_p .

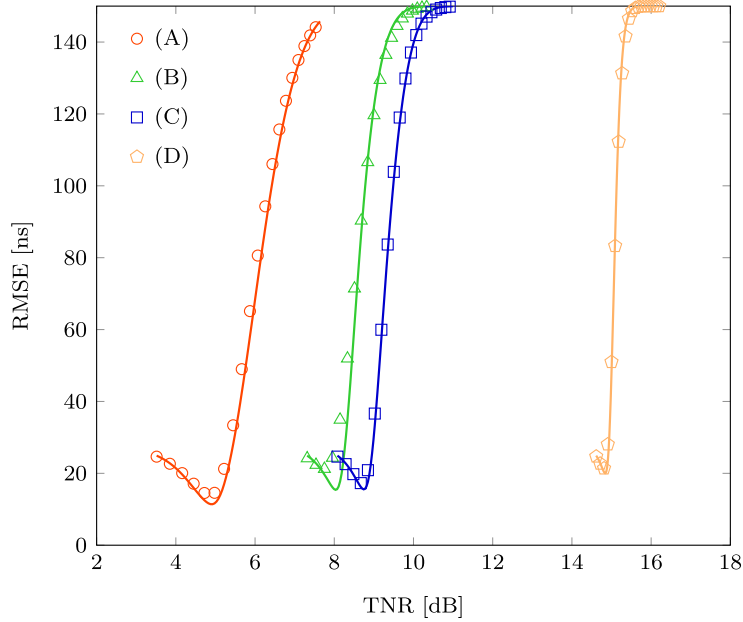


Figure 54: RMSE of the TOA estimate as a function of TNR per pulse for $N_p = 16$, $\gamma = -10\text{dB}$, and different emission masks: (A) China; (B) Japan; (C) Europe/Korea; and (D) USA. Theoretical results are shown in solid lines and simulation results are shown in symbols.

Figure 54 shows the unconditional RMSE of the TOA estimate for the TCS algorithm as a function of the TNR per pulse $\xi/(N_p \sigma^2)$ for different emission masks, $N_p = 16$, and $\gamma = -10\text{dB}$. In particular, emission masks that are compliant with the regulations of the following countries are considered: (a) China ($W = 0.6\text{GHz}$); (b) Japan ($W = 1.4\text{GHz}$); (c) Europe lower band/Korea ($W = 1.7\text{GHz}$); and (d) USA ($W = 7.5\text{GHz}$). It can be observed that the results obtained from the proposed range information model are in agreement with those obtained through sample-level simulations for all the values of the bandwidth W . As shown in Figure 53, the optimal TNR that minimizes the RMSE can be obtained from the proposed range information model. Note also that the RMSE varies more rapidly as the bandwidth W increases, revealing that the determination of the optimal threshold is critical for large W .

The localization accuracy of a network in which the agent position is determined according to the maximum likelihood (ML) criterion is now presented. Figure 55 shows the LEO as a function of the maximum tolerable localization error for soft-decision and hard-decision localization with $T_d = 2\text{ns}$, $N_p = 128$, and different values of the SNR per pulse received at 1m denoted by γ_0 . For hard-decision localization the JBSF algorithm with $N_w = 2$ and 5 , as well as the TCS algorithm are considered. The threshold ξ is chosen according to (28) with $P_d^* = 95\%$. It can be observed that the LEO obtained from the range information model is in agreement with that obtained through sample-level simulations. The effect of N_w on the LEO is evident, especially for the smaller γ_0 . It can be seen that a localization error smaller than 1.45, 1.50, and 1.37 meters can be achieved 95% of the time for case (A), (B), and (C) respectively, with $\gamma_0 = 10\text{dB}$. Similarly, 0.39, 0.39, and 0.40 meters can be achieved under the same settings with $\gamma_0 = 30\text{dB}$.

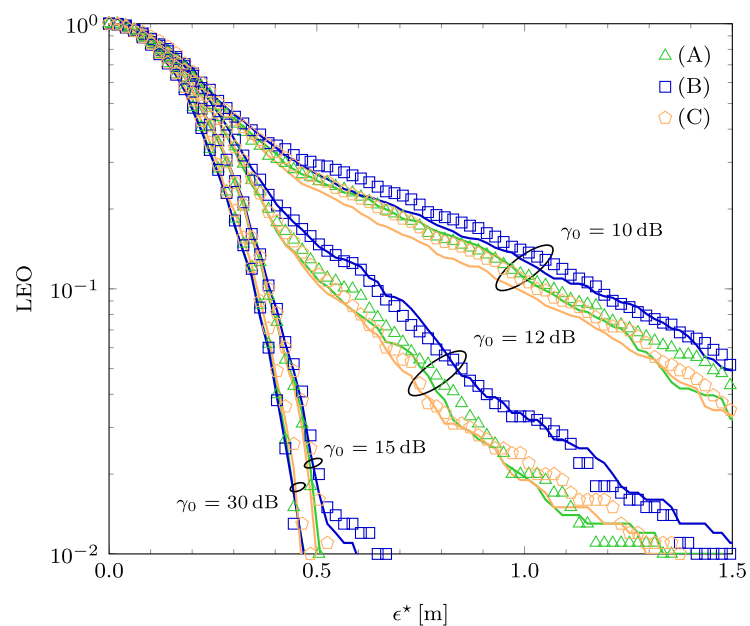


Figure 55: LEO as a function of the maximum tolerable localization error for soft-decision and hard-decision localization with $T_d = 2 \text{ ns}$, $N_p = 128$, and different values of γ_0 : (A) JBSF with $N_w = 5$; (B) JBSF with $N_w = 2$; and (C) TCS. Theoretical results are shown in solid lines and simulation results are shown in symbols.

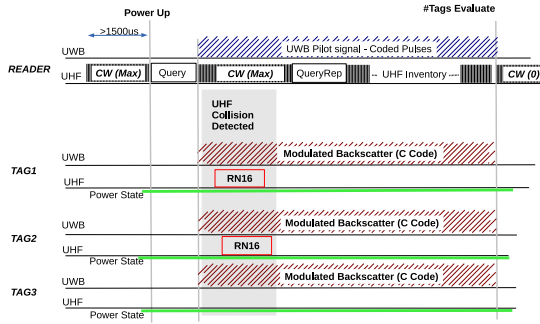


Figure 56: Standard UHF inventory in the first estimate of active tag number.

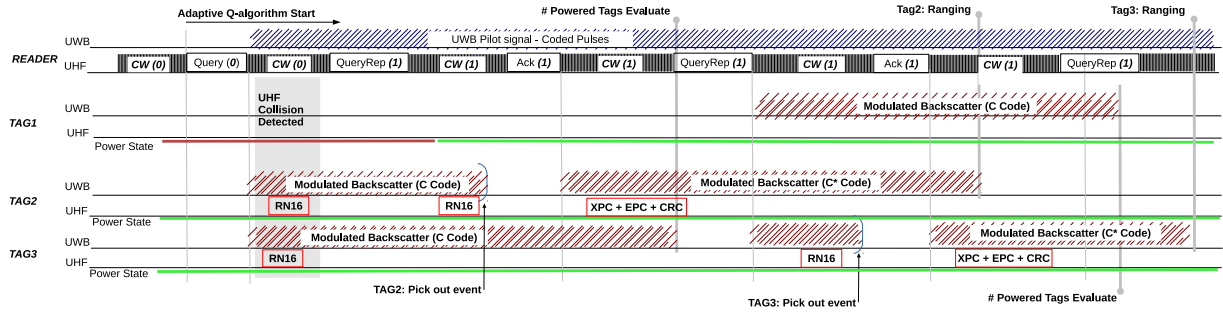


Figure 57: Example of UWB and UHF signal in the adaptive Q-algorithm, highlighting the UWB link tag use, the estimated number of tags (c_n code) and ranging (c_n^* code).

3.14 Network Management Protocols

3.14.1 UWB-enhanced Identification

In this section, we describe an enhanced ISO/IEC 18000-6C protocol for fast and energy efficient identification. Recall that the ISO/IEC 18000-6C standard is designed by considering that the number of tags and their position are not known a priori. However, in the presence of UWB modules, the reader can perform accurate and fast tag population estimation in parallel with the identification procedure. Then, it is possible to adapt the transmission range of the reader so that the average number of tags in each query is under control.

3.14.1.1 Identification algorithm

The time evolution of the algorithm is illustrated in Figs. 56 and 57 and described in the following.

- 1) Initially, the reader transmits a continuous-wave UHF signal (CW) to power up the tags in its maximum transmission range $RangeMax$.
- 2) As soon as the nodes are powered (i.e., $T_{pw} \approx 1500 \mu s$), the interrogation starts by following the standard ISO/IEC 18000-6C protocol. Together with the first *Query* command, the reader starts transmitting a sequence of UWB pulses and tags respond by modulating the backscattered UWB signal using the c_n code.
- 3) The reader interprets the received backscattered signal and estimates $Range0$ and $Range1$, namely the interrogation ranges that contains N_0 and $N_0 + N_1$ tags, respectively.
- 4) The reader then selects $Q = [\log_2 N_0]$, where $[.]$ denotes the nearest integer function, and sends the following *Query* command with sufficient power to interrogate tags in $Range0$.
- 5) Between consecutive *Query* commands, while interrogating tags in $Range0$, the reader continues the UWB ranging procedure by considering $Range1$ and $Range2$, which includes further N_2 tags. The

UHF transmission power is set to reach also tags that are interrogated in the next *Query*. By doing so, those tags are already powered when receiving the *Query* command.

6) After N_1 tags have been identified, the reader increases the transmission power of the following *Query* command to reach tags in *Range1* and, similarly, after $N_1 + N_2$ tags have been identified, the transmission power is increased to include *Range2*. In this way, the average number of active tags in different stages of the interrogation is kept between $N_0 - N_i$ and N_0 . Notice that already identified tags stop responding to query commands as well as backscattering modulated UWB pulses in the same interrogation session.

8) The transmission range is increased every N_i successful interrogations until it reaches *RangeMax* and the session ends when all tags have been identified.

We recall that the proposed mechanism is compliant with the ISO/IEC 18000-6C specifications for both the reader and the tag. The optimal choice of the parameters N_i is not straightforward. Every time the reader includes new tags, it has to issue a *Query* command instead of a shorter *QueryAdj* command. Therefore, if N_i is too small, the interrogation time and the energy consumption are negatively affected.

3.14.1.2 Determining the transmission ranges

Consider a reader that is transmitting with power level $P_{tx,dBm}$ in the UHF domain. We use an inverse power model of the link gain, and include shadowing component as well. The received backscattered power from a tag located at a distance r (meters) is then expressed as follows:

$$P_{bs,dBm} = P_{tx,dBm} - c_0 + M - 4 \log_{10} r, \quad (33)$$

where the constant c_0 (in dB) represents the power gain at the reference distance 1 m, and it can account for specific propagation environments and parameters, e.g., frequencies and antennas and M (in dB) is the antenna gain of the tag. In the operating conditions for ISO/IEC 18000-6C systems, with LOS between reader and tag, we have $c_0 \approx 45$ dB, and $M = 6$ dB [5]. The term $4 \log_{10} r$ accounts both for downlink and uplink.

By considering the reader read sensitivity S (dBm), i.e., the minimum power that can be decoded by the reader, we derive the relation between transmitted power at stage i and the corresponding range of interrogation,

$$P_{tx,dBm,i} = S + c_0 - M + 4 \log_{10} r_i \approx 39 + S + 4 \log_{10} r_i.$$

Commercial readers typically guarantee $S = -11$ dBm, and a transmission power range $P_{tx} = [20 - 32]$ dBm, which gives a distance range $r \approx [0.01 - 10]$ m.

Similar derivations hold in the UWB domain. However, the transmit power that is necessary for ranging purposes is much lower, i.e., $P_{tx}^{UWB} < 0$ dBm [6]. Therefore, in the derivation of the total energy consumption, the UHF term becomes dominant.

3.14.2 Performance Results

In this section, we show simulation results of the proposed algorithm and the performance in terms of average query success rate and total energy consumption during an interrogation session. The average query success rate corresponds to the average probability of identifying a tag in a query round. The energy consumption is calculated at the reader, by considering the transmission power levels in the different stages for UHF and UWB channels. Both the query success rate and the energy consumption depend on protocol specifications as well as the number of tags, the distance between the tag and the reader, environment, etc.

In this validation we assume static channel conditions and zero bit-error rate. Moreover, as we are interested on assessing basic performance of the identification protocol, we here neglect the effects of antenna polarization on the communication range of the reader.

A single reader is deployed to interrogate a population of $N = [27 - 125]$ tags deployed in a 3D volume according to a pallet model as in Fig. 58. The UHF air interface parameters are set to default

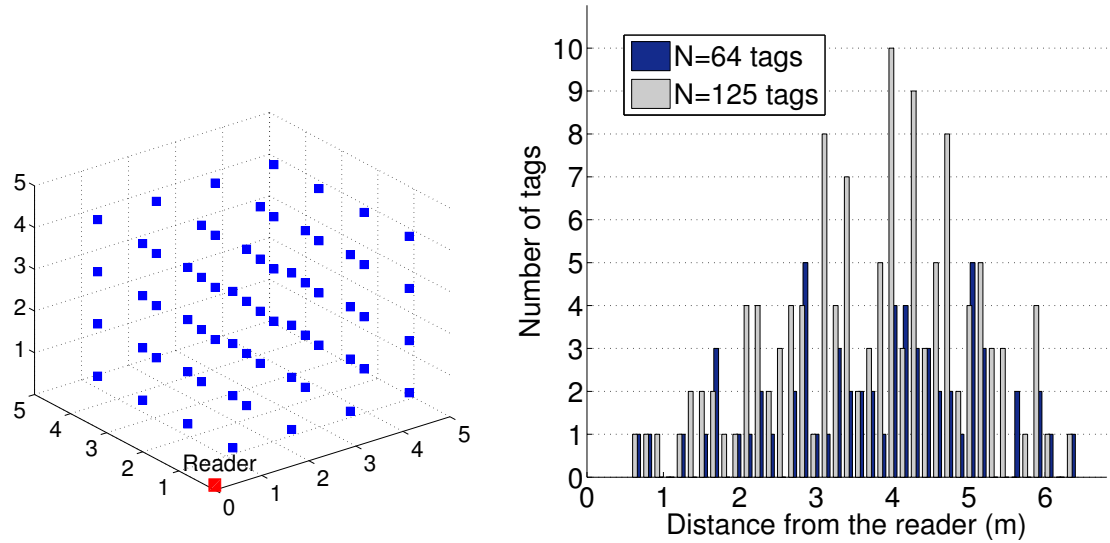


Figure 58: 3D Deployment of 64 tags, according to a pallet model (left) and distribution of the number of tags vs. distance to the reader for 20 cm ranges (right).

specifications in [7] for tag modulation rate of 125 KHz, Table 1. The UWB parameters are set as described in Table 2.

We show the performance results in terms of query success rate in Fig. 59 and total energy consumption in Fig. 60 of the standard ISO/IEC 18000-6C MAC and the proposed approach with $N_0 = 10$ and $N_i = 5$, for $i \geq 1$. We consider different levels of accuracy for the UWB ranging. The accuracy is measured in terms of maximum estimation error on the interrogation ranges (i.e., on the number of tags actually present in each range). A value of 2 cm can be achieved with very accurate UWB modules, while 20 cm can be a fairly conservative value [8]. The proposed mechanism achieves a query success rate ≈ 0.42 with 25% gain with respect to the ISO/IEC 18000-6C for the case with high ranging accuracy. The gain is only slightly reduced (20%) in the case of low ranging accuracy. The energy consumption is 25% lower with our proposed identification with respect to the ISO/IEC 18000-6C thanks both to the faster identification speed and the use of lower transmission power level. Interestingly, there is no significant dependency of the energy consumption with respect to the accuracy level.

3.14.3 Multi-Reader Systems

For a wide set of applications, characterized by large-scale tags deployments, single reader systems (i.e., one reader-multiple tags) are often unable to cover the entire region of interest, given the limitations of the reader's interrogation range. This motivates the use of multiple readers (Fig. 61), geographically distributed and networked in some fashion.

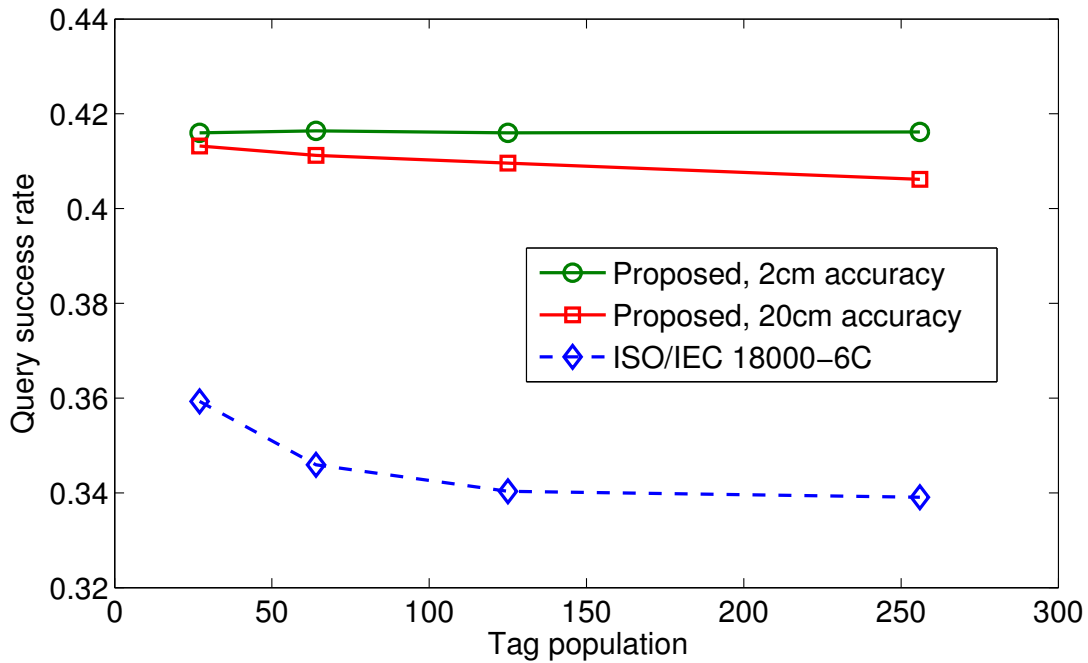


Figure 59: Query success rate vs. tag population. The proposed approach guarantees up to 25% improvement to the standard ISO/IEC 18000-6C for large-scale networks.

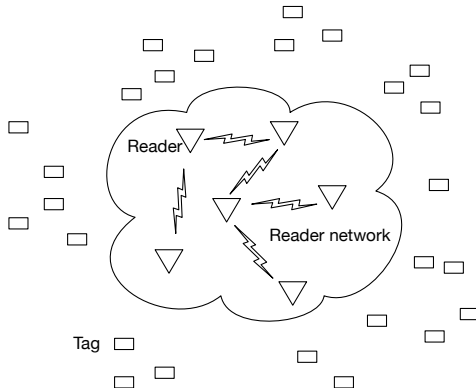


Figure 61: Multi-Reader/Multi-Tag System

The use of multiple readers not only improves coverage, but can also improve system performance and is strictly needed to meet real-time requirements for some kind of applications. However, multi-reader MAC protocols design is challenging given that different kind of collision problems arise. Indeed, unlike the single reader scenario, in which the *tag-tag collisions* can be handled by classical anti-collision schemes, in multi-readers systems interference between readers lead to different kind of collisions known as *reader collisions*. The interferer is represented by a reader and the interfered entity can be either a reader or a tag. Thus, we can distinguish two kind of reader collision (Fig. 62): *reader-tag collision* and *reader-reader collision*.

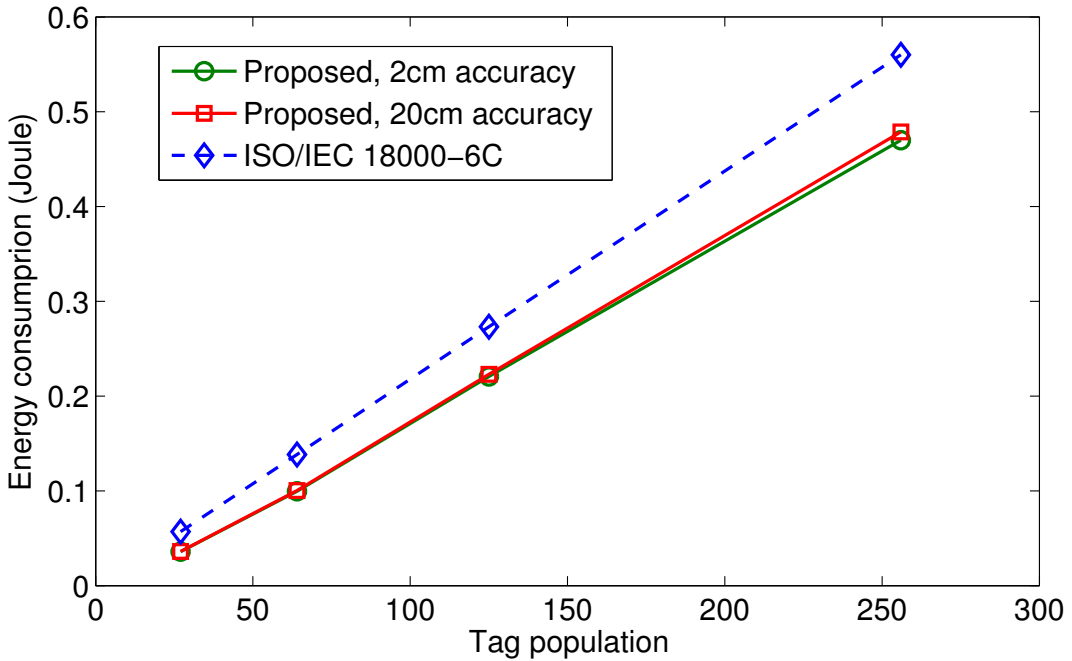


Figure 60: Total energy consumption vs tag population. The proposed approach guarantees more than 20% improvement to the standard ISO/IEC 18000-6C for large-scale networks.

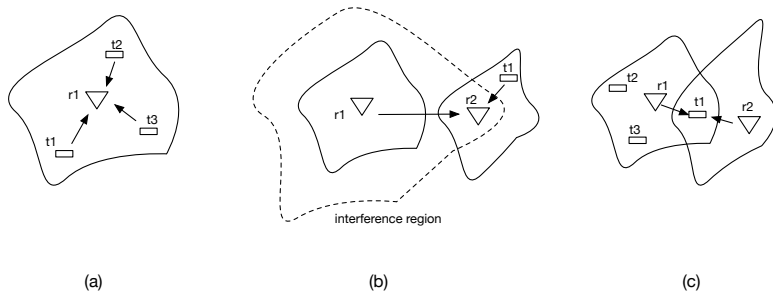


Figure 62: Collisions in multiple-reader RFID systems. (a) Tag-Tag collision. (b) Reader-Tag collision. (c) Reader-Reader collision

A *reader-tag* collision occurs when a reader is in the interference region of another reader (Fig. 62-(b)). Thus, even if the signal of two reader are out of range from each other, may still collide at the tags in the region between them. For example referring to Fig. 62-(b), the reflected signals reaching r_2 from t_1 easily get distorted by signals from r_2 . This kind of collision can be avoided by assigning different channel to near-by readers, or by scheduling reader activation at different times.

A *reader-reader* collision occurs when two reader with overlapping interrogation regions are active at the same time (i.e., simultaneously sent their requests and collide at the tags in the overlapping region). For example referring to Fig. 62-(c), signals from r_1 and r_2 may collide at tag t_1 that cannot recognize any query and the tag is read neither by r_1 nor by r_2 . Due to this kind of collision, r_1 will be able to read t_2 and t_3 but it may not be able to read t_1 . Unfortunately, this kind of collision cannot be avoided by frequency planning (i.e., tags have no filtering capabilities) and the only way to resolve them consist in handling reader activation scheduling.

Different approaches has been proposed to mitigate and solve the reader collision problem. In what follows, we briefly describe the principal existing MAC techniques proposed for this purpose.

1) *Listen Before Talk* (LBT): this *Carrier Sense Multiple Access* (CSMA) based protocol is standardized by ETSI EN 302 208 [9]. The protocol requires the reader to sense the channel for a specified minimum time before transmitting. If the channel is sensed idle for that time, the reader starts reading, otherwise it starts a random back-off procedure waiting for the channel becomes idle. However this kind of protocol may not be able to detect collision due to the *hidden terminal problem*.

2) *Colorwave* [10]: Colorwave is one of the first proposed protocols for solving the reader collision problem. It is a distributed TDMA (i.e., it assumes the presence of a single frequency channel) based algorithm where each reader chooses a random time slot, also referred as *colors*, to transmit. Whenever a collision is detected (i.e., two or more readers choose the same color), a reader choose a different time slot and communicate such a change to its neighbor readers. However, Colorwave require time synchronization between readers and relies on collision detection, which cannot be performed unless the tags are involved in the detection process.

3) *Pulse* [11]: Pulse is a distributed algorithm based on *beaconing*, which aims to handle the reader collision problem while resolving the hidden terminal problem typical of CSMA-based protocols. This is done by assuming two non-interfering channels. The first one (control channel) is reserved for reader-to-reader communication, while the second one (data channel) is used for reader-to-tag communication. When transmitting on the data-channel, the reader broadcasts beacon messages on the control channel to inform other readers of the ongoing data exchange, thus inform potentially colliding readers that the data-channel is busy. However, being a contention-based method, the access delay is supposed to increase when the number of contending readers increase.

4) *EPCGlobal Generation 2* [12] This standard proposes a FDMA-based solution to the reader collision problem. In particular, using spectral planning, it separates reader transmission and tag transmission such that tags only collide with tags and readers only collide with readers. However the protocol only solves reader-reader collisions, given that tags have no frequency selectivity. Hence when two readers using different frequencies communicate with a tag simultaneously, it will lead to collision at the tag. Thus reader-tag collision problem still exist in this standard. Further, the standard does not specify frequency planning techniques.

5) *Hierarchical Q-Learning* (HiQ) [13]: HiQ is a hierarchical, online learning algorithm that finds dynamic solutions to the Reader Collision Problem in RFID systems. HiQ attempts to minimize reader collisions by learning the collision patterns of the readers and by effectively assigning frequencies over time to ensure neighboring readers do not experience collisions from one another. HiQ is arranged hierarchically with distributed, local control. The algorithm is based on a type of reinforcement learning called Q-learning, which is used to determine frequency and time assignments. Through repeated interaction with the system, Q-learning attempts to discover an optimum frequency assignment over time. However, in order to maintain a hierarchical structure, overhead is occurred and the larger the network size is, the more inefficient the scheme becomes.

One of the most important problem strictly related to tag identification, is how to estimate the tag population cardinality, which is in general unknown. Counting the number RFID tags, namely *RFID counting* [14], is needed by a wide set of applications. In some application domains, it is desirable to simply count or just estimate the number of tags without explicitly identifying individual tags, while for some other scenarios, in addiction to its direct utility, *RFID counting* can also serve as a pre-processing step in support to other tasks (i.e., knowing the rough number of tags can make the identification process much more efficient). Referring to the counting problem we can distinguish two main version of the cardinality estimation problem. 1) The *single-set RFID counting* problem, which fall in the single reader system class, where a single static reader aims to count the number of tags that fall in its interrogation range. 2) The *multiple-set RFID counting* problem where the interrogation region of a single reader cannot cover the entire area of interest. Thus this problem is related to the multi reader systems category, or can be formulated considering a single mobile reader that sequentially visits a number of locations in order to cover the entire region of interest (Fig. 63). Note that in both cases there will be overlapping region, thus multiple counts and collision may affect the performance of the counting method. In both version of the problem, a key performance metric is the amount of time needed to count or estimate the

total number of tags and the main objective of a counting approach should be reducing this time.

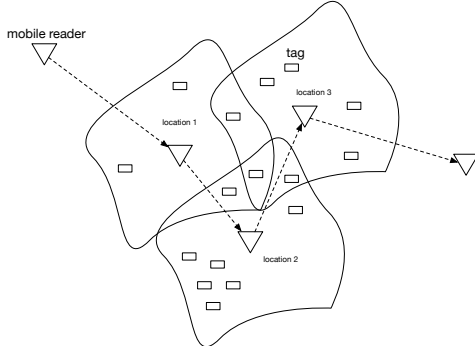


Figure 63: Mobile readers that visit a set of different positions

Different counting approaches and protocols have been proposed in the literature. For a detailed overview on the features and performance of these protocol one can refer to [14].

Most of these protocols are developed based on some common concepts. In particular they are all composed of a sequence of *round* or *trials*. Each *trial* is consist of a sequence of slots. At the beginning of each round, the reader broadcast a command to the tags and tags respond to the reader choosing a time slot according to a given scheme. The number of slot in a trial is called *length* of the trial. A slot is nonempty when only one tag respond in that particular slots. On the other hand, a slot is empty if either no tags respond in that time slot or multiple tags respond in that slot (i.e., a collision occurs). Based on observation of access patterns, the number of tags in the network can be estimated from various statistical quantities on the status of the slots [14]. The counting problem is an open research field, especially for multi-reader system and there is a great effort in finding simple and time-efficient solutions. In [14], the authors claim that a key aspect in developing accurate and efficient counting protocols is to divide the estimation process in two phase. The first phase results in a rough estimate of the number of tags. This first estimate can be used during the second phase to achieve the desired accuracy.

Very fast, reliable and efficient tag population estimation can be achieved by employing Ultra Wide Band (UWB) technology [15], [16]. UWB not only provide time-efficient tag population estimation, but also allows for accurate tags ranging and localization. Consequently, hybrid RFID systems based on both UHF and UWB guarantee two main advantages from a MAC layer perspective. First, fast tag population estimation can be used as a support for interrogation process (i.e., performed in the UHF band), improving collision resolution techniques provided by the existing standard. In particular, referring to EPCGlobal Generation 2 protocol, UWB technology allows to overcome drawbacks of the adaptive *Q-Algoritm*, which provides dynamic frame length update only based on observation of collided and idle slot patterns. Contrarily, having available an estimate of the number of tangs involved in the interrogation process, allows to develop more efficient frame length update algorithms for framed ALOHA-based MAC protocols resulting in more robust anti-collision solutions and thus in faster interrogation processes.

Second, UWB can be successfully employed as the core technology in developing *multi-reader cooperative systems*. Most of the MAC solution presented in this field are based on concurrently readers operations. However, more efficient and robust solutions for multi-reader RFID systems may be developed by allowing readers to cooperatively operate for targeting some common performance requirements. In this perspective, fast tags ranging, localization and counting are strictly needed in designing a cooperative readers network for large-scale dissemination RFID systems characterized by real-time requirements, high read reliability and accurate localization. Cooperation among readers can be defined in many different ways. Here, we present three possible scenarios (Fig. 64) in which reader cooperation can be exploited to improve MAC layer efficiency.

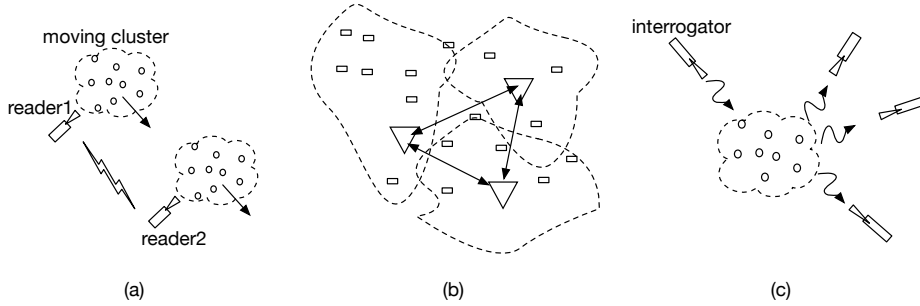


Figure 64: Readers Cooperation

In scenario of Fig. 64-(a), moving clusters of tags (e.g., conveyor belt applications) have to be identified as fast as possible. Reader cooperation represent a promising approach in this kind of application. For instance, the first reader can estimate the approximative number of tag in the arriving clusters, allowing the second to set accurate and fast reading process by communicating estimation information through a dedicated wireless link.

This concept can be generalized as in Fig. 64-(b), where a set of networked readers scan a wide area with high number of disseminated tags. In this case, readers can exchange ranging and population information in order to perform efficient tag identifications. This information can be further used to adjust interrogation ranges of readers in order to reduce interference guaranteeing high performance collision resolution at MAC layer and thus improving reading reliability and speed.

Cooperating readers may also act in multi static radar fashion Fig. 64-(c). In particular one reader act as the interrogator and the others are enabled for collecting tags responses. The interrogator, after energizing tags, send an enable command to other readers in the network making them only able to collect tag responses for identification proposes. Note that, in this case, the reader collision problem no longer subsists and only tag-tag collisions have to be addressed, for instance, by means of traditional anti-collision approaches. Again, UWB technology can be conveniently exploited for ranging, localization and tag population estimation and as a support for MAC layer operations.

3.15 Efficient RFID Tag Identification exploiting UWB and Compressive Sensing

A novel tag identification protocol based on compressive sensing (CS) and ultra-wide-band (UWB) is described. The main feature of the proposed scheme is that exploits UWB information to reduce the ID search space of CS decoding. This hybrid technique may significantly decrease the amount of required time consumption for successful identification as well as computational complexity compared to an UHF-RFID only protocol.

One of the current problem is related to the insufficient performance of the anti-collision algorithm. On this purpose, several research works has been done to improve such anti-collision performance [17].

Compressive Sensing (CS) solutions [18] and [19] have been proposed as an alternative to the current state of the art based on Frame Slotted-ALOHA (FSA). Unlike anti-collision protocols, collisions are useful in CS-based techniques, by allowing tags responding at the same time.

The main problem in CS is to reduce the ID search space. On this purpose, [18] proposes a coarse estimation of the number of active tags. Then the tags are divided in groups, among which the ones with active tags are selected through a time division multiple access (TDMA) procedure. Finally, the ID search space is reduced before performing CS for tags identification.

A large amount of time slots is required in [18] for groups identification, which reduce the overall efficiency of the protocol. On the contrary, we propose a novel CS-based solution, which combine ultra-wide-band (UWB) information to reduce the total amount of time slots spent for tags identification.

Specifically, in the presence of UWB modules, the reader can perform accurate and fast tag population estimation and groups identification. Then, it is possible to reduce the search space size by knowing such information. In particular, we divide the tags in groups, so that we discard from the search space the IDs

associate with groups that have all inactive tags in order to reduce the search space size. On this purpose, UWB modules can help by estimating the received UWB code associated to the group the tag belongs to. In particular, differently from UWB ranging where only one UWB code is needed, we use multiple codes to discriminate among groups. UWB modules performs this operation really fast, only few time slots are necessary for that. Moreover, tag population and groups information is useful also to adapt the length of the ID codes associated with the tags.

3.15.1 System Model

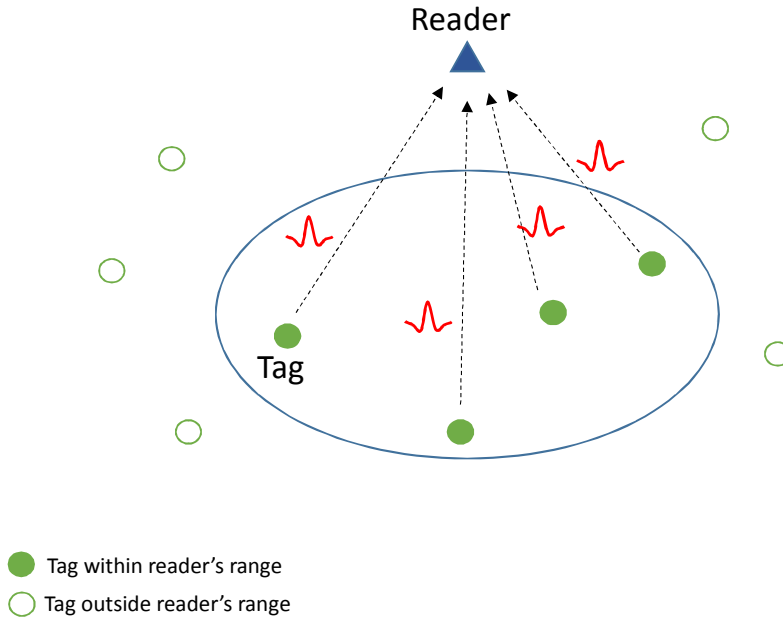


Figure 65: Proposed System Model

We consider an RFID system, as shown in Fig. 65, composed of K active tags within the reader's range and our purpose is to identify these K tags. As known, according to the EPC Gen-2 standard [20], the size of the temporary ID space is equal to $N = 2^{16}$, since each RN16 ID is a 16-bit sequence. Each tag chooses a temporary ID among N . A binary vector \mathbf{x} of size N is defined, where $x_j = 1$ if tag j is one of the active K tags to be identified, and $x_j = 0$ otherwise. Therefore, $\|\mathbf{x}\|_0 = K$, since there are K non-zero elements in \mathbf{x} . We want to identify the elements j for which $x_j = 1$.

After receiving a start command, i.e., a Query from the reader, each tag for which $x_j = 1$ uses its ID as a seed in its hash function [21] to generate an $M \times 1$ pseudorandom binary vector \mathbf{c}_j , whose elements $c_{ij} \in \{+1, -1\}$, where $i = 1, 2, \dots, M$. The j -th column of \mathbf{c} corresponds to the j -th code associated with the j -th tag. M denotes the number of bits required for successful identification. Gathering all vectors \mathbf{c}_j in the coding matrix $\mathbf{C} = [\mathbf{c}_1 \mathbf{c}_2 \dots \mathbf{c}_N]$ of size $M \times N$, where $M < N$, we have that the received measurement vector \mathbf{y} at the reader is given by

$$\mathbf{y}_{M \times 1} = \mathbf{C}_{M \times N} \mathbf{H}_{N \times N} \mathbf{x}_{N \times 1} = \mathbf{C}_{M \times N} \mathbf{z}_{N \times 1} \quad (34)$$

where $\mathbf{z} = \mathbf{Hx}$, where \mathbf{H} is the diagonal channel matrix, whose elements $\mathbf{H}_{jj} = h_j$ denote the complex channel coefficient for tag j . Indeed, since each tag transmits in a narrowband channel (640 kHz) its channel can be modeled as a single tap channel [20].

Fig. 66 shows the received signal \mathbf{y} according to the collision based identification scheme [19].

The reader uses a CS decoding scheme to estimate the elements of vector \mathbf{z} . The estimation of \mathbf{z} is formulated as an optimization problem [22], [23]:

Objective:

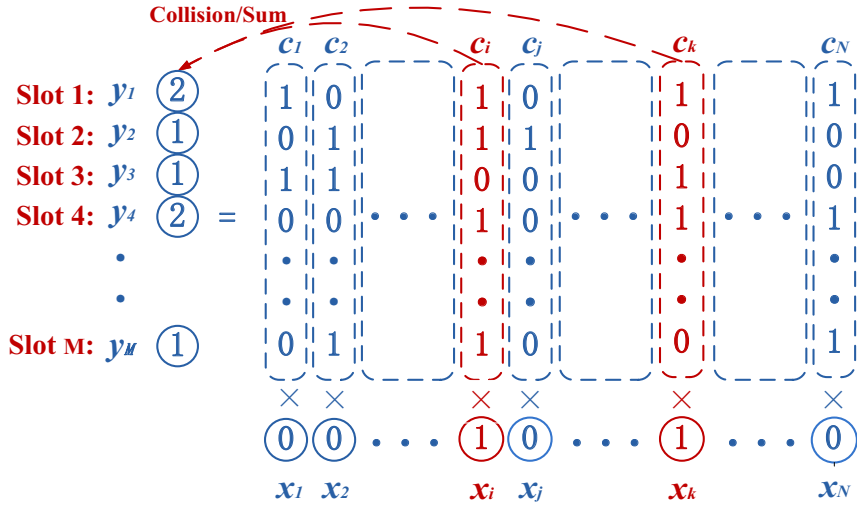


Figure 66: Collision-based identification scheme

$$\min_{\mathbf{z}} \|\mathbf{z}\|_1 \quad (35)$$

Subject to:

$$\mathbf{Cz} = \mathbf{y} \quad (36)$$

where $\|\cdot\|_1$ is the L^1 norm.

To guarantee stable recovery in presence of noise, the number of measurements M , i. e. the length of the ID code associated to a tag, must obey:

$$M \geq \alpha K \log \left(\frac{N}{K} \right) \quad (37)$$

where α is a constant [23]. However, this condition imposes a prohibitive high value of M for $N = 2^{16}$, the whole ID search space. For this reason, it is needed to reduce the ID search space before employing CS techniques.

However, the 16-bit sequence of RN16 IDs are not used in the CS-based protocols, since, generally, they will not fulfill the necessary condition (37) for successful recovery. Thus, M -length pseudo-random sequences are generated and transmitted in place of them.

A drawback of CS-based protocols is that these pseudo-random sequences have to be received synchronously at the reader. Anyway, synchronization is not a strict requirement at low data rates used for usual RFID applications.

3.15.2 Tag population estimation and groups identification

As said before, the UWB domain is responsible for *tag population estimation* and *group identification*. Let us assume a reader that interrogates the tags in its communication range by transmitting an UWB signal with a specific spreading code. For population estimation, it is reasonable to consider that tags share the same code c_n , but since we want to use this code also for group identification, we here assume different codes where c_n^g is the code of the g -th group, with $g = 1, \dots, N_g$ and N_g is the total number of groups. Specifically, we divide the tags in groups, so that we discard from the search space the IDs associate with groups that have all inactive tags in order to reduce the search space size of CS decoding scheme.

Let us consider all tags that backscatter at the same time. The energy collected by the UWB receiver at the reader give an estimate of tag population [24]. The tag population estimate reduces to estimating the number K of backscattered pulses.

According to the distance-based path-loss, the tags that are distant are penalized with respect to close ones. In order to guarantee that signal from the furthest tags can be detected with sufficient energy, a sufficient number of pulses per chips N_{pc} is necessary. On this purpose, a synchronization safeguard allows to neglect the problem of clock drift at the tags, and simplifies the UWB backscattered modulator switch requirements.

The *group identification* is then performed by estimated the received codes c_n^g , where $g = 1, \dots, N_g$, and N_g is the number of groups. On this purpose, it is possible to reduce the time spent to detect the groups with active tags by properly choosing the type of codes associated with the groups in order to optimize the search of family codes. Group identifications is then useful for the search space reduction, as detailed in the following.

Moreover, as we discuss in the next section, tag population estimation and group identification can be efficiently integrated with the operation of the UHF tags identification protocol.

3.15.3 Proposed UWB-CS Algorithm

In this section, we describe an enhanced CS protocol for fast identification.

Recall that CS protocols for tags identification, as well as ISO/IEC 18000-6C standard, are designed by considering that the number of tags and their position are not known a priori. However, in the presence of UWB modules, the reader can perform accurate and fast tag population estimation in parallel with the identification procedure. Then, it is possible to adapt the length M of the codes by knowing the estimation of tag population K and by reducing the search space size. On this purpose, UWB models can help by estimating the received codes c_n^g associated to the group the tag belongs to. In particular, we divide the tags in groups, so that we discard from the search space the IDs associate with groups that have all inactive tags. In this way it is possible to reduce the search space size of the CS decoding scheme.

3.15.4 First step: Estimating the number of active tags and groups

The time evolution of the algorithm is described in the following.

1. Initially, the reader transmits a continuous-wave UHF signal (CW) to power up the tags in its transmission range.
2. As soon as the nodes are powered (i.e., T_{pw} - 1500 μ s), the interrogation starts. Note that differently from the standard ISO/IEC 18000-6C protocol, the CS procedure does not need retransmission when a collision occurs. In particular, together with the Query command, the reader starts transmitting a sequence of UWB pulses, to which the tags respond by modulating the backscattered UWB signal using the c_n^g codes.
3. The reader interprets the received backscattered signal and estimates both the tag population K and the identification of the groups with active tags according to the received UWB codes c_n^g .

3.15.5 Second step: Reducing the scale of Compressive Sensing

Since CS moves the computational complexity from coding to decoding, a CS benefit is that the RFID tags can be quite low-cost. However the reader must handle more computing work. The decoding complexity of CS is $O(N \times \log(N/K))$ [23], which is really high when the number N of all the RFID tags is huge. On this purpose, the reader must reduce the scale of suspected RFID tags.

The protocol proposed in [18] uniformly divide all the RFID tags into groups and use a TDMA protocol to identify the groups with active tags. Specifically, the reader assigns one time slot to each group to detect if it has active RFID tags or not. In case there is an active tag in the group interrogated in a given time slot, it reflects the inquire RF signal to reply the reader. If there is no answer during that time

slot, the reader considers that there is no active tags in that group and can discard the tags IDs associate to the corresponding group from the search space.

We here propose to exploit UWB information to reduce the search space size. Specifically, the reader interprets the received backscattered signal and estimates the groups with active tags according to the received UWB codes c_n^g . Only the tags IDs associated with that group codes c_n^g will remain the search space, the other ones will be discarded, thus reducing the number of columns of the matrix \mathbf{C} in (34).

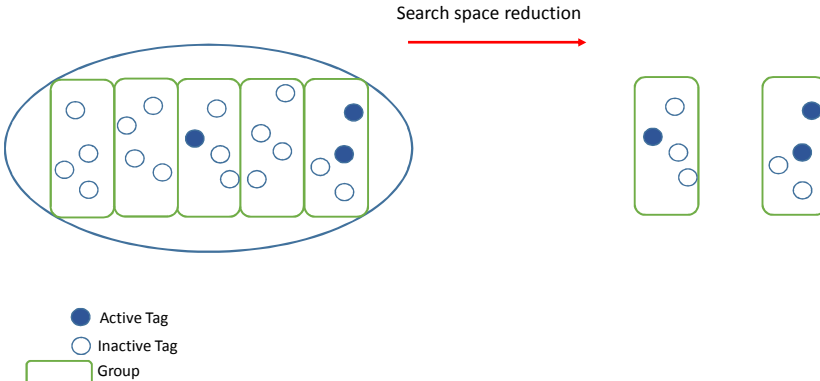


Figure 67: Groups formation and Search space reduction

Let \mathbf{C}' be a reduced version of the matrix \mathbf{C} that keeps only the columns corresponding to the remaining $N_g^* s_g$ possible temporary IDs, where N_g^* is the number of the groups with active tags, s_g is size of the group, with $N_g^* \leq K$. \mathbf{x}' and \mathbf{H}' are the similarly reduced forms of \mathbf{x} and \mathbf{H} . In this way, the reader only needs to regenerate \mathbf{C}' , as opposed to \mathbf{C} .

3.15.6 Third step: Tags Identification through CS Decoding Scheme

Now that we have reduced the scale of CS problem to recovering K temporary IDs out of only $K s_g$ possible IDs at most, and according to the notation in Sec. 3.15.5, the system to solve becomes:

$$\mathbf{y} = \mathbf{C}' \mathbf{H}' \mathbf{x}' = \mathbf{C}' \mathbf{z}' \quad (38)$$

To decode, the reader uses compressive sensing to estimate the elements of vector \mathbf{z}' .

Objective:

$$\min_{\mathbf{z}'} \|\mathbf{z}'\|_1 \quad (39)$$

Subject to:

$$\mathbf{C}' \mathbf{z}' = \mathbf{y} \quad (40)$$

The space of the problem is now N' as opposed to N , with $N' < N$ and $N' \leq N_g^* s_g$, where N_g^* is the number of groups with active tags.

3.15.7 Number of CS Measurements

In the proposed UWB-CS protocol, the total number of time slots used for tags identification, which is equal to the number of measurements or bits, must satisfy

$$M_{UWB-CS} \geq G + \beta K \log(s_g) \quad (41)$$

The term " G " is a constant that refers to the time slots needed to identify the groups with active tags. Indeed, the proposed UWB scheme is able to recover the groups just in few time slots since the usual

length of UWB spreading code ($N_c = 128$) is sufficient to identify a common number of groups N_g and it is possible to properly choose the type of codes associated with the groups in order to optimize the search of family codes.

Once groups identification is performed, the number of measurements M , i. e. the length od the code, for tags identification needs to obey (37) to guarantee stable recovery in the noisy case.

After the space reduction, (37) become:

$$M \geq \beta K \log \left(\frac{N_g^* s_g}{K} \right) \quad (42)$$

Since in the worst case, at most each of the K active tags can be placed in a different group, in this case $N_g^* = K$ and:

$$M \geq \beta K \log (s_g) \quad (43)$$

3.15.8 Simulation Environment

We evaluate the efficiency of the proposed solution to identify active tags for a different number of active tags, i.e., 4, 8, 12 and 16, out of a total number of 8000 tags.

We compare the proposed UWB-CS solution with the FSA system used in ISO/IEC 18000-6C standard, and with BUZZ protocol [18], a CS-based multiple access scheme applied to RFID system.

FSA uses 16-bit temporary IDs for the RFID tags. As first step, the reader sends a Query command and allocates a frame containing 2^Q time slots in order to identify the active tags. Each active tag randomly picks a slot and sends its temporary ID during that time slot. If multiple tags pick the same time slot, a collision occurs ad the temporary IDs can not be correctly decoded. In this case the procedure needs to be repeated. In order to avoid another collision, the reader increases Q to $Q = Q + C$ and the tags re-transmit their IDs until all the temporary ids are correctly received.

According to the FSA used in [18], we first set $Q = 2$, then if a collision occurs, Q is increased to $Q = Q + 0.3$. The reader assigns 2^Q frame in order to identify the active tags. Each frame is composed by 16 slots to transmit the 16-bit temporary IDs.

In BUZZ system, the size of group is set equal to 50. In this way, the 8000 RFID tags are divided into 160 groups. Given the TDMA scheme proposed in [18] (detailed in Sec. 3.15.5) it takes 160 time slots to reduce the scale of suspected tags.

In the proposed system, by exploiting the UWB information, the reducing phase contains only few steps that are performed just in few time slots.

3.15.9 Performance Evaluation

The simulation result of time consumption is shown in Fig. 68. Along with the number of active tags increases, all the three schemes spend more and more time to identify the tags. By using compressive sensing, the BUZZ and proposed scheme reach the goal of efficiently speeding up the identification in RFID system. In addition, the proposed UWB-CS scheme has a higher efficiency than BUZZ because of the reduction scheme based on UWB information. In particular, UWB modules are able to identify groups with active tags in few time slots, while BUZZ protocol use a TDMA procedure where one time slot is dedicated for the identification of each group. In our UWB-CS scheme, the usual length of UWB spreading code ($N_c = 128$) is sufficient to identify a common number of groups N_g . In our simulations we consider $N_g = 160$ with a group size $s_g = 50$ as in [19].

The following Fig. 69 shows three main characteristics of the proposed solution: it outperforms the other solutions; its capability to exploit UWB information returns in a really fast group identification, compared to the another CS-based approach (BUZZ protocol), thus it needs less time slots for a successfully tags identification; finally it is easy to note that the slope of the two CS-based approaches

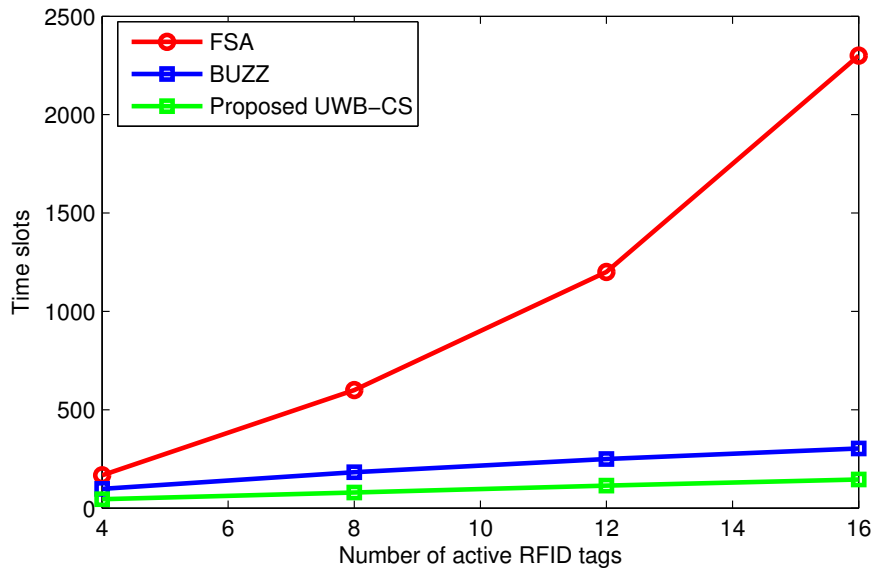


Figure 68: Time consumption: Comparison among FSA, BUZZ and the proposed UWB-CS

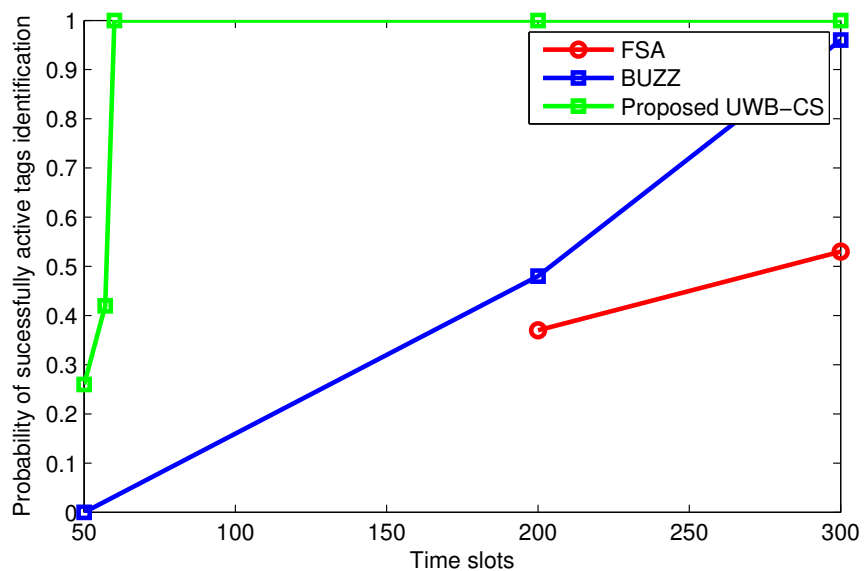


Figure 69: Probability of successfully identify the active tags when $K = 12$: Comparison among FSA, BUZZ and the proposed UWB-CS.

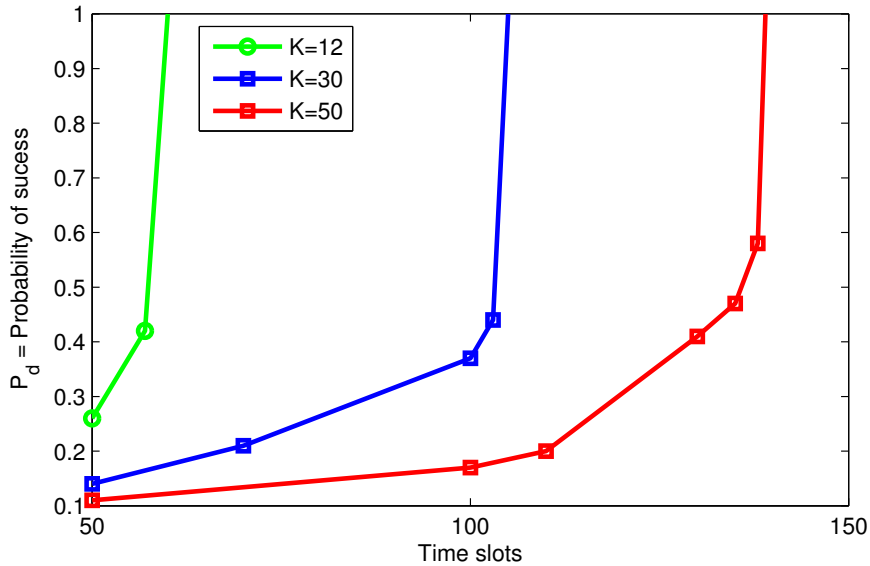


Figure 70: Probability of successfully identify the active tags varying the number K of active tags: Proposed UWB-CS under different conditions of simulation.

(UWB-CS and BUZZ) is higher than FSA solution proving that CS solutions are really effective for tags identification.

The following Fig. 70 refers to the proposed UWB-CS scheme under different conditions of simulation. Specifically, it describes the behavior of the probability of correct tags identification by varying the number of active tags. Fig. 70 shows that, as soon as the critical number of time slots is reached, the proposed solution is able to identify the active tags with high probability. In particular, when the number of time slots is less than the minimum value of M_{UWB-CS} expressed in (41), the proposed protocol can fail in identify the active tags, while as soon as the number of time slots guarantees (41), the proposed solution identify the tag with high accuracy.

Finally, to summarize, CS techniques allows collisions among tags, while UWB modules are able to quickly estimate the tag population and to help the search space size reduction for CS decoding scheme. Simulation results prove the effectiveness of the proposed solution, by showing the improvement in terms of time slots spent for tags identifications respect to other existing protocols, and hence the energy consumption reduction.